**UNIVERSITY OF CALIFORNIA, SAN DIEGO**

**SAN DIEGO STATE UNIVERSITY**

# Multi-scale Current Activated Tip-based Sintering of Powder-based Materials

A dissertation submitted in partial satisfaction of the
requirements for the degree Doctor of Philosophy
in

Engineering Sciences

(Mechanical and Aerospace Engineering)

By

Ahmed Mohamed El Desouky

Committee in charge:

University of California, San Diego

Professor Joanna McKittrick, Co-Chair
Professor Jan Talbot

San Diego State University

Professor Khaled Morsi, Chair
Professor Samuel Kassegne
Professor Kee Moon

2012

The Dissertation of Ahmed Mohamed El Desouky is approved, and it is acceptable in quality and form for publication on microfilm and electronically:

_____

_____

_____

_____

(Co-chair)

_____

(Chair)

University of California, San Diego

San Diego State University

2012

## DEDICATION

TO MY MOM, DAD, SHAHIRA AND MONA FOR ALL THEIR LOVE AND SUPPORT THROUGHOUT MY CAREER

AND TO THE BRAVE PEOPLE OF EGYPT, WHO ARE CONTINUOUSLY FIGHTING FOR THEIR FREEDOM

# TABLE OF CONTENTS

## LIST OF FIGURES

# LIST OF TABLES

## ACKNOWLEDGEMENTS

I would like to thank my advisors, Prof. K. Morsi, and Prof. J. McKittrick for their full support through my PhD work. No words can express my gratitude for their great help and support.

Special thanks to Prof. K. S. Moon and Prof. S. Kassegne for all their support with the CATS project. This research would not have been possible without their help. I would like to express my appreciation to Prof. J. Talbot for her examination of this dissertation and serving on my doctoral committee.

I would also like to thank Dr. Steve Barlow for his training on the use of the Scanning Electron Microscope at the EM-Facility at SDSU. In addition I would like to express my gratitude to Mr. Mike Lester and Mr. Greg Morris for their technical help in the machine shop. Thanks to present and past members of the advanced materials processing lab.

# VITA

| | |
|---|---|
| 2005 | Bachelor of Science in Production Engineering, Alexandria University |
| 2005 – 2006 | Inspection Engineer, Middle East for Operation and Maintenance of Hydrocarbon Industries |
| 2007 – 2012 | Teaching Assistant, Mechanical Engineering Department, San Diego State University |
| 2012 | Doctor of Philosophy, Engineering Sciences (Mechanical and Aerospace Engineering), University of California, San Diego, San Diego State University Joint Doctoral program |

## PUBLICATIONS

1. **A. El-Desouky**, K.Morsi "Spark plasma sintering and related processes" *Journal of Materials Science* (working paper)
2. **A. El Desouky**, S. Kassegne, K.S. Moon, J. McKittrick, K. Morsi "Temperature Evolution in Current Activated Tip-Based Sintering" *Materials and Design* (Working Paper)
3. **A. El Desouky**, S. Kassegne, K.S. Moon, J. McKittrick, K. Morsi "Micro-scale Functionally Graded Porous Materials Using Current Activated Tip-Based Sintering (CATS)" *Journal of Material Science* (Submitted May 2012)
4. **A. El Desouky**, S. Kassegne, K.S. Moon, K. Morsi "Preliminary Investigations of the Effect of Particle Size and Tip Size in the Current Activated Tip-Based Sintering (CATS) of Nickel Powder Compacts." *Proceedings of the TMS Annual meeting and Exhibition* (2011)
5. K. Morsi, **A. El Desouky**, B. Johnson, A. Mar, S. Lanka "Spark Plasma Extrusion (SPE): Prospects and Potential" *Scripta Materialia,* v61, n 4 (2009) p 395-398
6. K. Morsi, **A. El Desouky.** "Preliminary evaluation of spark plasma extrusion" *Proceedings of TMS Annual Meeting and Exhibition* (2009) p 685-692

7. V.V Patel, **A. El Desouky**, J. E. Garay, K. Morsi. " Pressure-less and Current-activated Pressure-assisted Sintering of Titanium Dual Matrix Composites: Effect of Reinforcement Particle Size" *Materials Science and Engineering A*, v507, n1-2 (2009) p 161-166

8. K. Morsi, V.V. Patel, K.S. Moon, **A. El Desouky**, J.E. Garay "Preliminary investigation into the effect of composite reinforcement particle size on the sintering of titanium-titanium boride dual matrix composites" *Proceedings of the TMS Annual Meeting and Exhibition* (2008) p 337-344

# ABSTRACT OF THE DISSERTATION

Multi-scale Current Activated Tip-based Sintering of Powder-based Materials

By

Ahmed Mohamed El Desouky

Doctor of Philosophy in Engineering Sciences
(Mechanical and Aerospace Engineering)

University of California, San Diego, 2012
San Diego State University, 2012

Professor Khaled Morsi, Chair
Professor Joanna McKittrick, Co-Chair

Spark Plasma Sintering (SPS) is a process that has stimulated worldwide interest for the rapid consolidation of powder-based materials where electric current has played a major role. In this dissertation, the localization of SPS through current activated tip-based sintering (CATS) is presented where electric current is selectively applied to small targeted regions of a green compact/powder bed via a precision controlled electrically conductive small tip. The unique tip-specimen geometry allows for locally controlled temperature and current distributions that can result in microstructural modifications on the micro-scale. A novel experimental setup was used to investigate

the spatial and temporal temperature evolution in CATS under continuous electric current exposure. Both tip and compact surface temperatures were found to be a function of current exposure time, particle size and green compact density. The concept of effective current density is introduced to explain the findings in addition to the role of electrical and thermal conductivities. A finite element model was developed revealing surface and subsurface temperature profiles in CATS, which were supported by experimental findings. The unique tip-specimen configuration in CATS and its associated localized effects has been used to rapidly produce highly consolidate regions in addition to functionally graded porous materials on the micro-scale under a continuous current mode. The effects of initial green density and particle size on the porosity profile and pore size distribution in the developed micro-scale functionally graded material are discussed. The use of micro-scale tips (10 & 50 μm) in a moving tip configuration was established using a novel micro-CATs machine, where the effects of tip speed and current intensity were studied on nickel and copper powders with varying initial green density and particle size (down to 500nm). The precision controlled movement of the tips under current exposure enabled the consolidation of the material in remarkably thin regions (<5 μm) enabling micro-scale processing. Slower tip speeds at higher current intensities produced the highest degree of consolidation. Smaller particle sizes and higher initial green density powder compacts tend to experience higher quality consolidated lines due to a smaller inter-particle spacing.

# 1 INTRODUCTION

Spark Plasma Sintering (SPS) has been the center of attention of numerous researchers due its noticeable advantages over conventional sintering techniques such as rapid heating rates (50 - 1000°C$min^{-1}$), lower sintering temperature and much shorter holding times [1,2,3,4,5].In fact, the growth kinetics for intermetallic systems such as NiTi have been shown to be as 40 times quicker when using diffusion couples than by using conventional heating methods at the same temperature [6]. Research on SPS has been applied on a wide variety of materials such as single phase metals [7,8,9,10,11], ceramics [12,13], transparent ceramics [14], composites [15,16], nano-materials [17], biomaterials [18], intermetallics [19,20] and many other material systems. SPS basically involves the passage of pulsed or continuous direct current through powder (typical current densities used J=1000 $Acm^{-2}$ assuming no current density loss in the die material) while subjected to an applied pressure (Fig 1.1), resembling hot pressing with the difference in the heating principle of the powders (direct electric current heating vs. furnace heating).

It is clear that SPS will always be a very important process for powder consolidation for some time to come. However, it has been largely limited to bulk and simple shapes with a few exceptions of research efforts to combine the effect of electric current with metal forming processes such as electric rolling of powders [21,22] and spark plasma extrusion[23,24,25,26]. One other limitation of SPS is the high electric current requirements as high current densities are required to achieve higher density products, which leads to high energy consumption (a typical commercial SPS supplies

1000 – 10,000 A of direct current [27]). The sintering of products with larger surface areas also becomes challenging as extreme current inputs will be required to achieve the adequate current density for sintering. For example, to obtain a current density of 1000 $Acm^{-2}$ with SPS equipment having a maximum capacity of 10,000A, the specimen will have a maximum diameter of ~ 3.6 cm.

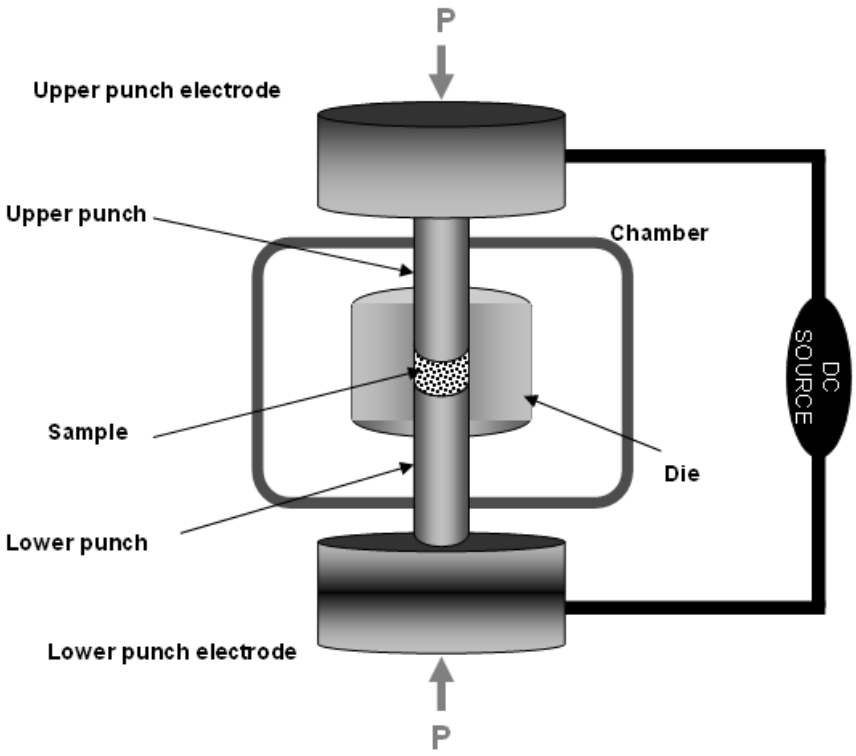


Figure1.1 Schematic of a SPS setup

A novel process called "Current Activated Tip-based Sintering (CATS)" was patented by Morsi and Moon [28] in the San Diego State University labs where pressure is applied and current is allowed to pass through a small conducting tip (stationary or moving) over a conducting powder bed to enforce SPS conditions on a controlled local area. Precise control of tip size, shape and path enables CATS to sinter extended

geometries and the process can be used in 3D fabrication where layers of powders are deposited and sintered sequentially. CATS also has the ability to sinter larger products compared to SPS when using moving macro-scale tips (such as rollers) with minimum electric current input requirements due to the small size of the tips.

This dissertation tackles a number of fundamental and novel issues related to CATS, these include the establishment of CATS processing on the micro-scale regime (down to the 10 μm level) as well as fabrication of micro-porous functionally graded materials. Experimental and modeling efforts towards the establishment of the governing processing-microstructural relations including simultaneous temperature measurements on the surface of the tip and the powder bed for the first time. The dissertation is divided into a number of chapters: Introduction – literature review – novelty aspects – experimental procedure – results and discussion- conclusions and directions for future work.

# 2 REVIEW OF LITERATURE

While a vast number of papers have been applying SPS to a large number of materials systems, comparatively less work has been devoted to other current activated sintering processes such as spark plasma extrusion (SPE), spark plasma joining (SPJ) and CATS. In this chapter, a literature survey is presented on different techniques involving electric current processing of powder-based materials.

## 2.1 Sintering

By definition, sintering is the act of bonding contacting particles together at high temperatures. It takes place either below the melting temperature of the sintered materials (solid-state sintering) or at temperatures equal to or higher than the melting temperature of one of the phases to be sintered (liquid-phase sintering). Figure 2.1 shows a scanning electron micrograph of solid state neck formation between particles [29]. The mass flow process during sintering takes place over four geometric categories known as the four classic stages of sintering. Table 2.1 outlines the sintering stages and their main characteristics [30]. During the adhesion stage, powder contact is mainly established through prior powder compaction and preparation. The initial stage is where necks start to grow and there is a significant loss in surface area, this is followed by the intermediate stage where the discrete particles begin to lose their identity and a tubular rounded pore structure is formed. In the final stage, the pores shrink into segregated spherical pores that are no longer connected to the surface. This stage is also characterized by rapid grain growth. Figure 2.2 shows a schematic of the four stages of sintering.

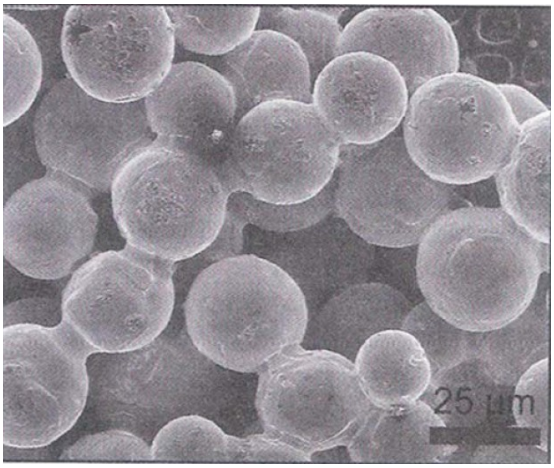


Figure 2.1 Scanning electron micrograph showing solid state neck-formation during sintering of bronze spherical powders [29]

Table 2.1 Classic stages of sintering [30]

| Stage | Process | Surface Area Loss | Densification | Coarsening |
|---|---|---|---|---|
| **Adhesion** | Contact formation | Minimal unless compacted at high pressures | None | None |
| **Initial** | Neck growth | Significant, up to 50% loss | Small at first | Minimal |
| **Intermediate** | Pore rounding and elongation | Near total loss of open porosity | Significant | Increase in grain size and pore size |
| **Final** | Pore closure, final densification | Negligible further loss | Slow and relatively minimal | Extensive grain and pore growth |

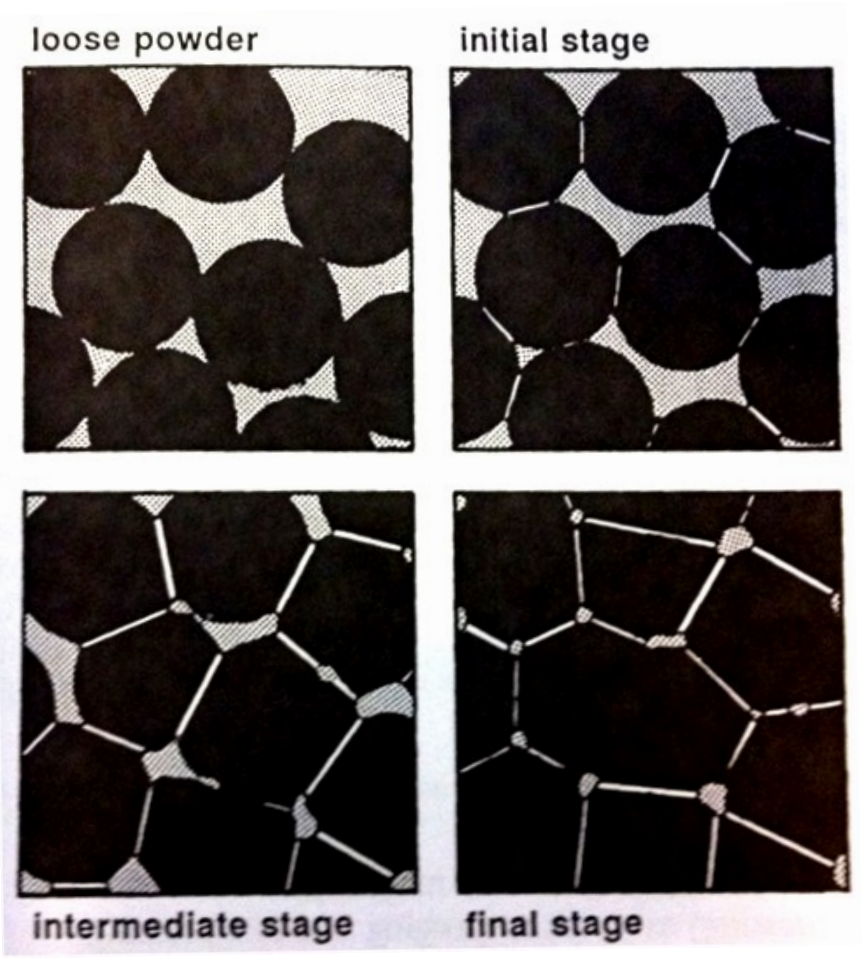


Figure 2.2 Classical sintering stages loose powders (adhesion), initial stage, intermediate stage and final stage [29]

### *2.1.1 Densification Parameter*

One important parameter in sintering is the densification parameter $\Psi$ which is a measure of fractional porosity change after sintering relative to the fractional porosity change needed to achieve full density (Equation 2.1)

$$\psi = \frac{f_S - f_G}{1 - f_G} \tag{2.1}$$

Where $f_S$ is the fractional sintered density and $f_G$ is the fractional green density.

Densification is often expressed in percentage and a densification of 100% corresponds to a powder compact that has been sintered to a pore-free fully dense material. Densification is a useful parameter especially when comparing specimens with different initial green densities (different initial porosity levels) [30].

### *2.1.2 Effect of initial green density on sintering*

When powders are compacted prior to sintering, different applied compaction pressures can lead to different green densities. Higher compaction pressures result in higher green density specimens with increased contact areas which are translated into larger neck sizes during sintering as shown in Figure 2.3. Higher green density specimens will also experience less shrinkage when approaching higher sintered densities and therefore are generally desirable in conventional sintering.

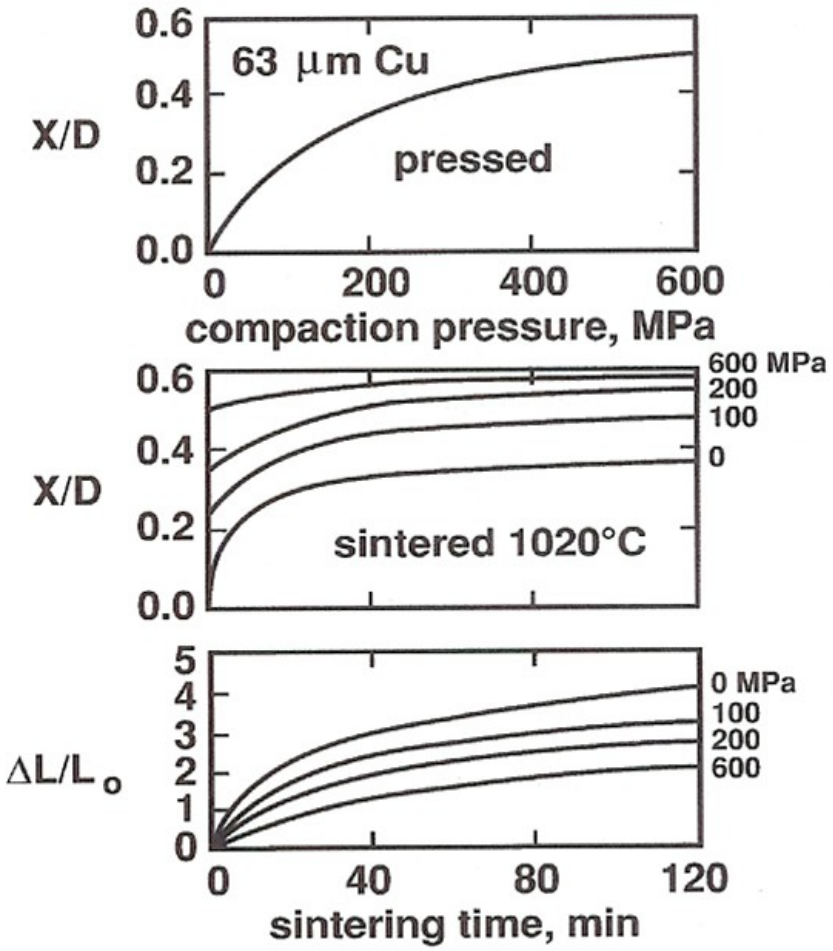


Figure 2.3 Effect of compaction pressure on sintering. The top two curves relate the neck size ratio to compaction pressure and sintering time, and the bottom curve shows the decreased shrinkage due to compaction [29]

### *2.1.3 Effect of powder particle size on sintering*

In general smaller size particles tend to sinter faster due to shorter diffusion distances, increased number of contact points and increased surface area [29]. Figure 2.4 shows the sintering behavior of nickel powders with various initial particle sizes.

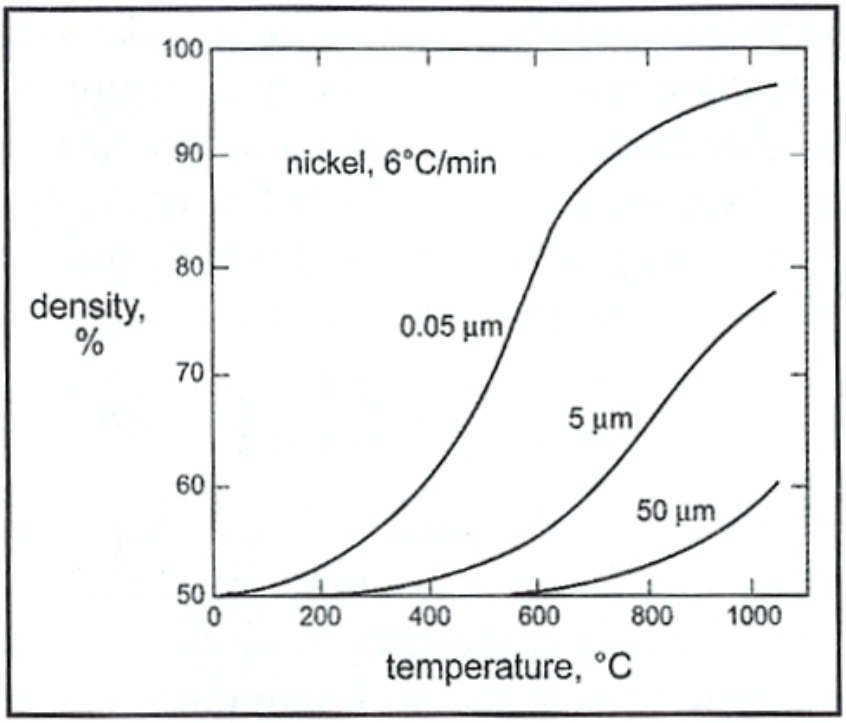


Figure 2.4 A plot of the sintered density versus temperature for different particle sizes of nickel [29]

## 2.2 Spark Plasma Sintering (SPS)

Spark plasma sintering (SPS), in basic terms a current-activated "hot pressing" process has been gaining immense interest from researchers worldwide. The realization that passing pulsed direct current through powders subjected to an externally applied pressure can significantly increase sintering rates has simulated many researchers to investigate the underlying reasons for this unique phenomenon and exploit it to rapidly sinter a vast number of materials [1-20]. This is a process with many synonyms; which include Field Assisted Sintering Technique (FAST) [31], Pulsed Electric Current Sintering (PECS) [7,32], Current Activated Pressure-Assisted Sintering (CAPAS) [16,33] and Current-Activated Pressure-Assisted Densification (CAPAD) [27,34], the

latter two names emphasize the importance of both pressure and current in this type of sintering process. Also Omori [13] indicated that SPS should refer to spark plasma "system" not sintering, since the setup does not only provide for sintering but also claimed spark plasma growth, spark plasma joining and spark plasma reaction. Despite the repeated use of the word "plasma" in current-activated powder processing, there is a controversy over whether plasma exists or not, this has been well documented and discussed and to this day there are still believers [4,13,35] and skeptics [1,27].

### *2.2.1 SPS Historical Perspective*

From a historical prospective, the work on using electricity to consolidate powders has been around since the early years of the 20$^{th}$ century. A patent by Lux in 1906 (Austria) [36] is claimed to be the earliest attempt to utilize electric current in the sintering of tungsten to form lamp filaments. Several articles and publications recognized A. G. Bloxam as the author of this patent but in fact Bloxam was only the patent attorney and Lux should be fully credited for this work. In 1922 a patent was reported on the production of dense materials from oxide powders where the electric current is used to heat up the sample to the appropriate sintering temperature [37,38]. The first attempt to combine electric current with uniaxial loading came out a few years later in a patent by Hoyt (working at General Electric Co. New York) [39]. Fig 2.1 shows the sketch of the used apparatus accompanying Hoyt's patent. WC/Co powders were used in Hoyt's experiments and a pressure of 7 MPa was simultaneously applied with electric current to the powder through electrodes connected to an external electric circuit, bringing the temperature up to ~1300-1450°C which was sufficient to

thoroughly sinter the powders. Gilson (also working for General Electric Co.) [40] performed the same experiments on reacting elemental W and C powders, his work is considered as the precursor to all current-activated reactive sintering. In 1934 Taylor [41] achieved full density WC/Co cemented carbide in less than one second by discharging a pulse of direct current to the powder followed by the imposition of alternate current.

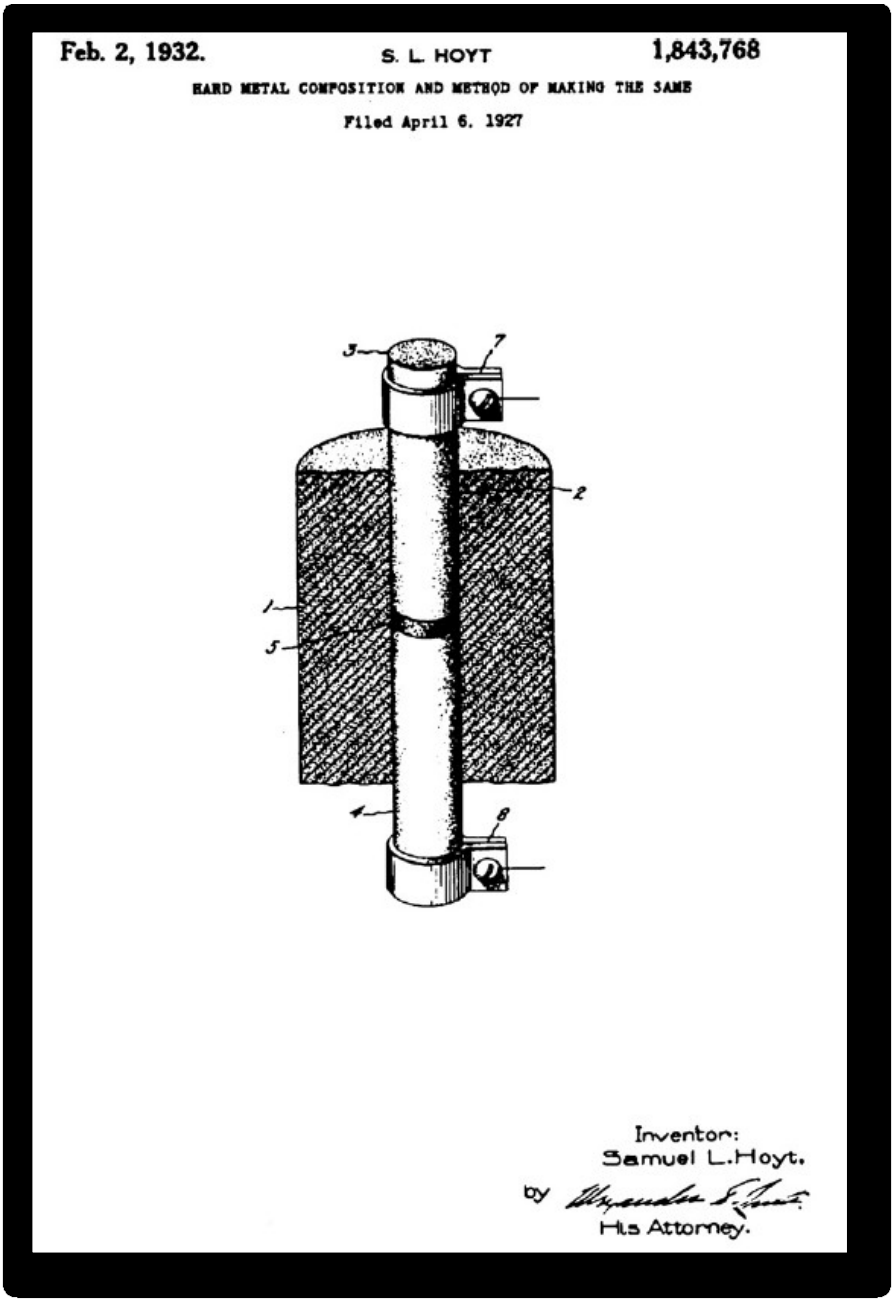
Feb. 2, 1932. S. L. HOYT 1,843,768

HARD METAL COMPOSITION AND METHOD OF MAKING THE SAME

Filed April 6, 1927

Inventor:
Samuel L. Hoyt.
by
His Attorney.

Figure 2.5 Hoyt's setup for simultaneous current and pressure application [37]

Patents by Inoue [42,43,44] received the most credit for providing one of the first solid studies on the effect of electric current during sintering [45]. His patent also introduced for the first time new basic sintering principles by using different waveforms

of current input such as alternative current, unidirectional alternative current and pulsed DC. Inoue named this process Electric Discharge Sintering (EDS) which was later named Spark Sintering (SS). Grasso et. al. [45] provided a comprehensive review of 642 patents on electric current activated sintering between the years 1906 and 2008. Fig 2.2 shows the evolution of number of SPS related patents over the last century.

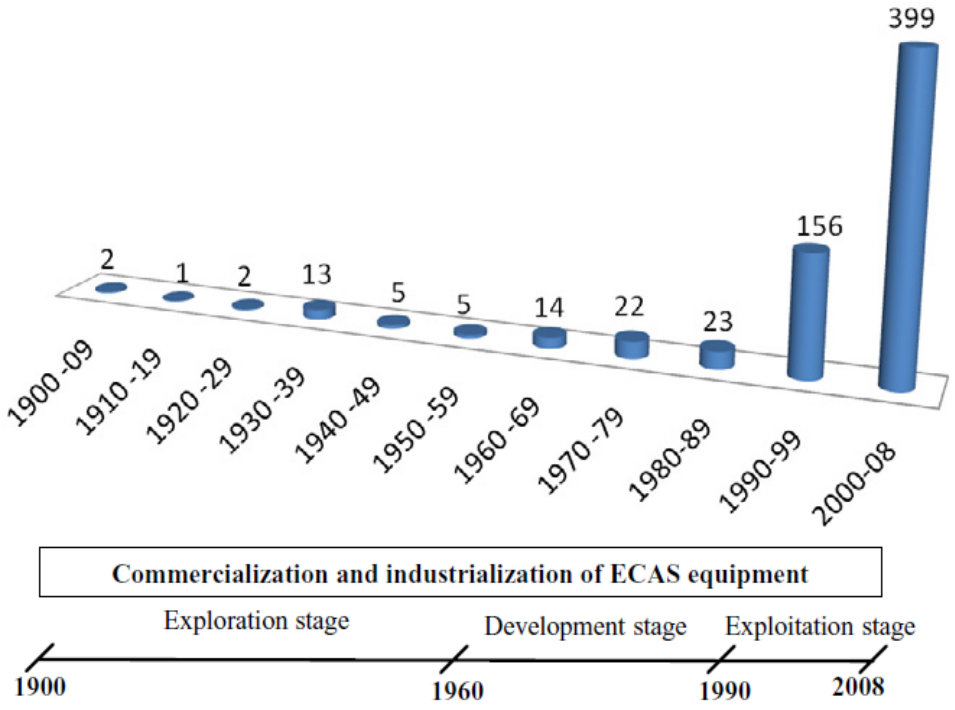


Figure 2.6 Number of electric current processing of powders related patents between 1900 and 2008 [45]

The exploitation stage over the last two decades was not only evident in the number of patents, Fig 2.3 shows that the number of publications related to electric current-activated sintering started to grow exponentially in the late 90s. This was due to the available commercialized SPS in Japan. In fact Japan, China and Korea have the

major contribution in SPS related research due to the large equipment availability in these countries [37].

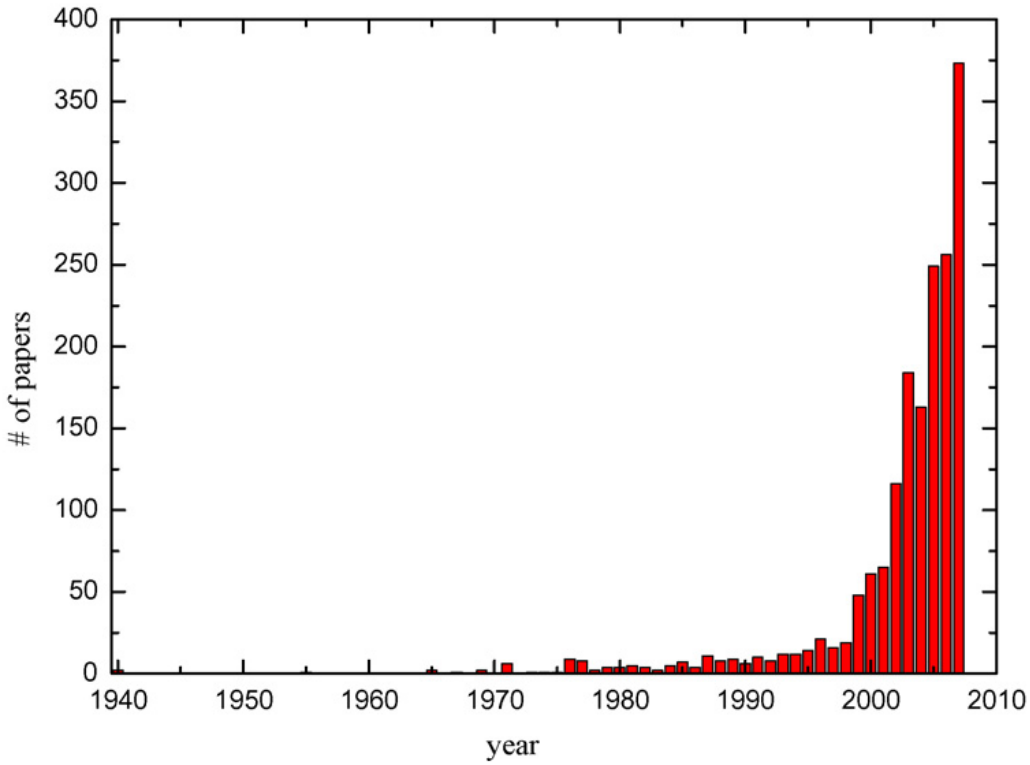


Figure 2.7 Number of publications related to SPS. [37]

### *2.2.2 Reviews on Current Activated Sintering*

Several reviews have been published on the SPS technique over the last decade with different focuses. One of the first review type articles in this area was on SPS of different material systems by Omori in 2000 [13], in this work Al metal and alloy, WC powder and AlN powder were sintered using SPS and the enhanced sintering mechanisms were mainly attributed to the presence of plasma due to pulsed current. The use of SPS apparatus in etching the surface of organic fibers as well as joining of

coupled eutectic powder systems were also discussed. In 2002 Mamedov [46] presented a short overview on SPS highlighting possible densification mechanisms of sintering that might be taking place during the process. However, Mamedov could not state with absolute certainty what actual mechanism takes place during the process and was inclined towards the possible effect of discharge between particles and the generation of plasma.

Munir *et al.* [47] provided the first comprehensive review on SPS parameters where the effects of heating rate, pressure, and electric current were studied separately. The debate on the presence of plasma was illustrated by supporters and skeptics in this study and its role was doubted especially with several studies showing no effect of electric pulse patterns on the final product. Another more recent review published by the same group [48] was published in 2011 where the role of current was discussed in more details and the presence of plasma and the effect of electric pulse frequency and duration were once again ruled out. In fact the process was named "electric current activation of sintering" in this work to avoid the use of the word "plasma". Other reviews by Garay [27] and Orru et al [37] also avoided the use of the word plasma naming the process "current-activated, pressure-assisted densification" and "electric current activated/assisted sintering" respectively. The work by Orru provided the most comprehensive review on SPS to date, over 96 different material systems were investigated under 58 different names of SPS. More than 1000 papers were reviewed in this work. Table 2.2 shows a list of reviews on the SPS process starting the year 2000.

Table 2.2 Summary of Reviews on SPS since 2000

| YEAR | TITLE | AUTHOR(S) | Topics Covered | Ref. |
|---|---|---|---|---|
| 2000 | Sintering, consolidation, reaction and crystal growth by the spark plasma system | M.Omori | Different material systems investigated (Al, WC, AlN, organic fibers, $CoSb_3$, eutectic powders) | [13] |
| 2002 | Spark plasma sintering as advanced PM sintering method | V. Mamedov | Diffusion and densification mechanisms | [46] |
| 2006 | The effect of electric field and pressure on the synthesis and consolidation of materials: A review of the spark plasma sintering method | Z. Munir *et al* | Effect of Electric current, temperature and pressure during SPS | [47] |
| 2009 | Spark Plasma Sintering as a Useful Technique to the Nanostructuration of Piezo-ferroelectric Materials | T. Hungria *et al* | Applications of SPS in ceramics, reaction sintering and piezo-ferroelectric ceramics | [49] |
| 2009 | Electric Current Activated/Assisted Sintering (ECAS): A Review of Patents 1906–2008 | S. Grasso | Review of patents over 100 years | [45] |
| 2009 | Consolidation/Synthesis of materials by electric current activated/assisted sintering | R. Orru *et al* | Electric Discharge Sintering, Resistive Sintering, Different material systems, modeling | [37] |
| 2010 | Current-Activated, Pressure-Assisted Densification of Materials | J. Garay | Role of temperature, heating rate, pressure and pressure rate. Densification mechanisms and properties of Spark Plasma Sintered materials | [27] |
| 2010 | SPS for Multi-scale surface engineering | Mulukutla | Amorphous coatings for structural and biomedical applications | [50] |
| 2011 | Electric Current Activation of Sintering: A Review of the Pulsed Electric Current Sintering Process | Z. Munir *et al* | Role of current, current pulsation, temperature and pressure during SPS | [48] |

### *2.2.3 Role of Current in SPS*

In SPS, the electrical conductivity of the specimens plays an important role in defining the current and temperature distributions within the system. In case of ceramics or non conducting powders, the electric current is only expected to flow through the die materials (typically graphite) causing rise in the temperature of the die due to resistive heating, and the electrically non-conducting specimen's temperature will increase via heat conduction. Since all the materials used in this dissertation were electrically conducting metallic powders, this review will be more focused on the studies of the effect of current and temperature on electrically conducting powders.

Song *et al*. [3] believed that one of the consolidation mechanisms in conducting powders comes from the discharge between neighboring particles caused by pulsed DC input. This discharge will ionize the gas molecules thus forming plasma between the surfaces of particles. A concept of "self-adjusting mechanism" of powder microstructure was also proposed, which explains how current will always favor a path between particles with larger contact areas (due to their lower electrical resistivity) causing neck formation and temperature increase which will in turn affect the electrical resistivity in this neck region. The current will continue its flow through the neck region until the resistance coefficient becomes dominant and the resistivity of the neck region becomes higher than that of particles with smaller contact area, and this is when the electric current flow will switch to the smaller particles that were not favored first. The same group performed experiments later on where copper powder were heated to various temperatures using SPS with no holding time to show the effect of temperature

on neck formation (Figure 2.8) [4]. Such studies confined the role of current in only two branches; the first role is Joule heating of the surrounding die (which in turn conducts heat to the powder) which is responsible for the high heating rates, and the other is the formation of plasma between powder particles which enhances densification.

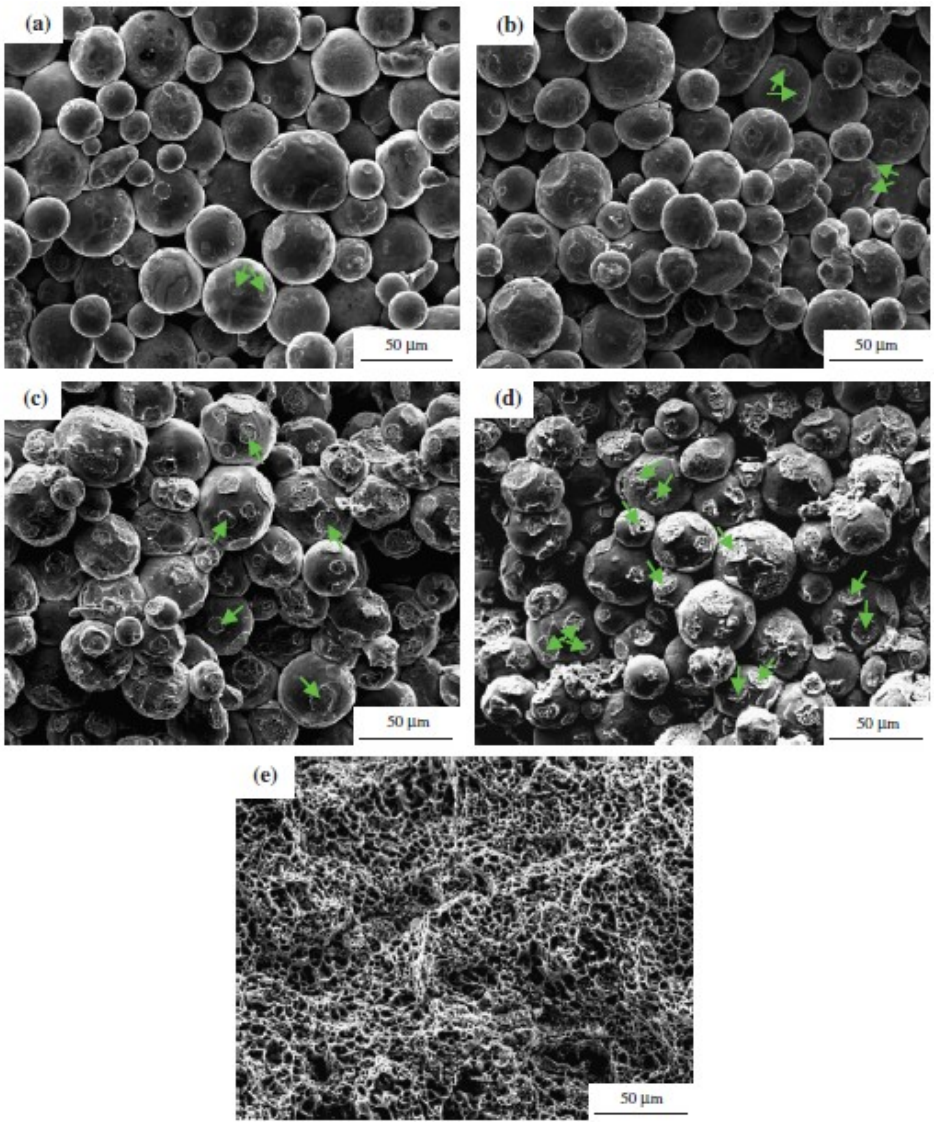


Figure 2.8 Neck formation at fractured surfaces of specimens sintered at temperatures of (a) 440°C, (b) 550°C, (c) 660°C, (d) 770°C and (e) 880°C [4]

More recently Hulbert *et al.* [51] investigated the presence of plasma using different techniques such as in-situ atomic spectroscopy, direct visual observation and ultrafast, in-situ voltage measurements (Figure 2.9). The experiments were performed on a wide range of materials and plasma generation was not indicated by any of the methods. To date, (to the best of the author's knowledge) no study was able to prove otherwise, hence, it is safe to assume that plasma in fact does not exist in SPS. However, the term SPS will still be used throughout this dissertation as it is still the most commonly used name both in research and commercial applications.

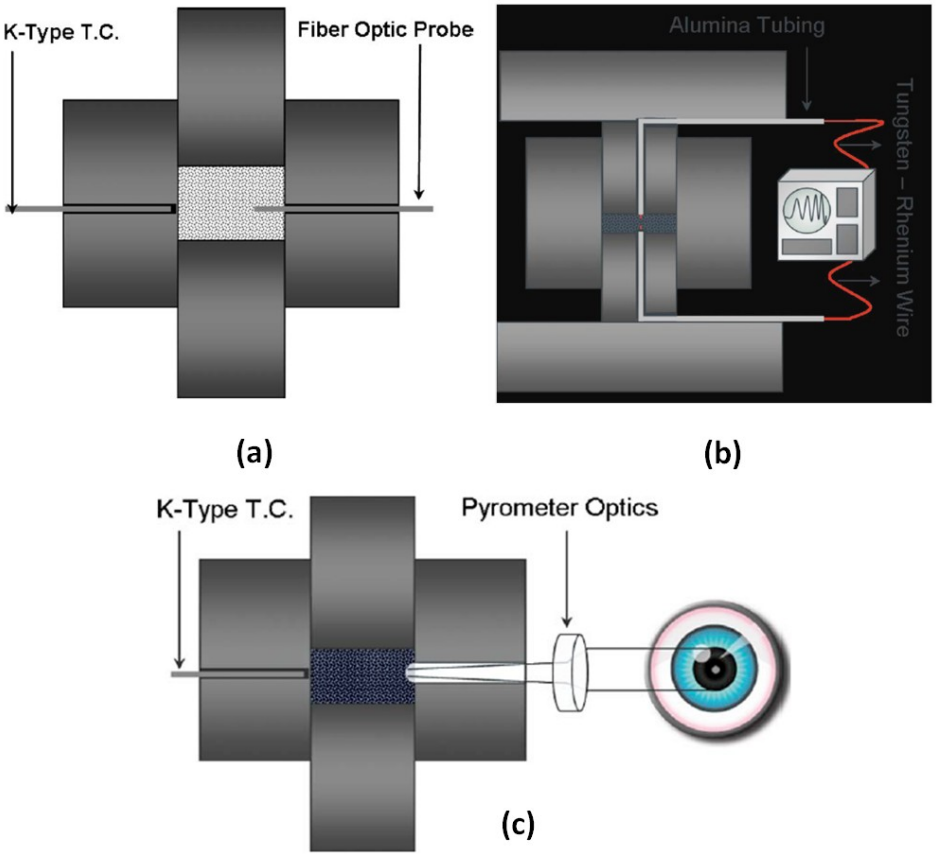


Figure 2.9 Different methods used to investigate the generation of plasma: (a) In-situ atomic emission spectroscopy, (b) ultrafast in-situ voltage measurement, and (c) direct visual observation [51].

Several studies later on focused on the intrinsic role of electric current which is believed to have a clear influence on materials processes through a number of studies. Conrad and coworkers [52,53,54,55,56,57] have a significant number of studies on the effect of electric field and current on crystallization, recrystallization, phase transformation, deformation, as well as studies on electroplasticity in solid materials. They demonstrated how high electric current densities play a role in enhancing the crystallization rate of amorphous materials as well as retaining a nanostructure by inhibiting grain growth through accelerated crystallization at lower temperatures. The effect of high current densities was also evident in enhancing the plastic deformation rate in metals due to electron wind effect and reducing the flow stress during superelastic deformation while hindering grain growth and cavitations. In fact it was reported that above critical current densities of 1,000-10,000 $A.cm^{-2}$, strain rates were observed to increase by orders of magnitude.

While the debate continues on the existence of plasma in SPS, one effect of electric current that remains persistent is the effect of electromigration on enhanced mass transport [5,47,58] which can be evaluated by the following equation:

$$J_i = -\frac{D_i C_i}{RT}\left[\frac{RT\,\partial \ln C_i}{\partial x} + Fz^*E\right] \qquad 2.2$$

Where $J_i$ is the flux of the diffusing $i$th species, $D_i$ is the diffusivity, $C_i$ is the concentration of the species, $F$ is Faraday's constant, $z^*$ is the effective charge on the diffusing species, $E$ is the field, $R$ is the gas constant, and $T$ is the temperature.

Several experiments were conducted in attempts to separate the intrinsic role of current from its thermal Joule heating effect. Bertolino *et al.* [59] built a setup where 127μm gold foils were sandwiched between 100μm aluminum layers and the effect of current on mass transport was tested by reacting the diffusion couples under electric current and without the application of current at the same temperature. Figure 2.10 shows a significant influence on phase formation under high current densities while there was no evidence of product layer formation when no current was applied.

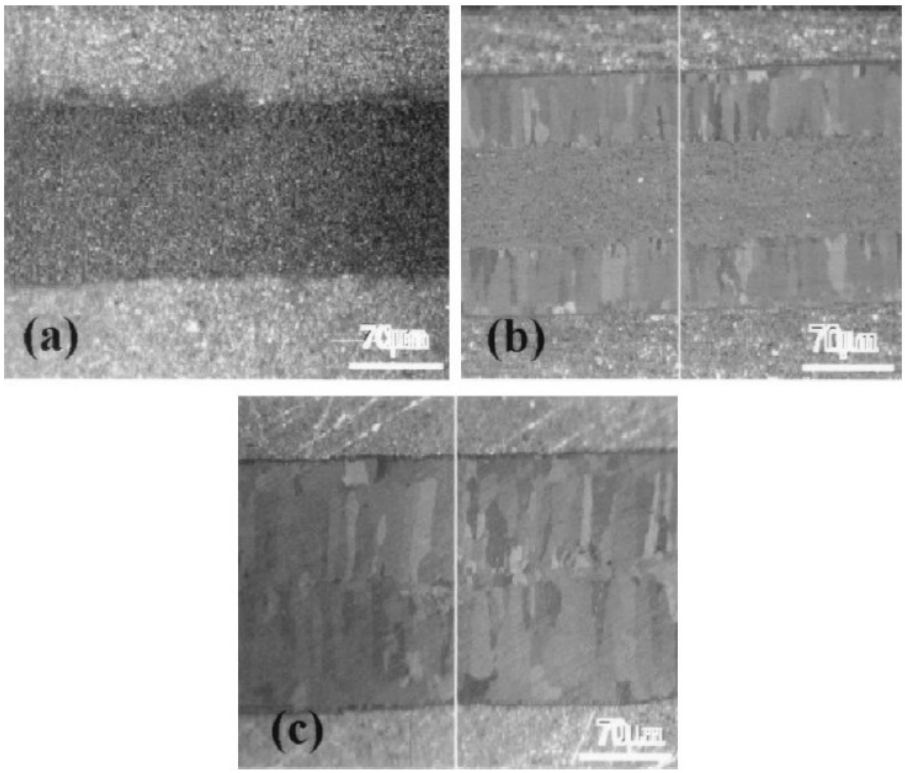


Figure 2.10 optical micrographs showing phase formation in the Al-Au-Al system held at 723K for 4 hours (a) under zero current, (b) under a current density of 509 A/cm$^2$, and (c) 1019 A/cm$^2$ [59]

In a similar study on a Ni-Ti system, analysis showed that the intrinsic growth rate constant in case of current activated annealing is 40 times higher than current free annealing in isothermal diffusion couples. Furthermore, the increase in current density resulted in an increase in the growth rate and a decrease in activation energy for the formation of the different phases in this system [6].

In a more recent study by Frei *et al* [5], the intrinsic effect of current on neck growth was investigated between 3mm diameter copper spheres and copper plates placed in a SPS apparatus (Figure 2.11) . Multiple layers of graphite foil were added to control the current density for the same amount of power generated. Figure 2.12 shows

scanning electron micrographs of the neck geometries on the copper plate at different magnitudes of electric current applied for the same duration at 900°C. The increase in neck size can be seen clearly and was attributed to electromigration.

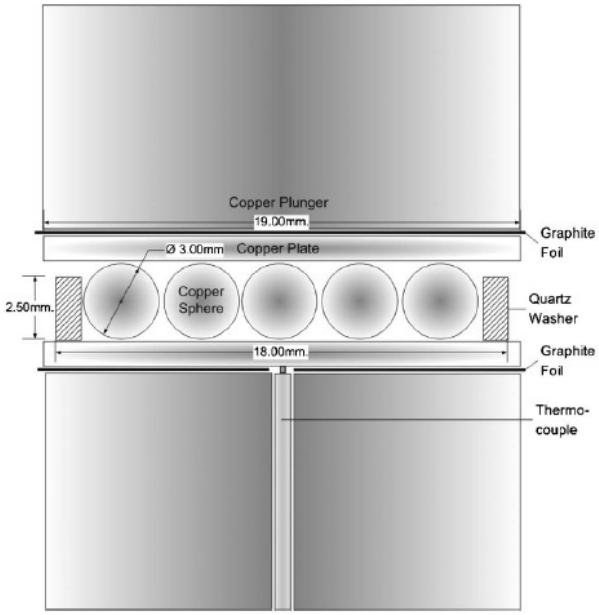


Figure 2.11 Schematic of copper spheres and plates geometry in a SPS setup [5]

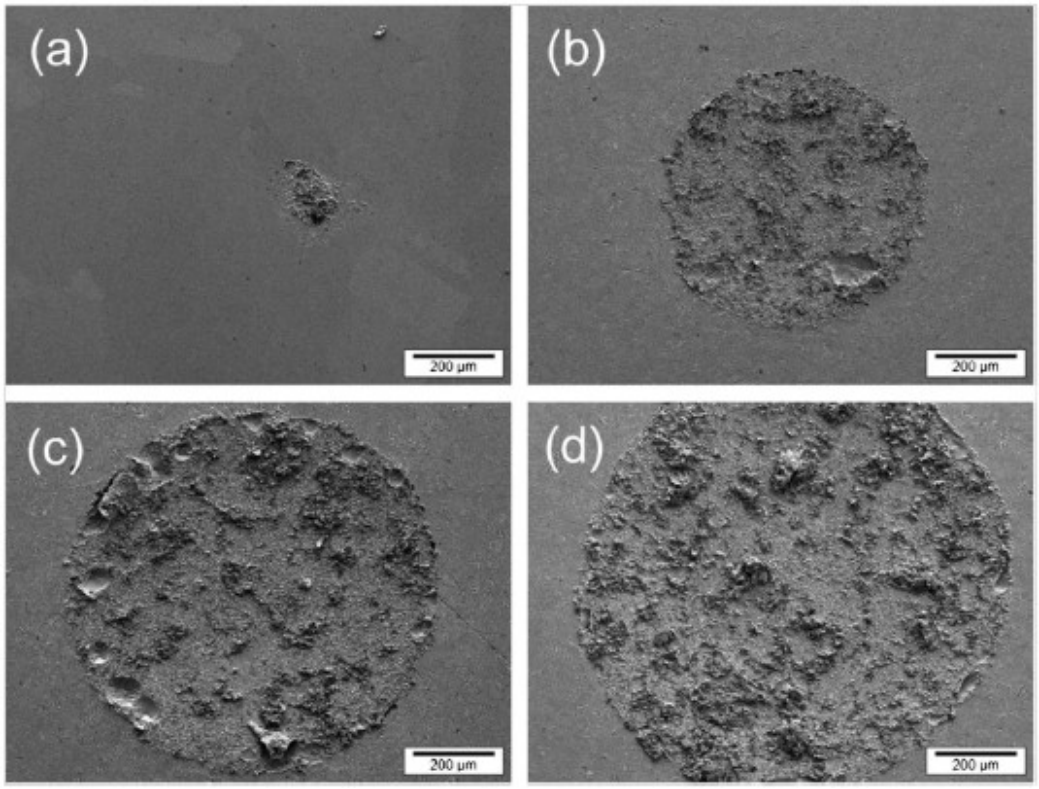


Figure 2.12 SEM images of neck geometry on copper plates sintered at 900C for 60 min.: (a) no current, (b) 700A. (c) 850A, (d) 1040 A [5]

### *2.2.4 Role of Current Pulsation*

The majority of commercially available SPS equipment has the capability to supply pulsed current in many different wave forms. Early investigations gave much credit to current pulsation when explaining the technique's superiority over conventional sintering methods. However, Nanko *et al* [60] reported a lack of effect of pulsed current on the sintering of Ni-20Cr powders while Xie *et al* [61] investigated the effect of different pulse frequencies (Figure 2.13) on the density and other different properties of aluminum powder compacts. It was found that no effect on the density or any of the microstructural properties investigated took place under all frequency configurations including 0 Hz frequency (continuous DC).

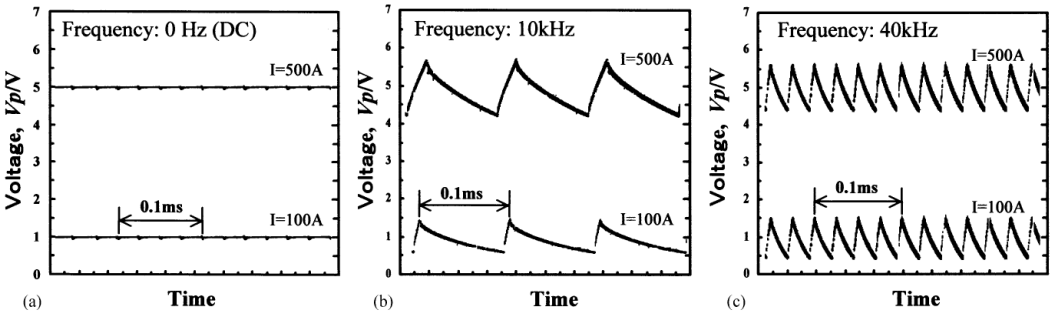


Figure 2.13 Different wave forms of heating and sintering currents in the SPS of aluminum powders. (a) 0Hz (DC), (b) 10 kHz, and (c) 40 kHz [61]

More recently Chen *et al* [1] investigated the effect of different pulse patterns (Figure 2.14) on the reactivity between Mo and Si layers as well as the effect of the directionality of the current and found out that the growth rate of the $MoSi_2$ product was independent of the pulse pattern and the electric current direction.

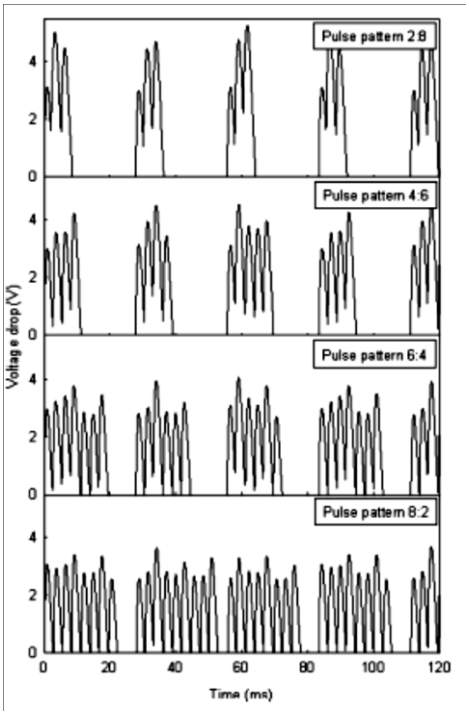


Figure 2.14 SPS pulse patterns for various on:off combinations used in the sintering of Mo and Si layers [1]

The previous results on the effect of electric current pulsation, together with the studies that ruled out the existence of plasma, brings us to the conclusion that pulsation during SPS is unnecessary as it has no effect on densification or microstructural properties.

### *2.2.5 Finite Element Models of the SPS setup*

Over the last few years, several simulation studies on SPS have been carried out. Garay [27] classifies the modeling and simulation efforts into two categories; (1) Modeling of the SPS system or apparatus and (2) Modeling of densification of materials. System models are mainly concerned with current, temperature and pressure distributions which could be very beneficial for estimating conditions that are difficult to measure in the system, while densification models help explain the densification mechanisms taking place during the process.

One of the earliest SPS modeling attempts was carried out by Zavalingos *et al* [31] where ABAQUS FEM software was used to perform a coupled electrical-thermal analysis while taking the thermal and electrical contact resistance into account. Experimental measurements were also performed for comparisons. The temperature of the specimen was found to be higher than that of the surface of the die showing a linear correlation between both temperatures. This allows for proper calibration of the specimen temperature when taking die surface temperature measurements (using a thermocouple or a pyrometer).

Vanmeensel *et al.* [62] also performed experimental as well as modeling analysis on fully dense conducting (TiN) and insulating ($ZrO_2$) materials and found the temperature in the SPS tooling and the specimen to be inhomogeneous. Hence, a temperature measurements method was proposed involving the use of a pyrometer focused on a borehole in the punch about 5mm away from the specimen center.

Anselmi-Tamburini *et al* [63] simulated temperature and current distribution for conducting (copper) and non conducting (alumina) fully dense samples by solving the fundamental joule heating equations:

$$\nabla.\vec{J} = 0, \qquad \nabla.\vec{f} + \rho C_p \frac{\partial T}{\partial t}\ h \tag{2.3}$$

Where $\vec{J} = \sigma\vec{E}$ is the current density ($\vec{E}$ being the electric field), $\vec{f} = -\lambda\nabla T$ is the heat flux density, $\sigma$ is the electrical conductivity, $\rho$ the density, λ the thermal conductivity, $C_p$ the heat capacity and $h = \vec{J}.\vec{E} = \left|\vec{J}\right|\left|\vec{E}\right| = JE$ is the heat generated per unit volume. Figure 2.15 shows the current density distribution in both investigated configurations. As expected, current does not flow through the non conducting alumina samples meaning that the sample will only heat up through thermal conduction from the die material. Figure 2.16 shows that it takes up to 100 s for the entire alumina specimen to heat up homogenously, it was also observed that the highest temperature occurred in the punch. On the other hand, the conducting sample (copper) experienced the highest current density through the sample body, which is also anticipated given the high conductivity of solid copper compared to graphite which is the material of the die. This

brings doubts about the similarity of current and temperature distributions to SPS of conducting materials in real life, as loose powders are expected to have much lower conductivities than the die material.

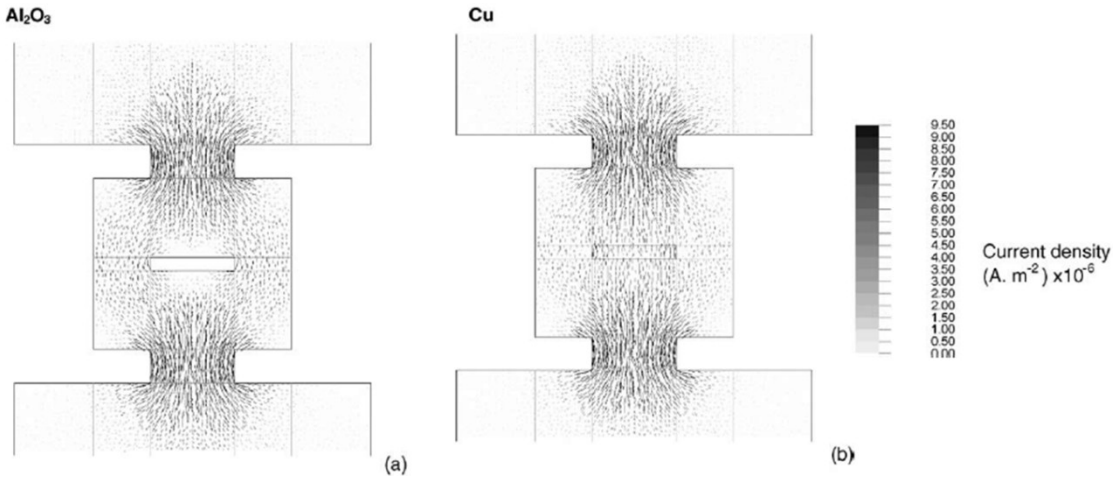


Figure 2.15 Electric current distribution in (a) alumina sample, and (b) copper sample [63]

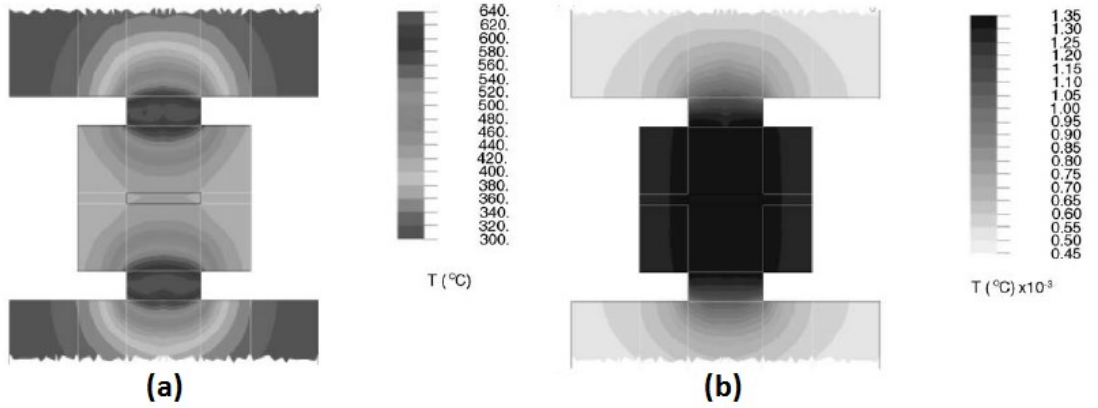


Figure 2.16 Temperature distribution in alumina samples under 4V of constant voltage after (a) 9 s and (b) 150s [63].

Cincotti *et al* [64] used a heuristic approach to model current, temperature and strain distributions in the SPS apparatus without powders and the results for the model were quantitatively in agreement with experiments. Wang *et al* [65] also used three-way

dynamic coupling of temperature, current distribution and mechanical behavior in the SPS system and investigated the effects on isotropic solid copper and alumina. Both temperature and stress (displacement) distributions depended largely on material properties. Figure 2.17 shows the stress distribution and gradient for both investigated material systems.

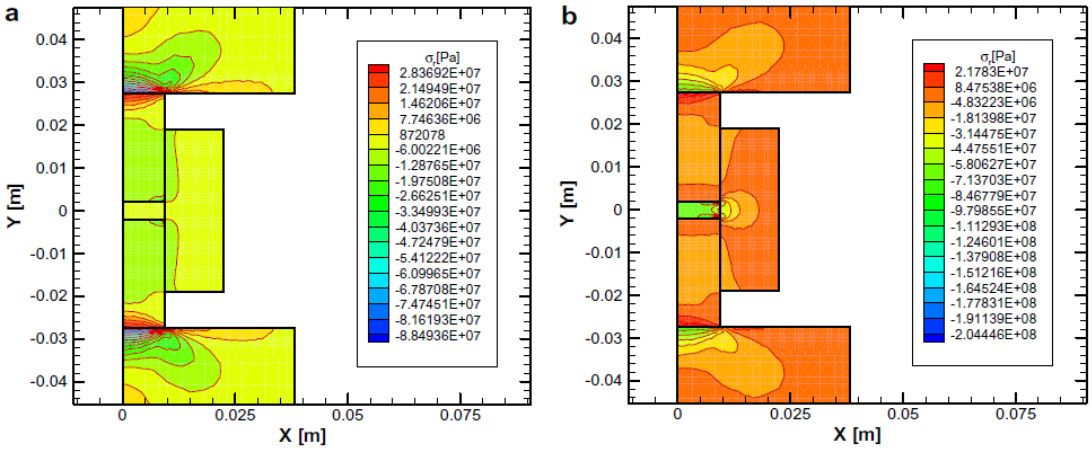


Figure 2.17 Stress distribution in the system with (a) alumina sample and (b) copper sample [65]

Tiwari *et al.* [66] considered various thermal conductivity values of powder compacts in a temperature and current simulation model using MATLAB and ABAQUS. They found that the temperature gradient between the specimen and die wall was largely dependent on the thermal conductivity of the powder compacts and the power input. More recent publications were focused on the simulation of current, temperature and stress distribution in the SPS system. In fact some of the published work was merely a recreation of existing models using different simulation packages such as the work by Mechigel *et al.* [67] where COMSOL Multiphysics was used to

simulate the exact same system developed in the models by Anselmi-Tamburini *et al*.[63] and Wang *et al*. [65].

Olevsky and Froyen [68,69] have made major contributions in the area of modeling of densification mechanisms in SPS. They analyzed the influence of thermal diffusion during SPS and found it to be significant especially for smaller particle sizes. In fact (within certain temperature ranges) it was found to compete with the contribution of external-pressure power law creep [68]. They also developed a constitutive model for SPS incorporating electromigration [69]. Olevsky *et al* [70] studied the effect of high heating rates in SPS and showed that there is an enhancement in consolidation under increased heating rates as the time that the specimen spends within the temperature range where surface diffusion is dominant is reduced. In this case grain boundary diffusion is favored resulting in increased densification.

## 2.3 Other SPS Related Processes

### *2.3.1 Spark Plasma Extrusion*

Early work that relates to this type of process, is a 1983 patent of a continuous extrusion apparatus that uses electric current for the uniform heating and simultaneous sintering and "continuous" extrusion of electrically conductive granulated materials [71]. In this patent the use of ceramic extrusion containers/tooling was suggested. The spark plasma extrusion of powder-based materials however remains an almost virgin area from the research stand point, with many opportunities for further development. The extension of spark plasma sintering to spark plasma extrusion can provide

important advantages. Among those is the ability to produce extended geometries in addition to potential grain refinement through material re-crystallization due to the effect of stress-induced deformation under the influence of electric current/heat.

It has been shown that high electric current density can decrease the flow stress of metals, and recent research [56] has focused on studying this effect and establishing a fundamental understanding of mechanisms involved. As mentioned earlier, it has been indicated that for critical current densities of 1,000-10,000 $A.cm^{-2}$, strain rates were found to increase by orders of magnitude. This may translate to powder processing, such that it may be possible that SPE can provide reductions in extrusion temperature and pressure requirements at some critical current density, compared to conventional hot extrusion.

In 2009 Morsi and El Desouky, conducted initial experiments on SPE of aluminum powders [23]. Unlike SPS, very high pressures are expected to be used for extrusion which rules out graphite as a possible material for the specimen container. H-13 tool steel was used for the container, die and die holder in the SPE rig for high maximum allowable pressure. The extrusion ram was made of WC-Co which has a relatively low electrical resistivity ($2x10^{-8}$ Ω.cm) and high compressive strength. Figure 2.18 shows a picture of the manufactured extrusion rig that was used for all SPE experiments at SDSU. Initially the aluminum powders were ball milled for a few minutes to break any insulating oxide layer that could be present around the powder which would otherwise prevent the flow of electric current during SPE. The milled

powders were then compacted with a sodium chloride (NaCl-table salt) surrounding to form a final green compact consisting of aluminum and an outer layer of NaCl salt (Figure 2.19), this layer provides electrical insulation from the walls of the container to ensure that the current will flow directly through the powders. Even though the extrusion process was successful under current, using salt as pressure transmitting medium was not effective in terms of porosity elimination and side extrusion (Figure 2.20).

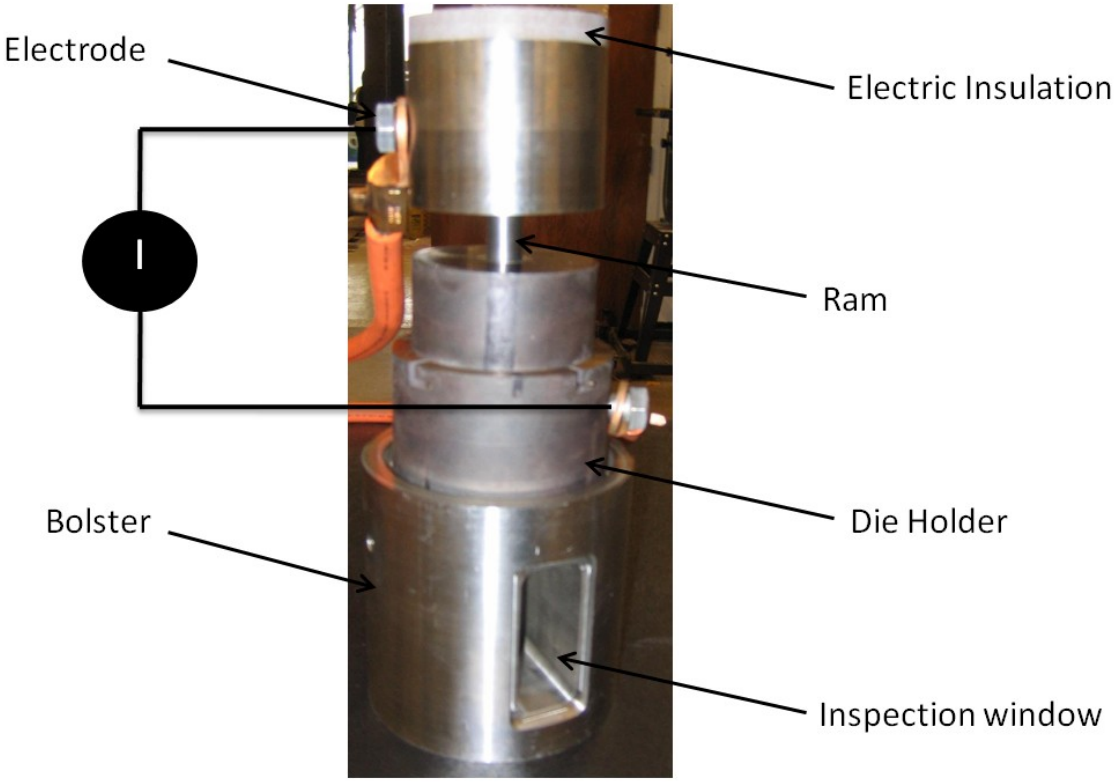


Figure 2.18 Extrusion rig designed and manufactured at AMPL

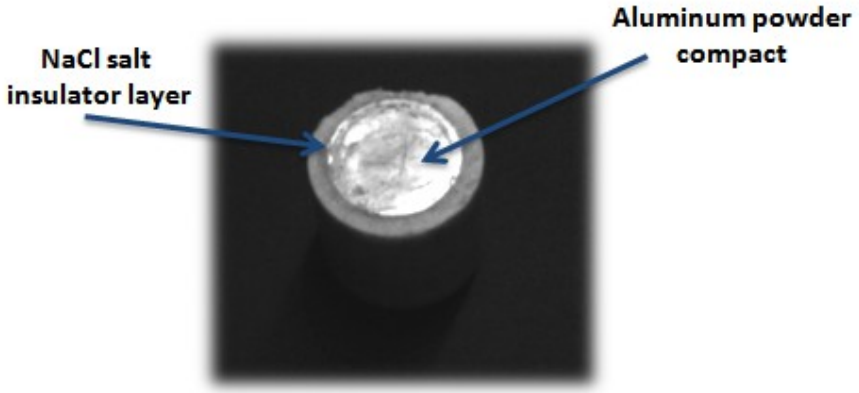


Figure 2.19 Aluminum powder compact with NaCl-Salt insulator layer [23]

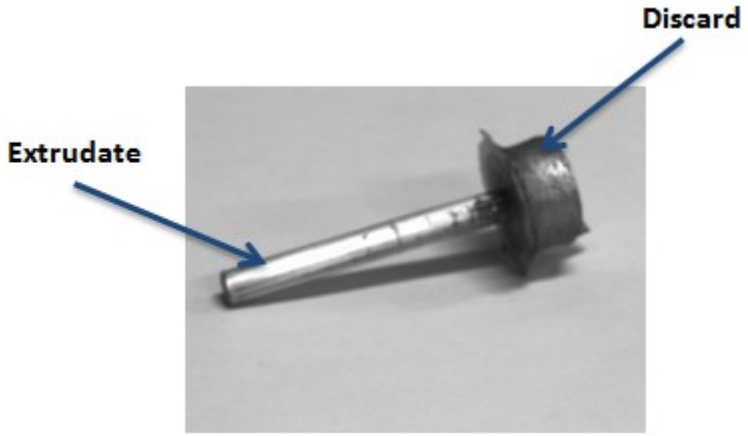


Figure 2.20 Product of SPE after dissolving the salt outer layer [23]

The feasibility of SPE was once again tested by Morsi *et al* [24] without the use of NaCl salt as an insulator, instead a thin flexible mica sheet was placed around ball-milled aluminum powder compacts and extrusion was performed under various temperatures measured through a K-type thermocouple embedded in the bottom of the specimen through the die opening. This time only 50% of the length of the compact was extruded. This way, each specimen would experience two different types of electric-

current processing; SPE in the extrudate and SPS conditions in the discard. Extrusion was only successful at onset temperatures of 350°C and higher for an extrusion ratio of 16:1 (Figure 2.21). Also materials subjected to SPS conditions displayed lower hardness and higher porosity levels than those spark plasma extruded; however, both displayed a reduction in microhardness with increase in extrusion onset temperatures due to possible dynamic recovery/softening processes (Figure 2.22, Figure 2.23).

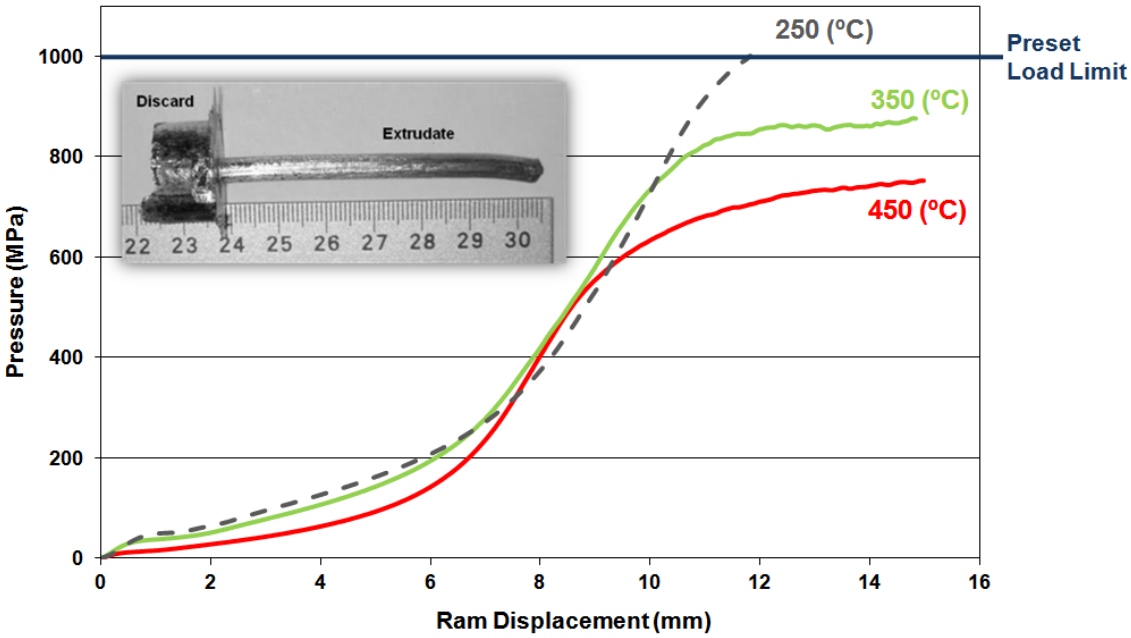


Figure 2.21 Pressure-Ram displacement curves for specimens extruded at 250°C, 350°C and 450°C and a picture of the extrudate (350°C onset temperature) with a centimeter scale

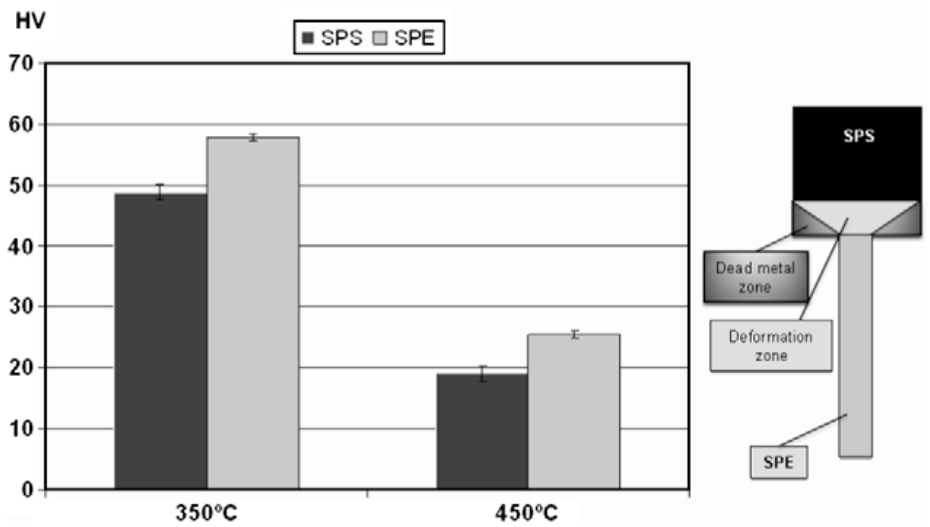


Figure 2.22 Average Vicker's microhardness measurements taken within different regions in specimens extruded at 350 and 450°C (error bars represent standard deviations) and a schematic of an extruded specimen showing typical regions in the discard and extrudate.

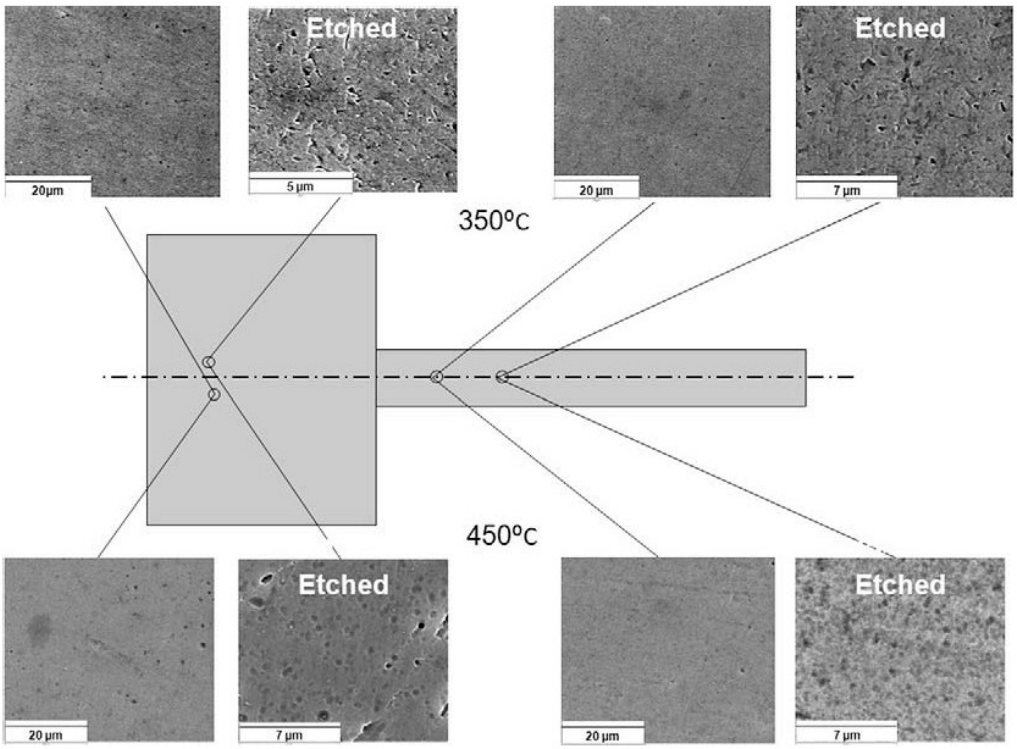


Figure 2.23 Electron micrographs taken of etched and unetched regions in the discard and extrudate of specimens extruded at 350 and 450°C

In other work by Morsi and coworkers [25, 26] aluminum–carbon nanotube composites were synthesized by SPE. The extrusion of the composite was successful and showed enhancement in both hardness and compressive strength [26]. Although no clear reduction in pressure or temperature requirements were observed, this may not be surprising since the experiments were conducted at current densities lower than those indicated to cause such behavior. It was however suggested that a continuous powder-based wire/fiber extrusion should yield extremely high current densities, to enable such effects.

### *2.3.2 Spark Plasma Sintering-Joining (SPS-J)*

In addition to its previously mentioned advantages, SPS proved to be a successful bonding technique for joining as well as coatings. Similar to regular SPS, joining and coating involve the passage of direct current through layers of similar or different materials. In case of joining, graded material interlayers can be present to reduce thermal expansion effects, and it has been used to fabricate metal-metal [59,72], ceramic-ceramic [73], metal-ceramic [74], Semiconductors [75], nanocrystalline and reactive joints [76].

Joining of intermetallic/ceramic functionally graded layers and metal alloys was investigated by Xu et al [74] where 316L stainless steel and $MoSi_2$ layers were joined together using SPS technique. The production of such joints was successful when several graded interlayers were used to overcome the differences in thermal expansion coefficient (Figure 2.24). Prior to this work, the joining of $MoSi_2$ and steel was not

possible due to high joining temperature requirements and the difference in thermal expansions coefficient. This work capitalized on SPS advantages such as reduction in thermal stresses and the simplicity of producing graded material interlayers. Figure 2.25 shows a microstructural image of the $MoSi_2$/316L joint. Fan *et al.* [77] investigated the process of joining $CoSb_3$ binary skutterudite to molybdenum electrode using SPS. The joining was successful by inserting a titanium interlayer which formed a composition gradient alloy layer at the Ti-Mo boundary and an intermediate layer of TiSb at the Ti-$CoSb_3$ front (Figure 2.26).

The feasibility of ceramic-ceramic joints made of Yttrium (Y) and Ytterbium (Yb) doped α-SiAlON using SPS were investigated in a recent study by Limeng et al [73]. The bonding was successful without the use of interlayer material and the joints (free from residual stresses) showed flexure strength similar to that of the parent material. Joining Aluminum foam and solid aluminum is an example of metal-metal joining using SPS. Researchers at the Korea Institute of Industrial technology reported that at higher holding times, the tensile strength of the Al foam-Solid Al joint was higher than that of the Al foam [72].

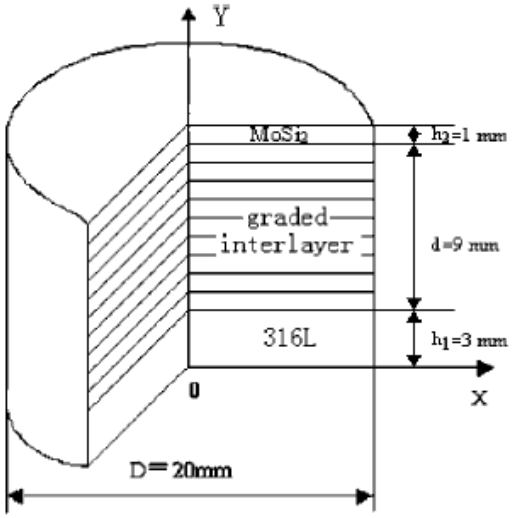


Figure 2.24 Dimensions and distribution of graded interlayers [74]

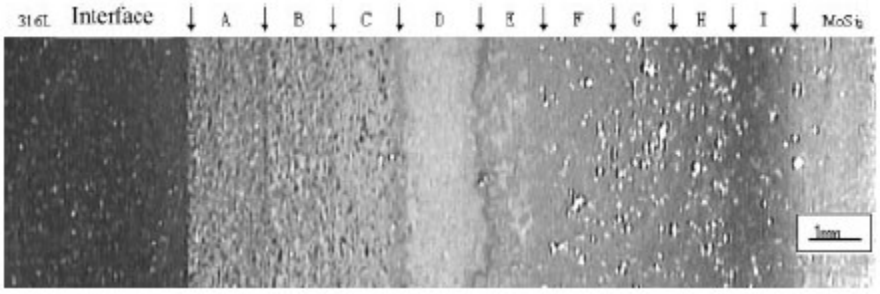


Figure 2.25 Optical microstructure of the $MoSi_2$/316 L joint [74]

Liu and Naka [76] investigated the effect of SPS on the in situ joining of nanocrystalline reactive systems where mechanically alloyed nanocrystalline $Ni_3Al$ and $Ni_3Al$-40%TiC joints were fabricated. The resulting joints were found to be fully dense with $Ni_3Al$ and TiC being the only phases present in the joint (Figure 2.27). The nanocrystalline structure was also preserved and the final joint was without cracks or void defects.

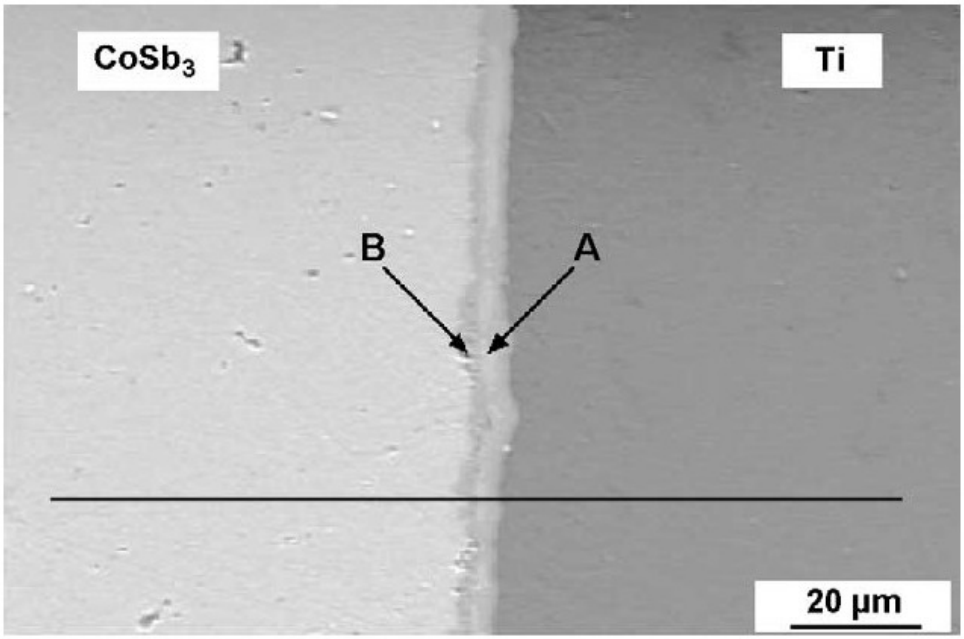


Figure 2.26 SEM of joint interfaces of $CoSb_3$/Ti, area "A" is a TiSb compound and area "B" is believed to be the ternary compound of Ti-Sb-Co [77]

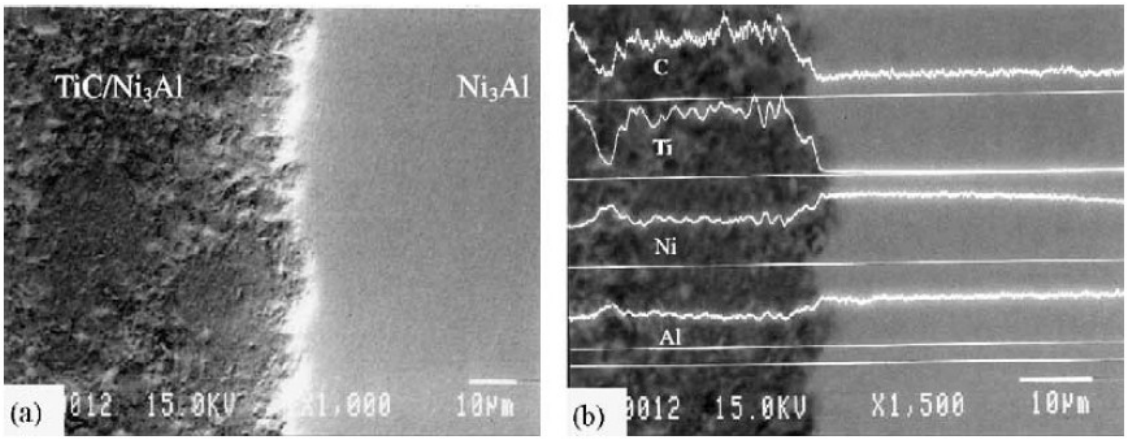


Figure 2.27 Ni3Al and Ni3Al-40vol% TiC joint at 1100C for 5 min. (a) SEM image (b) line scans of the elements accross the joint interface [76]

Kim et al [75] used SPS to join p-type and n-type Bi-Te materials. The resulting mutual atomic diffusion layer across the p-n junction was only 2µm thick (4% of the thickness produced by hot pressing of p-n interface). Also in situ metallization during SPS reduced the resistance of the p-n interface.

### *2.3.3 Current Activated Tip-based Sintering (CATS)*

Despite the numerous advantages reported in SPS, SPE and Electric Rolling, they have so far been predominantly limited to the production of bulk or continuous macro-scale features. Also the electric current requirements are considerably high especially for larger size specimens. Researchers at San Diego State University developed and patented a novel process where direct electric current is passed through a conducting tip that is either stationary or moving along the surface of a conducting powder compact to enforce localized sintering. This selective sintering process is called current activated tip-based sintering (CATS) [28]. The control of tip size, path, speed, and shape adds great versatility to the electric current processing of powders. CATS has the potential of extending to 3D fabrication as well as micro and possibly nano-scale sintering, in addition to the macro-scale applicability which enables a versatile scalability option for current activated processing of large structures. Furthermore, higher current densities than conventionally possible were reported with minimum energy input due to the relatively small size of the used tips.

The validity of the process in localizing SPS effects was investigated by Morsi et al. [78]. Results showed that microhardness for nickel powder compacts and the depth of sintering significantly increases after 5 duty cycles (2s on: 10s off) at a nominal current density 12,732A/cm$^2$ (Figure 2.28). Figure 2.29-A shows a scanning electron micrograph of the specimen's cross-section beneath a 1mm tip. Cracks that separate the sintered region from the remaining green compact were observed due to shrinkage, this was confirmed with microhardness tests shown in Figure 2.29-B where

the microhardness values of points A,B,C and D (inside the sintered region) are significantly higher than the hardness of point E which has the same value of the green compact hardness. Preliminary investigations were also conducted on a moving tip configuration where AC current was applied through a 0.02 mm copper tip. Shrinkage was observed in the nickel but porosities were still present in the sintered regions which were limited to 50 µm below the surface.

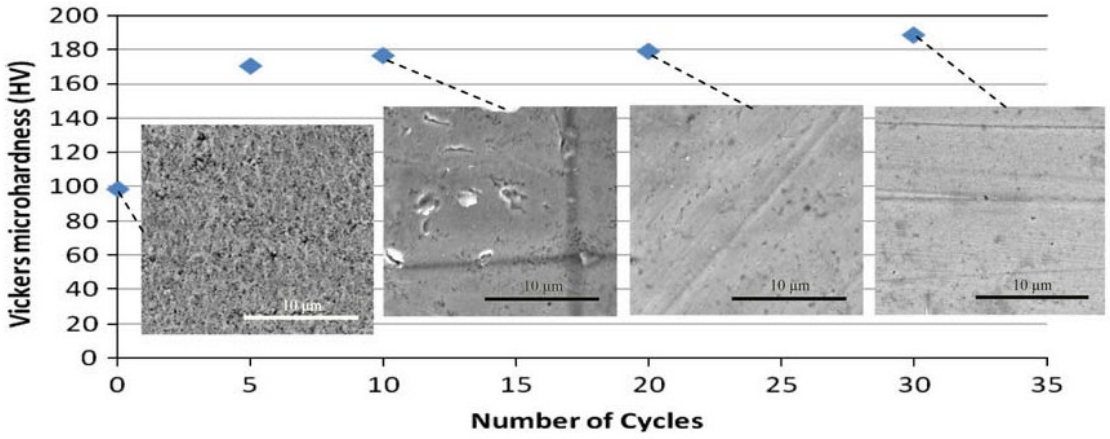


Figure 2.28 Effect of number of cycles on the hardness of nickel sintered locally with a 1mm tip [78]

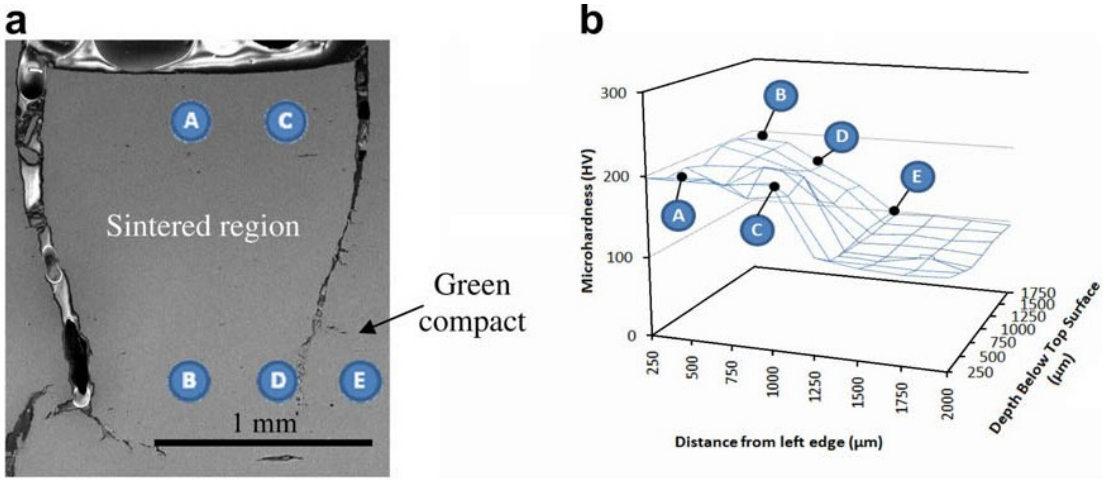


Figure 2.29 SEM of the cross-section beneath the CATS tip (a) and the corresponding hardness map (b) [78]

A great deal of work has been done by the CATS group at the advanced materials processing lab (AMPL) at San Diego State University such as the effect of tip speed, current density, tip pressure and tip shape as well as the study of the application of CATS on different material systems [79,80,81,82,83,84,85]. The effects of tip speed and number of tip passes were investigated [79] where a 0.5mm tip was allowed to travel at velocities of 0.42, 2.1, 8.4 and 16.9 mm/sec over a nickel powder compact for a single pass, and the experimented was later on repeated at a 2.1 mm velocity for a various number of passes. Figure 2.30 shows the effect of the number of passes on microhardness of the sintered region. It is clear that densification takes place after a single pass and microhardness of the material increases with increasing the number of passes at levels 125μm and 300μm beneath the surface. Investigation of the tip speed showed that higher densities were achieved at lower tip speeds (after one pass) as the exposure time is prolonged. In another study, the effect of tip pressure in stationary CATS was investigated [80], where different pressures were applied on the CATS tip for different current exposure times. The applied pressure had a significant effect on the Vickers microhardness of the specimens as it was found to increase with increased applied pressure regardless of the current exposure time. However, the applied pressure had little to no effect on the porosity levels of the sintered specimens.

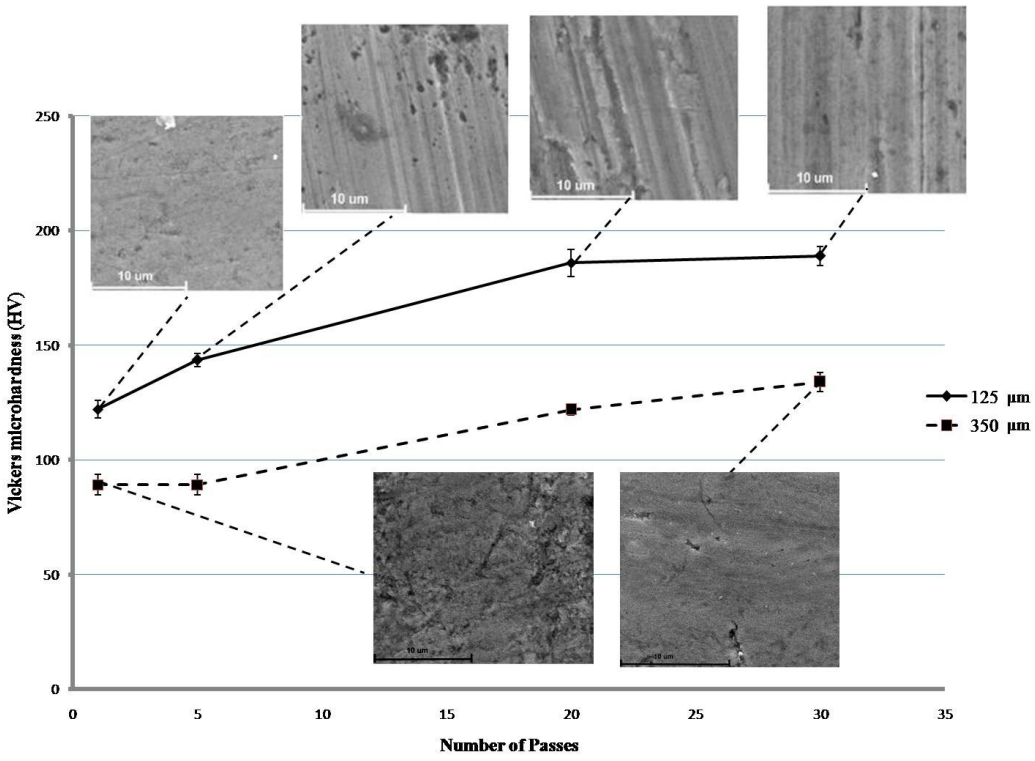


Figure 2.30 Effect of number of passes on the Vickers microhardness at 125 µm and 350 µm beneath the tip/specimen interface [79].

Other work by the CATS group demonstrated the versatility of CATS by using a pre-formed tip of a complex shape (Figure 2.31 CATS pre-formed tip [81]) [81]. Current densities of up to 5,000 A/cm$^2$ were applied through the forming tip under various tip pressures to find the optimum current density/pressure combination. For this particular experiment the application of higher pressures was desirable to enhance localization. Furthermore, the depth of the sintered artifact increased with the increase of current density input. (Figure 2.32) shows a photograph of a sintered shape on a nickel powder compact.

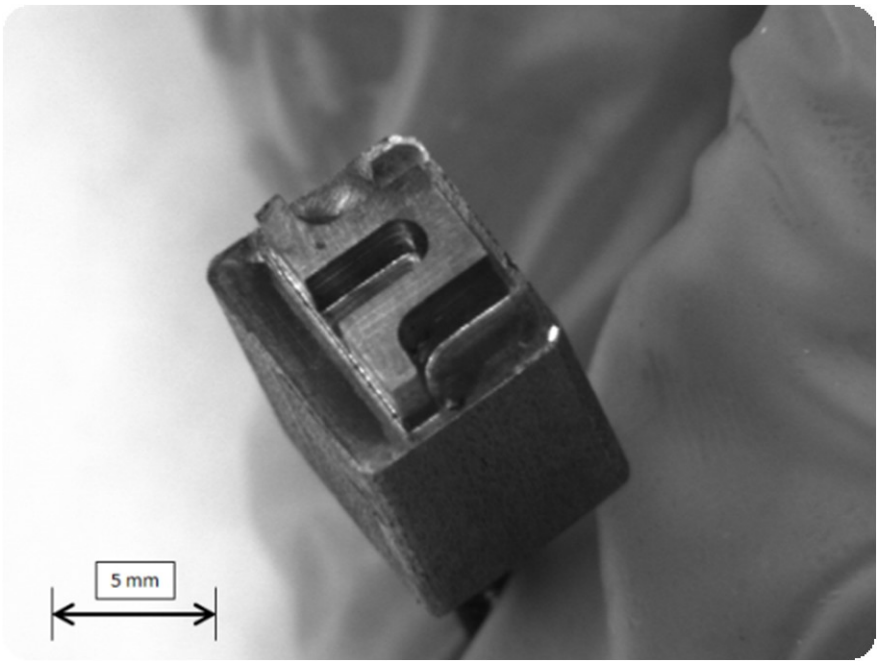


Figure 2.31 CATS pre-formed tip [81]

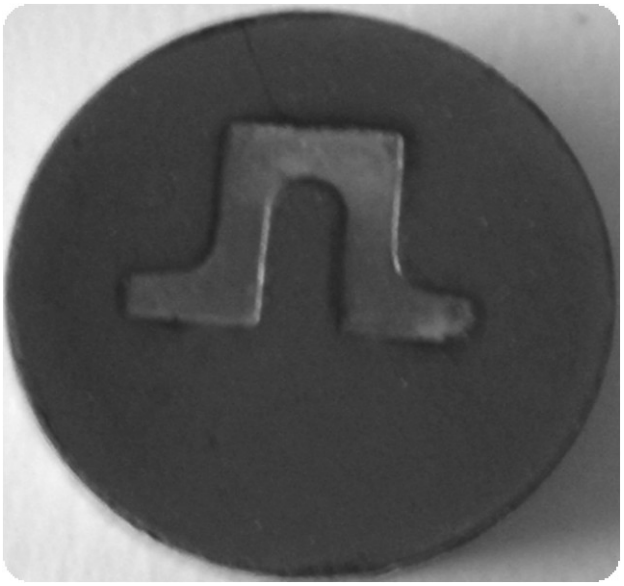

Figure 2.32 Sintered shape on a nickel powder compact, sintered at 5,000Acm$^{-2}$ [81]

Patel *et al* [82] used CATS to locally sinter mechanically-alloyed amorphous NiTi powders at different current densities and current exposure cumulative time. The current was applied through a 1mm tip on cycles (1s on, 11s off) to reduce heat transfer outside

of the process zone. Figure 2.33 shows the effect of number of cycles (i.e. current exposure time) on the porosity (measured at 250 µm beneath the surface) and it can be seen that near full density was approached when the specimens were exposed to 70 or more cycles. The area of the highly densified local regions underneath the tip also increased with the increase in number of cycles (Figure 2.34). The increase in the size of the process zone was explained by the development of a highly consolidated progressive region under the tip which will act as a highly conducting medium, transferring sintering conditions to the significantly unsintered (more resistive) areas beneath it. This will consequently be repeated as sintering progresses through the thickness of the powder compact.

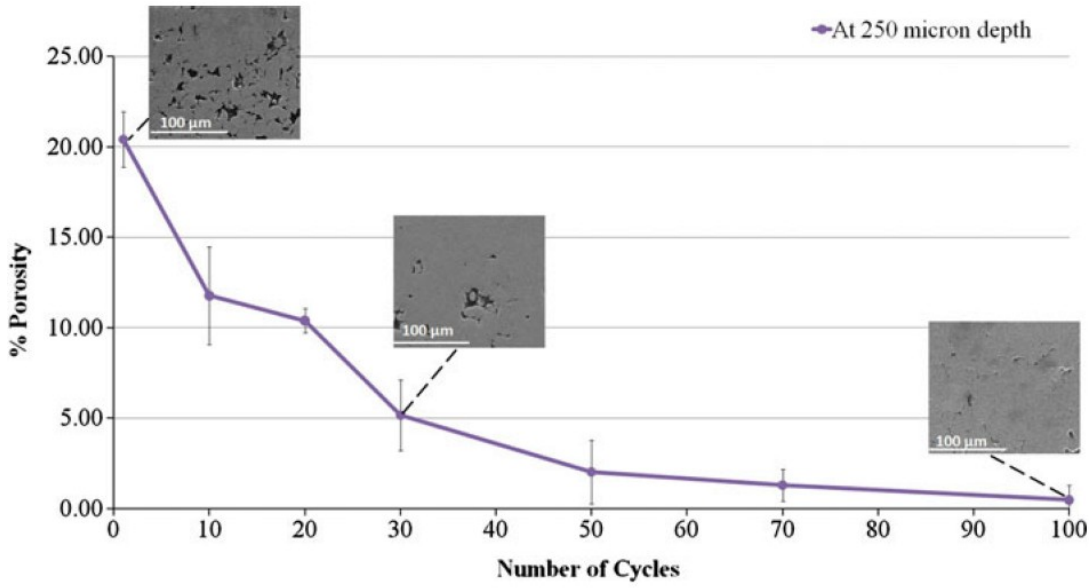


Figure 2.33 Effect of number of cycles on the pore content [82]

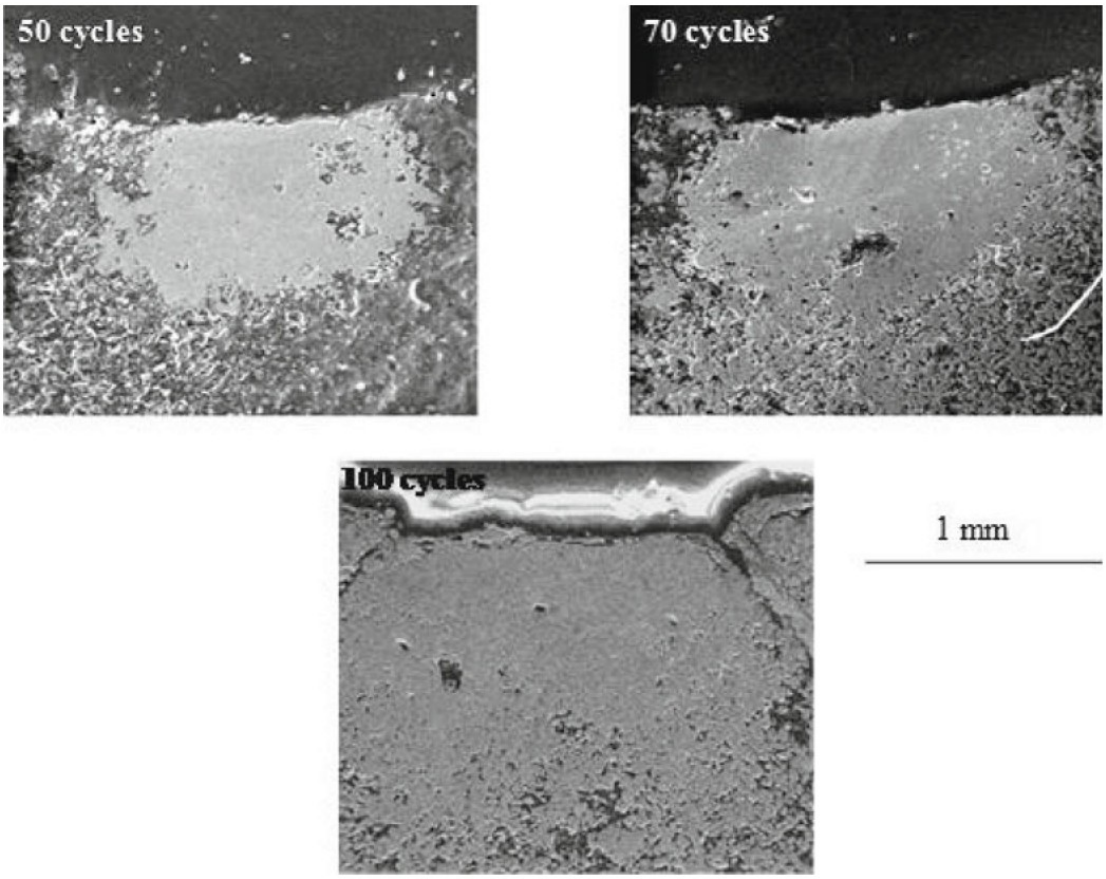


Figure 2.34 Scanning electron micrographs of the process zone beneath the tip after 50, 70 and 100 cycles at a current density of 12,700 A/cm$^2$ [82]

CATS of reactive Ni/Al powder compacts was recently investigated by Numula et al. [83,84], where mixed Ni and Al powders were subjected to high current densities through a CATS 1mm tip to initiate a combustion synthesis type reaction and rapidly form nickel aluminides intermetallics. Figure 2.35 shows the process progression when a continuous current of 200A was applied. A self propagating high-temperature synthesis (SHS) type reaction is believed to be triggered at 16.45 s (Figure 2.35-F) as this is the time where radial cracks start to form, after which wave propagation can be observed as the entire specimen is lit up (Figure 2.35-H) after less than 0.5 s. Further microscopic examination using backscattered scanning electron microscopy revealed a

multiphase microstructure (Figure 2.36). It should be also noted that various current inputs were investigated (100, 200 and 300A) and the reaction was only triggered for the 200 and 300A configurations.

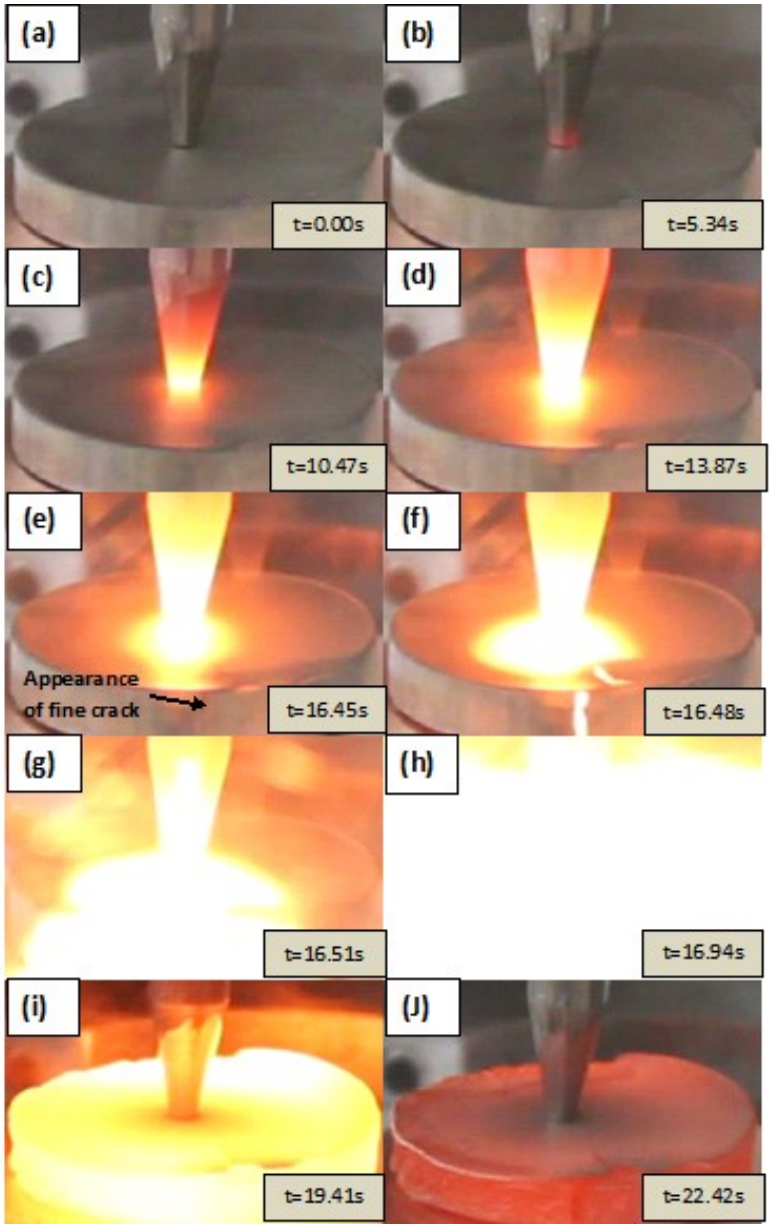


Figure 2.35 Progression of the reaction in Ni-Al powder compact under CATS (200A, 1mm tip) [84]

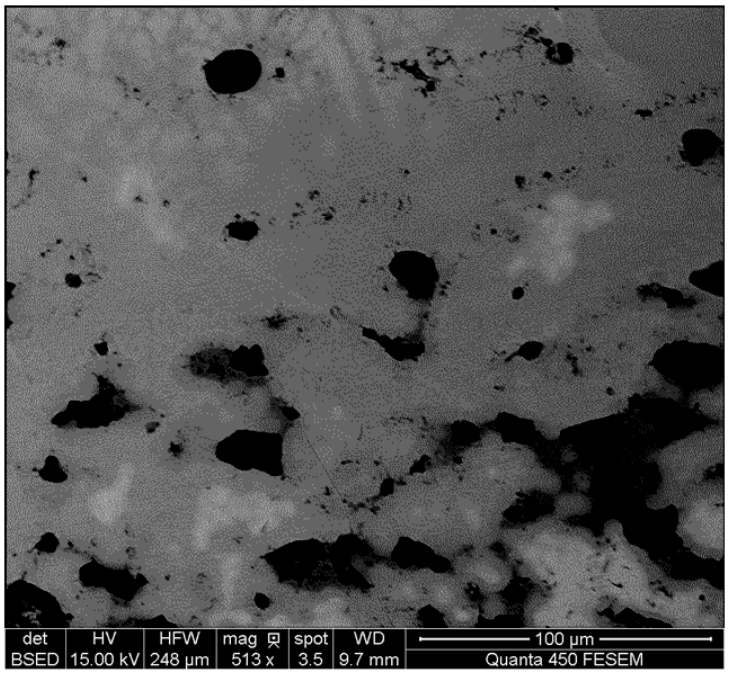


Figure 2.36 Backscattered scanning electron micrograph of reacted Ni-Al intermetallic compound. The dark grey areas are $Ni_3Al$ and the lighter areas are unreacted regions of predominantly nickel [84].

## 2.4 Production of Functionally Graded Materials

Functionally graded materials (FGMs) have been made for many decades, and have the special feature of a spatial change in composition [86,87,88], grain size [89, 90,91], or porosity [92,93,94,95]. The powder metallurgy approach can be well suited for the production of these types of materials. One of the basic approaches is to sequentially deposit or add different powder layers of varying compositions [96,97], particle size and/or pore content [90] followed by full or partial consolidation at high temperatures. Despite its advantage in terms of simplicity, it involves multiple powder deposition steps and the approach is prone to processing defects such as layer delamination/interface cracking [90] upon sintering which may result from differential shrinkage

### *2.4.1 SPS of Functionally Graded Materials*

SPS has been used recently as an approach for the consolidation of FGMs. One of the most popular SPS applications in FGMs is the production of crack-free multilayer composites [96,97, 98,99,100,101]. Jin *et al* [98] used SPS to sinter mullite/Mo sequentially stacked layers of powder. Figure 2.37 shows the FGM product where the layers boundaries can be seen clearly with no delaminations or defects.

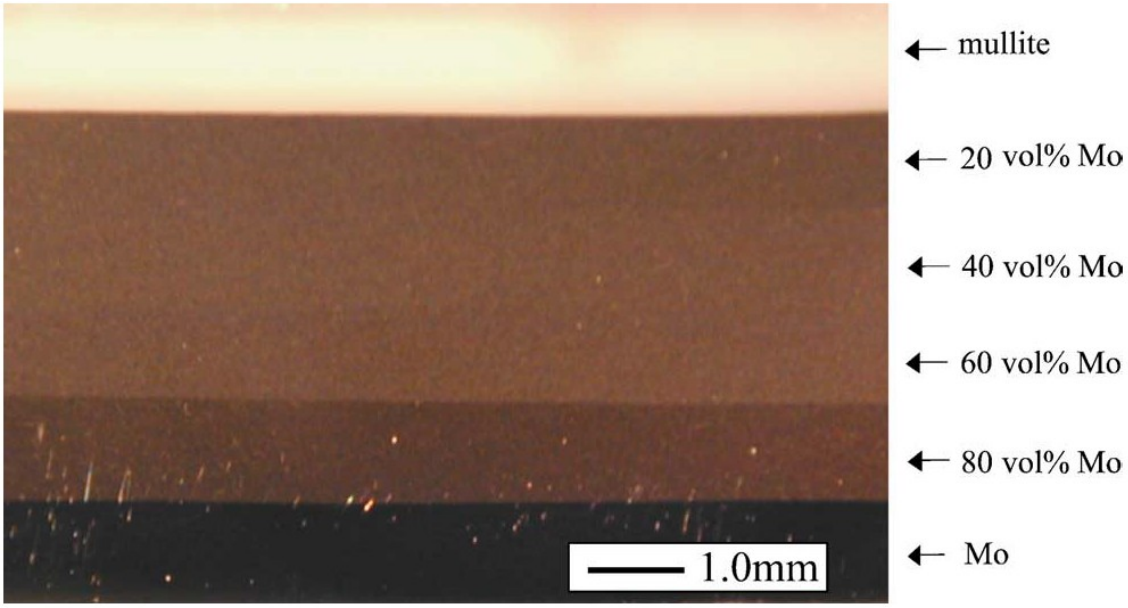


Figure 2.37 Optical micrograph of the mullite/Mo FGM [98]

Within the context of porous FGMs, SPS has recently been used to produce functionally graded porous tungsten macro-scale structures (which were later infiltrated with aluminum following SPS) using a prior powder segregation technique of bimodal powders [92]. Figure 2.38 shows the porous microstructure after being infiltrated with copper. Watanabe et. al. [93] also spark plasma sintered titanium-sodium chloride (NaCl) composites after which the NaCl was dissolved out to produce functionally

graded porous titanium microstructure ready for subsequent infiltration with biodegradable poly-l-lactic acid fibers.

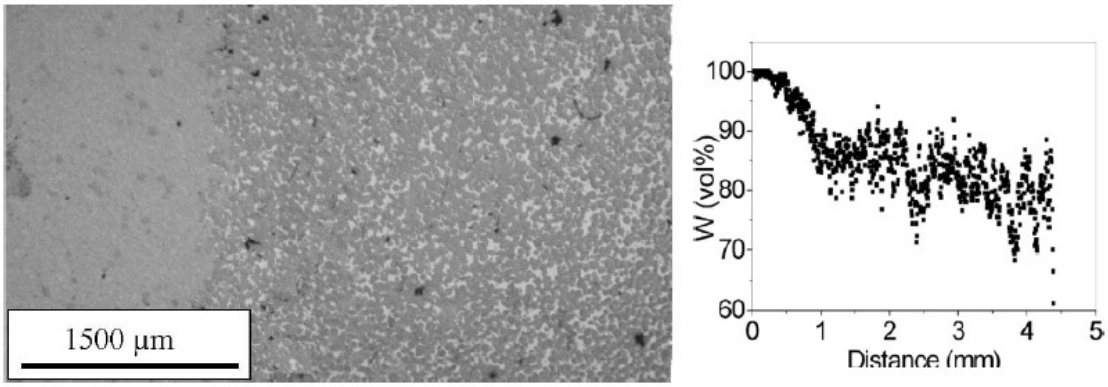


Figure 2.38 Evolution of the microstructure of self-formed tungsten structure vibrated for 120 minutes and sintered at 1723K. The structure was subsequently infiltrated with copper. The corresponding tungsten volume percent is presented on the right hand side [92]

One of the techniques recently used to produce porous FGMs by SPS is the offset die method used by Hulbert *et al* [94] and Holland *et al* [95]; where the powders are loaded in the SPS die in an offset manner as shown in Figure 2.39. The shift in position of the plungers creates a thermal gradient along the length of the specimen which could lead to different densification levels. In the first study reactive mixtures of amorphous boron and carbon powder were used to produce macro-scale porous $B_4C$ FGM using offset-SPS which were later infiltrated with aluminum [94]. Figure 2.40 shows a cross-section of the porous FGM product. In the other study 15 mm long and 9 mm thick $B_4C$ tubes were produced using an SPS configuration that generates a steep temperature gradient enabling a steep radial microstructural variation across the outer thickness of the cylinder [95], to produce macro-scale cylinders with functionally graded porous surfaces.

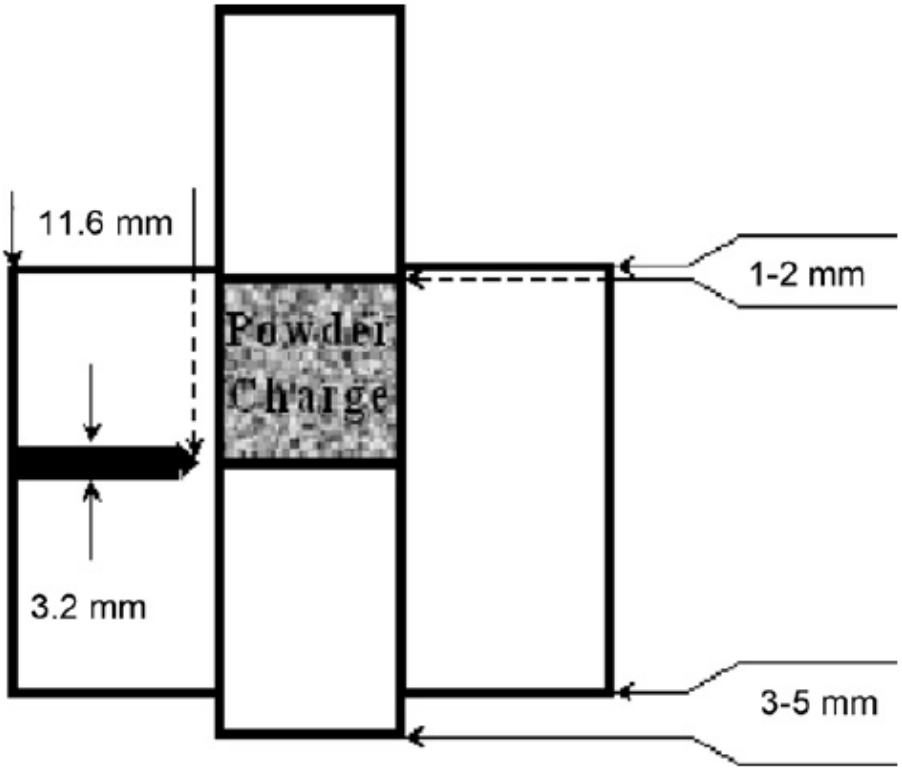


Figure 2.39 A sketch showing SPS die and punches offset-setup [94]

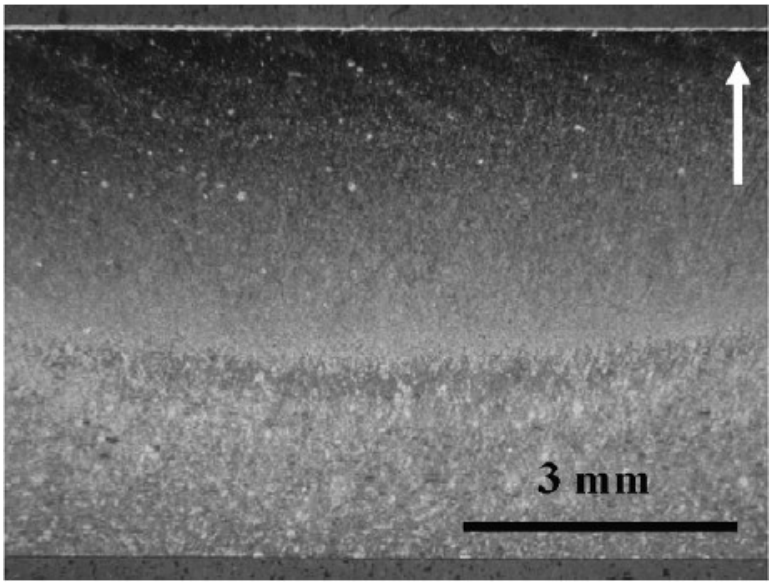


Figure 2.40 A cross-section of the porous B4C FGM before aluminum melt infiltration [94]

# 3 SCIENTIFIC NOVELTY

This study focuses on Current-Activated Tip-based Sintering (CATS) of metallic powders where several unexplored fundamental issues are tackled. The work in this dissertation has the following scientific novelties:

1. Experimental investigation of temperature evolution in CATS.
2. Development of a finite element model to generate surface and subsurface temperature profiles in CATS.
3. Investigation of the effect of green density of powder compacts in CATS
4. Investigation of the effect of the initial particle size of powders in CATS
5. Generation of micro-scale porous functionally graded materials with detailed characterization of the spatial pore content and pore size distributions.
6. Production of micro-scale consolidated features of extended geometry using micro-scale moving CATS.
7. First investigation of tip/particle size relations in CATS

# 4 EXPERIMENTS AND METHODS

## 4.1 Powder Preparation and Compaction

Nickel powders used in the experiments were manufactured by Inco Co. with different particle sizes and morphologies (Table 4.1 Nickel powders size and shape). Figure 4.1 shows a scanning electron micrograph of the INCO 123 and INCO 210 powders. For the moving tip experiments, copper powders with different particle size were used. 500nm copper (nano dynamics Co.) was used for the effect of current density and tip speed experiments while copper powder from GFS chemicals Inc. with particle size (50% through -325 mesh) was sieved to obtain powders that are over 45μm and under 45μm in size for the effect of particle size and effect of green density experiments. Thin weighing paper is first placed on a high precision balance with 0.0001 gm accuracy (Figure 4.2) and then the powder is placed on the weighing paper (taking the tare weight into account). A Carver steel die (12 mm inner diameter) setup shown in Figure 4.3 was used for powder compaction. Pressure pads were ground and polished to the 0.02 μm level to make sure the powder compact surface is smooth prior to CATS. Before the powder is placed in the die, the inner surface of the die, the punch and pressure pads are all cleaned carefully with acetone. The powder is then placed into the die followed by the pressure pad and the tool steel punch. The entire assembly is then placed into a hydraulic Carver Press (Figure 4.4) and compaction pressure is applied and maintained for 10 seconds. Following the release of pressure the die base is removed and an ejector is placed instead and the assembly is once again placed in the

hydraulic press to release the powder which is now a green compact. Figure 4.5 shows an example of a nickel green compact.

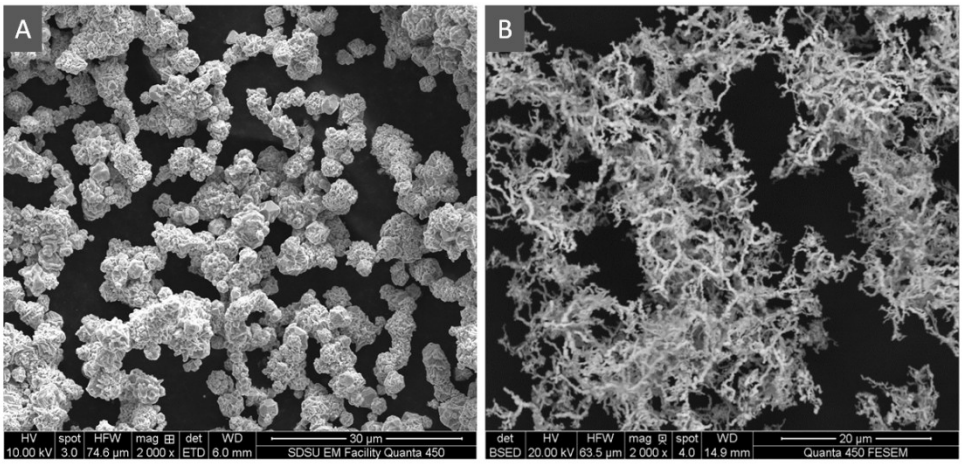


Figure 4.1 Scanning electron micrograph of (a) INCO 123 and (b) INCO 210 nickel powders

Table 4.1 Nickel powders size and shape

| **Type** | **Size (µm)** | **Shape** |
|---|---|---|
| 123 | 3-7 | Spherical with Spiky, needle-like texture |
| 110 | 1-2 | Spherical |
| 210 | 0.5-1.0 | Filamental |
| 210h | 0.2-0.5 | Filamental |

Figure 4.2 High Precision Balance

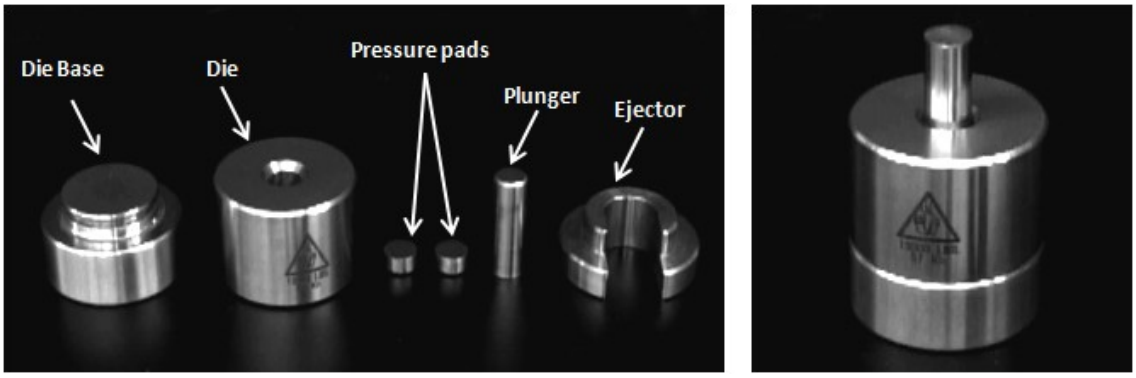


Figure 4.3 Components of the Carver tool steel die (left) and the full die-assembly (right)


Figure 4.4 Carver hydraulic press

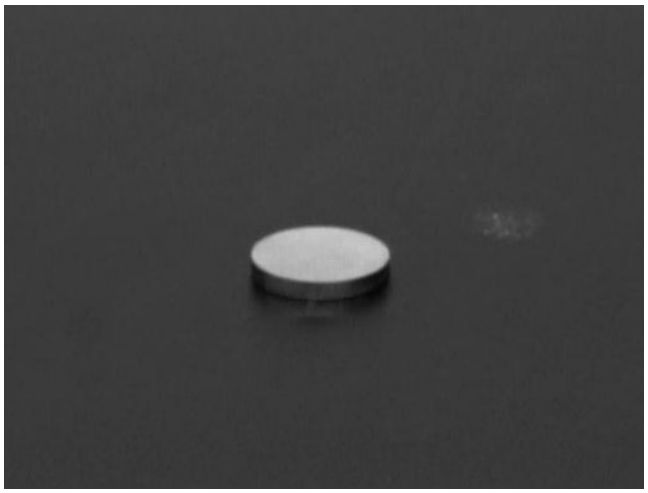

Figure 4.5 Nickel powder compact (12.1mm diameter, 1mm thick)

For the effect of green density studies, Ni 123 powder was compacted to various fractional green densities ($\rho_G$) 0.55 – 0.78 of theoretical density of nickel (8.9 kg/cm$^3$). For particle size analysis Ni 123, Ni 110, Ni 210 and Ni 210h powders were compacted to ~ 0.65 fractional green densities which were calculated using the density equation:

$$\rho_G = \frac{M}{V} \quad 4.1$$

Where M is the mass of the green compact, and V is the volume of the compact, measured using specimen dimensions which were measured at multiple points using a high precision micrometer.

## 4.2 CATS Setup

Experiments were conducted on stationary as well as moving tip configurations. Different set-ups were used for each configuration to accommodate the different experimental parameters such as tip size, pressure and tip mobility. A KEPCO DC power supply (100 A, 10 V capacity, Figure 4.6) was used for all experiments conducted with input currents less than or equal to 100A, while a DC power supply Power Ten P63- 51000 (1000A, 5V capacity, Figure 4.7) was used for all experiments that required higher currents.


Figure 4.6 KEPCO 100A, 10V power supply


Figure 4.7 Power Ten P63- 51000 1000A, 5V power supply

### *4.2.1 Stationary CATS Configuration*

Polished pure tungsten flat tips purchased from (Diamond ground Co.) were used in all stationary tip configurations with diameters 0.5 and 1 mm. Initially the tungsten tips were mounted on an Instron machine using an electrically insulated load application setup that was designed and manufactured specifically for CATS processes (Figure 4.8). The Instron machine is used to apply the load during CATS. However for later experiments another more dedicated CATS setup (Figure 4.9) using a modified micro-CNC was used. In this setup the specimen table was allowed to move in the X and Y direction, while the tip holder was mounted on a screw controlled z-motion to

enable pressure application. The tip holder was supplied with a spring bracket to maintain contact at all times during the process. The initial applied pressure was measured in terms of Z-axis screw rotations, using a balance placed underneath the tip where the first rotation of the screw corresponded to (4 N).

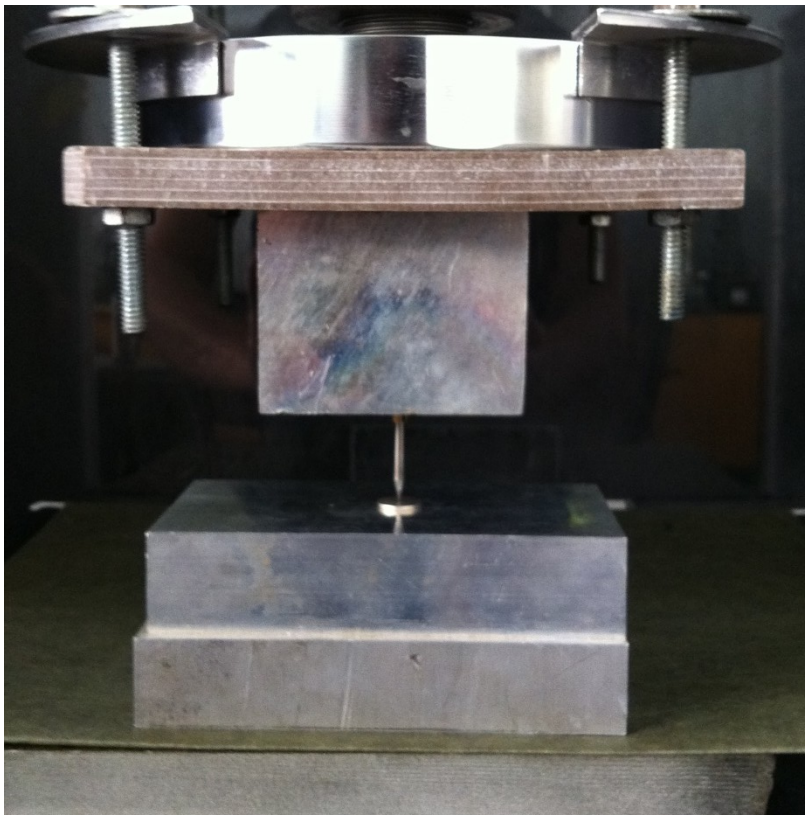

Figure 4.8 Stationary CATS setup on the Instron machine at the SDSU materials laboratory.

For both stationary tip configurations, the powder compacts are placed on a smooth surface of an aluminum block that is in turn connected to the DC power supply, the tip is then lowered until contact is achieved as close as possible to the center of the powder compact after which load is applied and maintained (Figure 4.10).

Figure 4.9 Dedicated CATS setup with XYZ motion capability

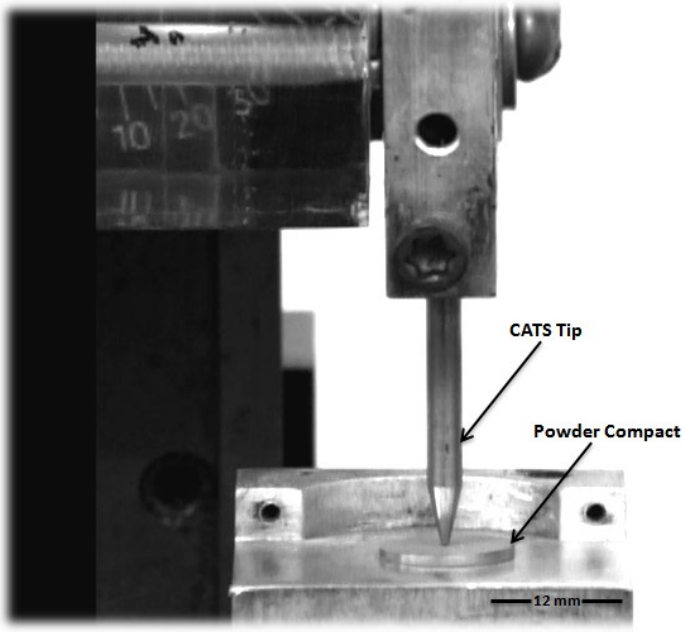


Figure 4.10 Close up photograph of the tip-specimen setup in stationary CATS

#### 4.2.1.1 Temperature Measurements in stationary CATS

Temperature measurements experiments were performed on the Instron stationary CATS setup. Initially unsheathed thermocouples were used where the thermocouple was placed at the closest point possible to the tip-powder compact interface as shown in Figure 4.11. However, this approach led to results that lacked repeatability and the thermocouples did not withstand high temperatures and often broke.

A special device was then designed that enabled temperature measurements at different radial locations on the top surface of the powder compact as seen in Figure 4.12. The base aluminum block had to be modified so that the tip positioning is central to ensure that all three thermocouples are properly spaced and to ensure positioning repeatability. After all thermocouples are in place, each thermocouple is separately tested using a multi-meter (Figure 4.13), one terminal is connected to the thermocouple extension wire and the other is connected to the powder compact to make sure that it is in contact with the surface of the specimen as the slightest of movements can break the contact between the specimen and thermocouples due to their light weight as well as the light weight of the holding device.

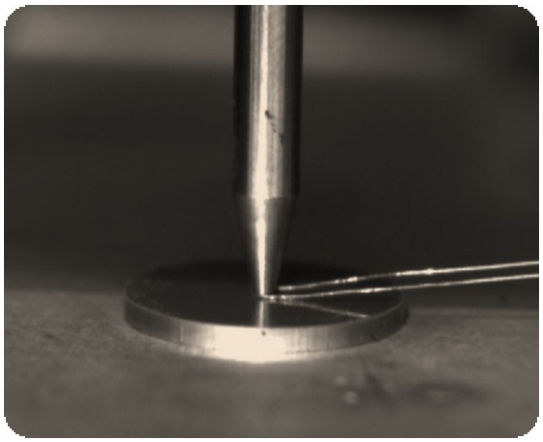

Figure 4.11 Bare-wire thermocouple placed right at the tip-compact interface

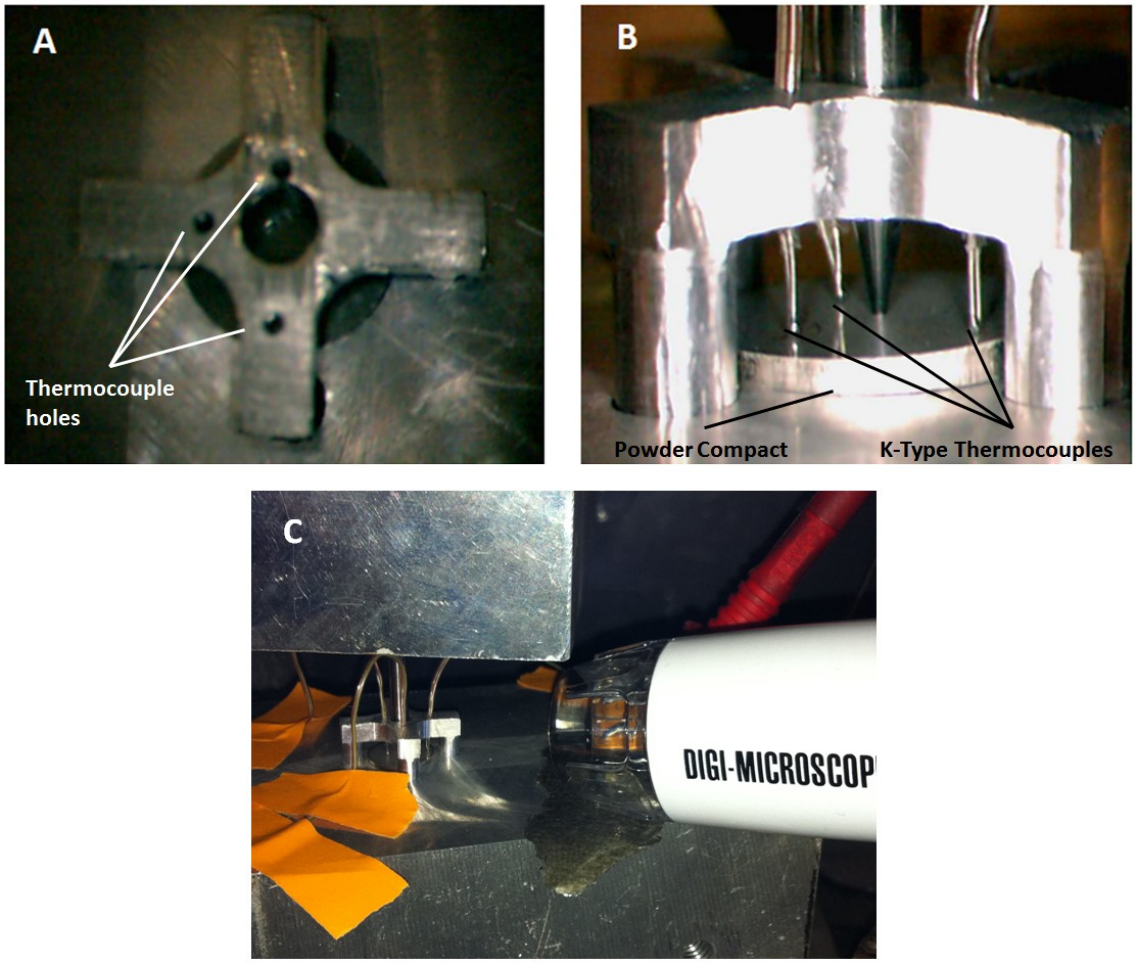


Figure 4.12 (a) Thermocouple holder with holes at different radial distances, (b) close-up photograph of tip-specimen-thermocouples configuration and (c) a photograph of the setup after all attachments are in place


Figure 4.13 Commercially available multi-meter used in the testing of thermocouple conductivity with the specimens

Other experiments were also conducted using flat tip K-type thermocouples cemented on the sintering tip at a ~2.5 mm distance from the tip-compact interface (Figure 4.14). The cement mixture used was 3 parts cement to 1 part water and was left to dry for 24 hours. After the thermocouple is cemented on the thermocouple it is also tested for electrical conductivity to make sure that that the cementing material did not insulate the thermocouple from the tip material (Figure 4.15).A data acquisition system (PDAQ view OMB-DAQ-55) was used to collect the temperature data from the thermocouples at a frequency of 3 readings per second (Figure 4.16). The data were then exported into excel and plotted versus time.

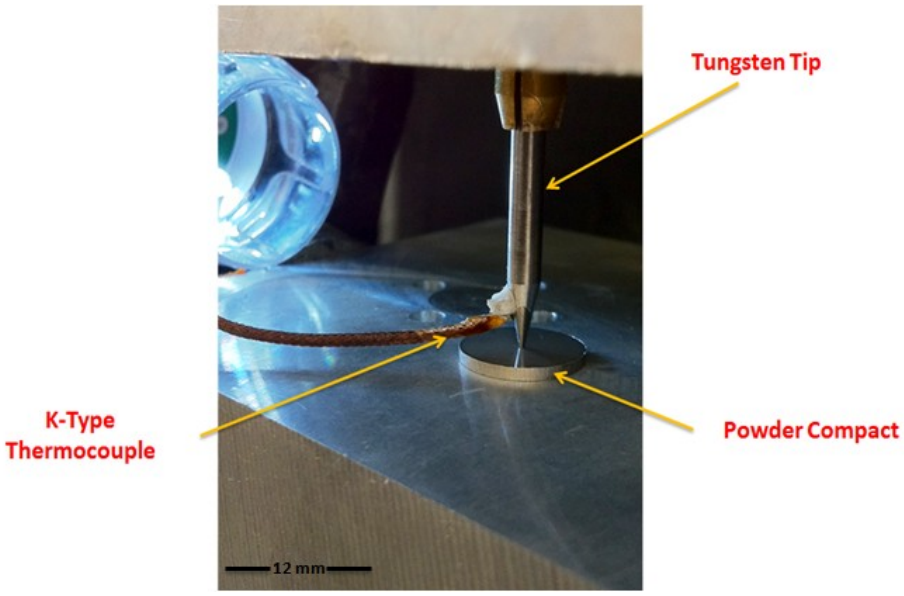


Figure 4.14 Flat-tip fast-response K-type thermocouple cemented on CATS tip

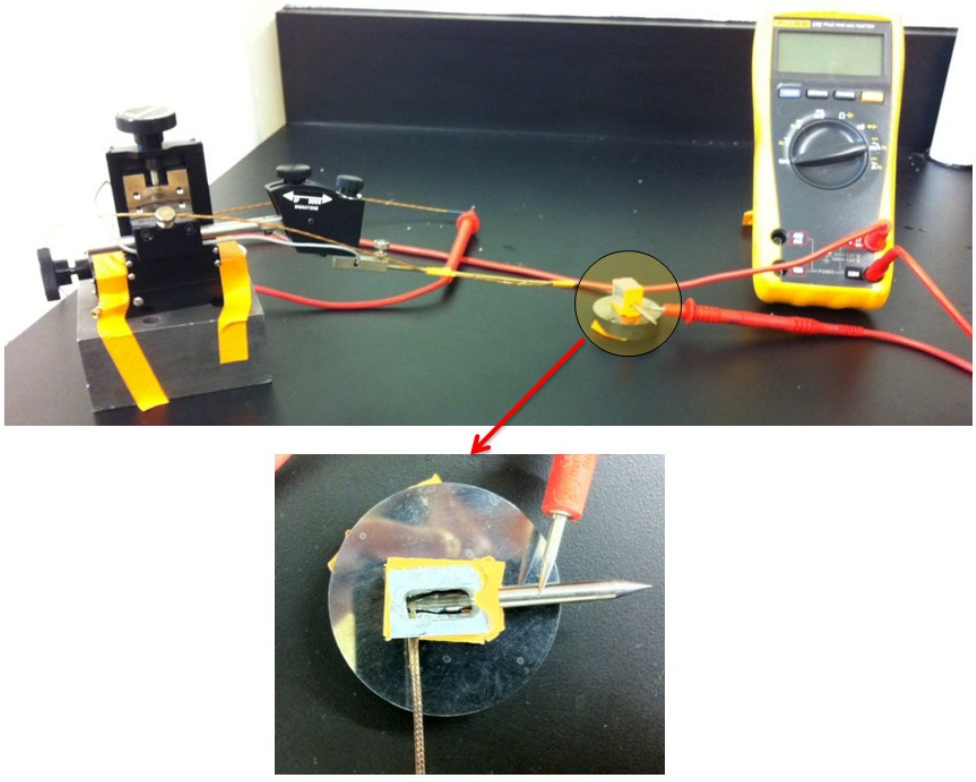

Figure 4.15 setup used to cement flat-tip thermocouples to CATS tips and testing for electrical conductivity


Figure 4.16 Omega OMB-DAQ-55 data acquisition system

4.2.1.2 Experiments on the Effect of Particle Size

Nickel powders type INCO123, INCO 110 and INCO 210h were compacted to ~63% green density and CATS was used according to the conditions listed in Table 4.2 Conditions used in the experiments on the effect of particle size in stationary CATS

Table 4.2 Conditions used in the experiments on the effect of particle size in stationary CATS

| Powder | Tip size (mm) | Nominal Current Density ($A/cm^2$) | Tip Pressure (MPa) | Sintering Time (sec) |
|---|---|---|---|---|
| INCO 210h | 1 | ~12,700 | 40 | 10 |
| | 0.5 | ~51,000 | | |
| INCO 123 | 1 | ~12,700 | | |
| | 0.5 | ~51,000 | | |
| INCO 110 | 1 | ~12,700 | | |

4.2.1.3 Production of μ-FGM using CATS

Nickel powders (INCO Type 123 and INCO 210) were used in the investigations. Powders were compacted to different fractional green densities between

~0.57- ~0.78 of theoretical. Fractional densities were calculated by measuring the specimen mass and dimensions to give the density, which was then divided by the theoretical density of nickel (8.9g/cm$^3$). Table 4.3 shows the investigated green density-particle size combinations.

Table 4.3 Investigated fractional green density-particle size combinations (for investigated configurations A-D) in μ-FGM production

| | **Fractional Green Density** | | |
|---|---|---|---|
| **Particle Size (μm)** | **0.57** | **0.67** | **0.78** |
| **3-7** | A | B | C |
| **0.5-1.0** | | D | |

All green compacts had the dimensions ~12.1 mm diameter and ~1 mm thickness (i.e. squat specimens) in order to minimize density distribution within the compact. Compacts of less than 0.57 fractional density lacked sufficient green strength for handling and processing and were therefore excluded from the investigations. For all specimens in this investigation a continuous current density of ~101 kA/cm$^2$ was to the top central region of each green compact using 0.5 mm tips for 30 seconds.

*4.2.2 Moving CATS*

A Novel μ-CATS device was designed and manufactured in the SDSU nano-engineering lab Fig 4.15. The μ-CATS is a sophisticated device that is equipped with a high precision X-Y stage and the tip fixture is equipped with a piezoelectric material to monitor the contact between the tip and powder bed as the tip is moving to ensure a

closed electric circuit at all times. μ-CATS is capable of sintering 2D features using tip sizes that can be down to 1 μm in diameter.

INCO 210 and copper powders (Nanodynamics Co.) were used in the moving CATS experiments. Micro tungsten tips (The Micromanipulator Co.) 7G-50 (radius of tip curvature) and 7G-10 (radius of tip curvature) were used as electrodes in the experiments (Figure 4.17). A servo motor MTR-10-E and a NAI MC-CQ-B motion controller (National Aperture) were used to control the linear movement of the specimen under the tip. The tip specimen and speed were dictated through a software MVP demo that uses G-code to precisely control the position and speed of the moving table. Table 4.4 summarizes the different parameters and conditions used in all the moving tip experiments.

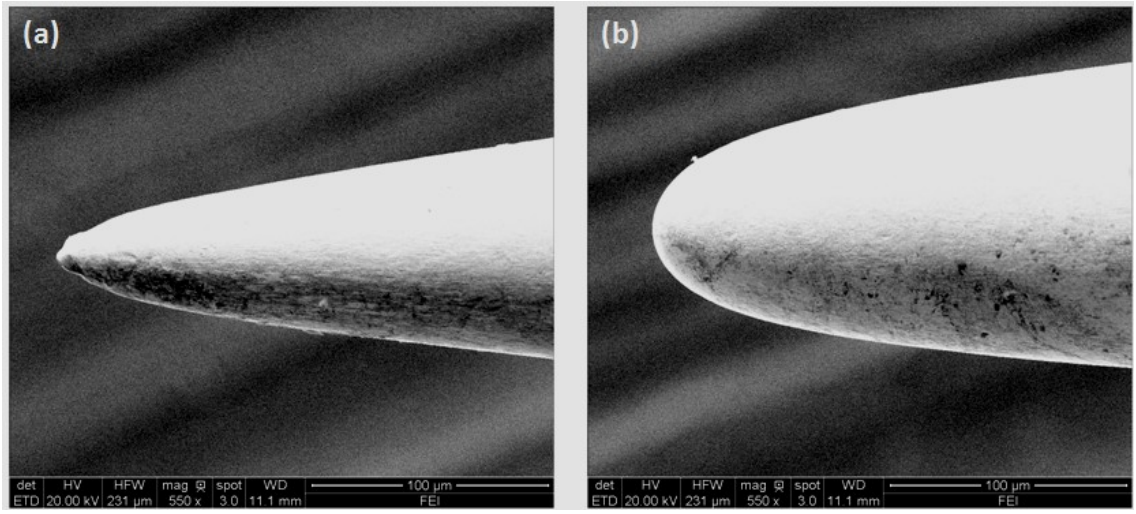


Figure 4.17 Micro-tungsten tips used in the moving-CATS experiments (a) 7G-10 and (b) 7G-50

Table 4.4 Summary of the conditions used in the moving-CATS experiments

| Experiment | Powders used | Tip type | Fractional density | Current (A) | Tip Speed (mm/s) |
|---|---|---|---|---|---|
| Effect of current intensity | Cu (500 nm) | 7G-10 | 75% | 0, 3, 6, 9 | 2.4 |
| | Cu (500 nm) | 7G-50 | 75% | 0, 12.9 | 2.4 |
| | Ni 210 | 7G-10 | 65% | 0, 6 | 0.2 |
| Effect of tip speed | Cu (500 nm) | 7G-10 | 75% | 6 | 0.2, 0.8 |
| | Ni 210 | 7G-10 | 65% | 6 | 0.2, 1.6 |
| Effect of particle size | Cu (>45μm), Cu (<45μm) | 7G-50 | 75% | 12.9 | 1.6 |
| Effect of green density | Cu (<45μm) | 7G-50 | 55%, 75% | 12.9 | 1.6 |

## 4.3 Post Sintering Processes

After being subjected to CATS processing, each specimen is placed in a 32mm diameter plastic mold (Figure 4.18). Figure 4.19 shows a schematic of the steps to mount the specimen in epoxy. First a mixture of 4 parts epoxy resin to 1 part hardener is placed in a disposable cup and is stirred gently for a few minutes until homogenous. It is important to avoid air bubbles as much as possible to avoid cracking problems during

machining later on in the specimen preparation. The mixture is then poured on top of the specimen in a plastic mold and is left to dry for 3-6 hours.

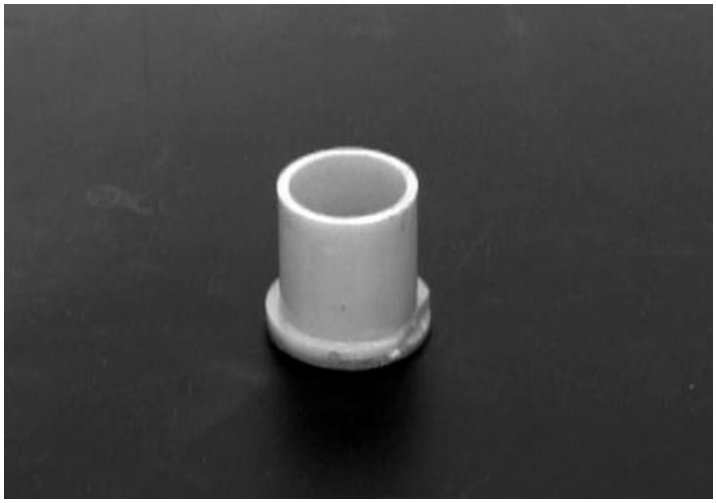

Figure 4.18 Plastic mold used for mounting specimens in epoxy

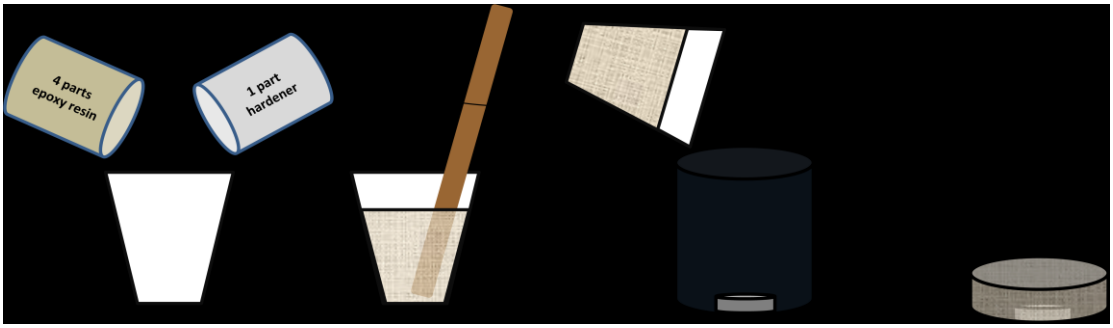


Figure 4.19 Schematic showing the steps to mount specimens in eopxy

Specimens that required surface analysis are then ground on four diffirent silicon carbide grinding papers: 240, 320, 400 and 1200 grit. After grinding, the specimens are cleaned in distilled water using a Branson 200 ultrasonic cleaner (Figure 4.20). For polishing, the specimens were mounted on LECO spectrum system 1000 (Figure 4.21) polishing machine and pneumatic pressure is applied to hold the samples against a rotating plate and a mono-crystalline liquid diamond suspension (South Bay

Technologies Inc) is frequently sprayed on the rotating polishing cloth. The specimens are polished on 1µm level for 15 minutes followed by 0.02 µm polishing for at least another 15 minutes or until a scratch-free mirror like surface is obtained. The Ni 210 specimens required prolonged polishing on the 1µm level with minimum applied pressure as prior grinding operations usually result in closed pore structures. Figure 4.22 shows an example of a polished specimen mounted in epoxy.

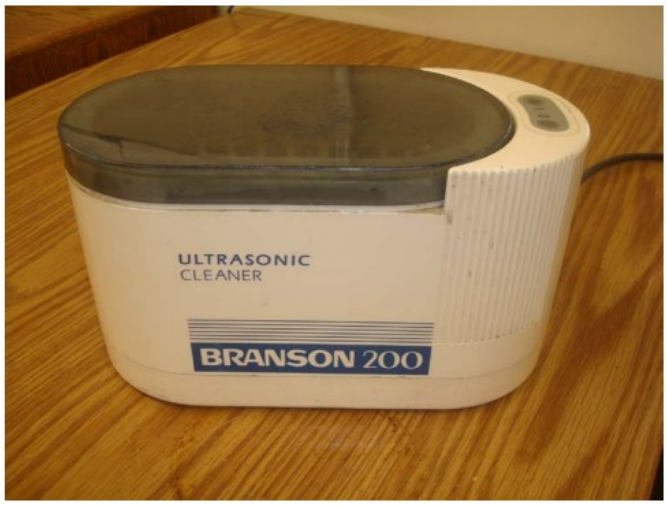


Figure 4.20 Branson 200 ultrasonic cleaner (courtesy of Preetam Borah)


Figure 4.21 Spectrum system 1000 polishing machine by LECO

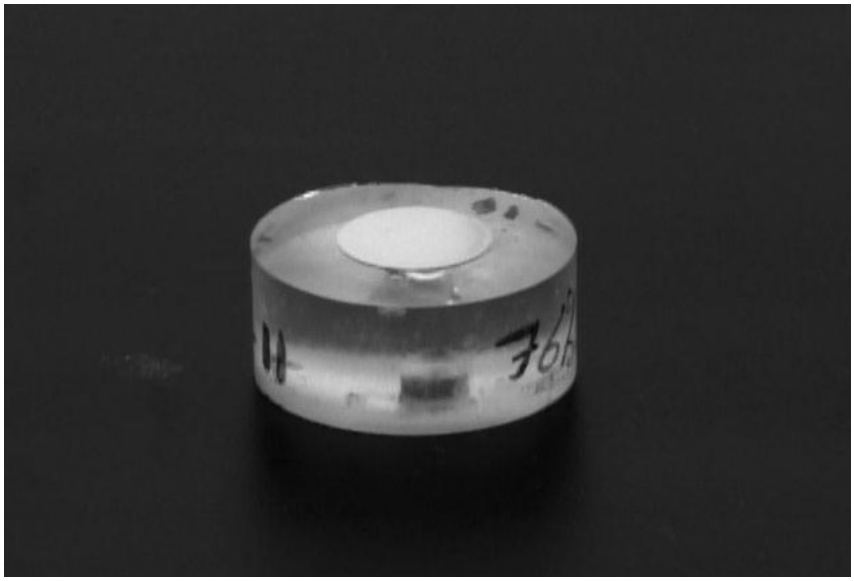

Figure 4.22 Photograph of a specimen molded into epoxy after grinding and polishing

Specimens that required sectioning were cut down the middle using a digital Buehler IsoMet 1000 diamond saw (Figure 4.23). Water is used as a coolant as higher temperatures caused by friction can cause sticking between the tool and the epoxy and may hinder the cutting process and even possibly damage the mounted specimen. For specimens that were sintered with a 0.5 mm tip, it was impossible to use the diamond saw to make a precise cut right down the center of the sintered region. To overcome this problem, the diamond saw is set to make a cut near the outer circumference of the sintered region, and the specimen is then ground using a 120 grit silicon carbide abrasive paper until the central line is reached (Figure 4.24). This is followed by the same grinding and polishing procedure mentioned previously. Figure 4.25 shows an example of a sectioned specimen after grinding and polishing.


Figure 4.23 BUEHLER diamond saw

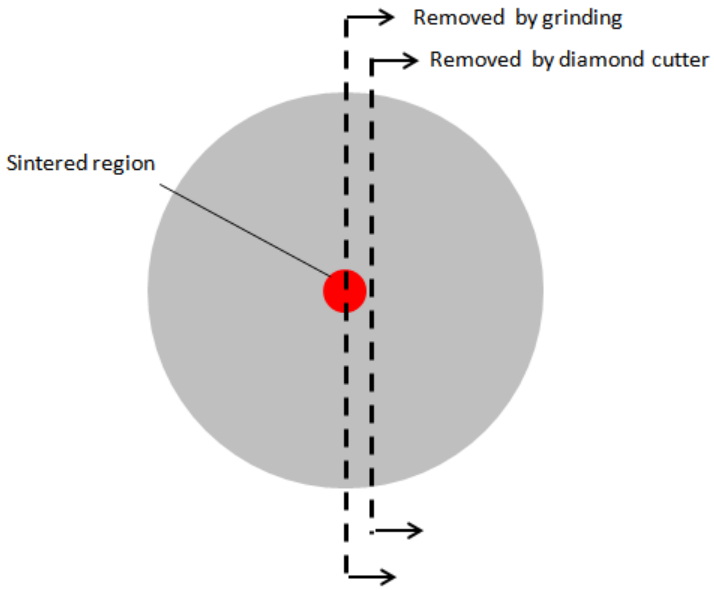


Figure 4.24 Schematic of a sintered region on a powder compact specifying the areas of the material removed by cutting and grinding.

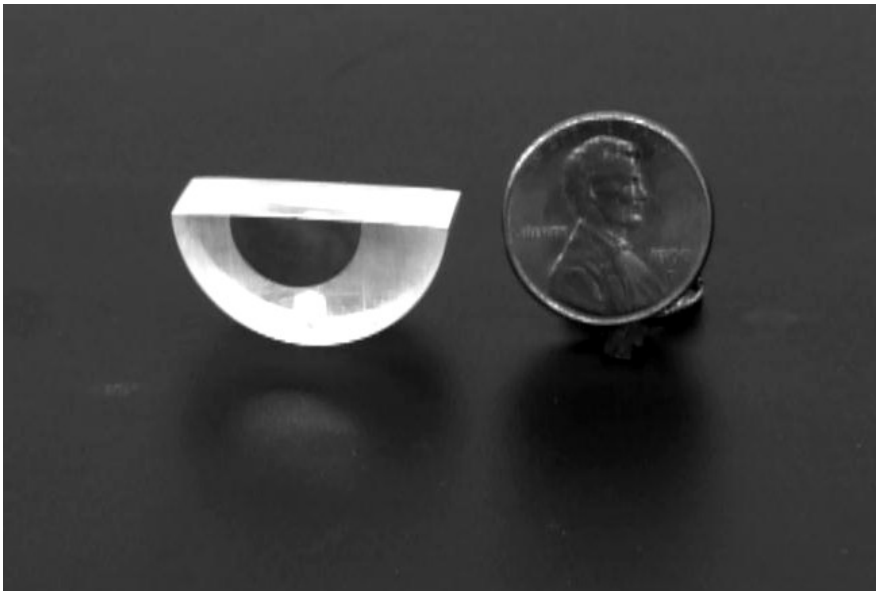

Figure 4.25 Photograph of a specimen molded in epoxy with sectioned at the center.

## 4.4 Materials Characterization

### *4.4.1 Scanning Electron Microscopy*

A field emission scanning electron microscope (FESEM QUANTA FEC-450) located in the SDSU EMF lab (Figure 4.26) is used to investigaate the morphology of the powders, green compacts and sintered specimens. A carbon double-sided tape is used to ensure an electrically conductive system between the tested specimens and the table inside the FESEM. For specimens embedded in epoxy, the carbon tape goes all the way round from the bottom of the assembly all the way to the top where the conducting specimen is located.

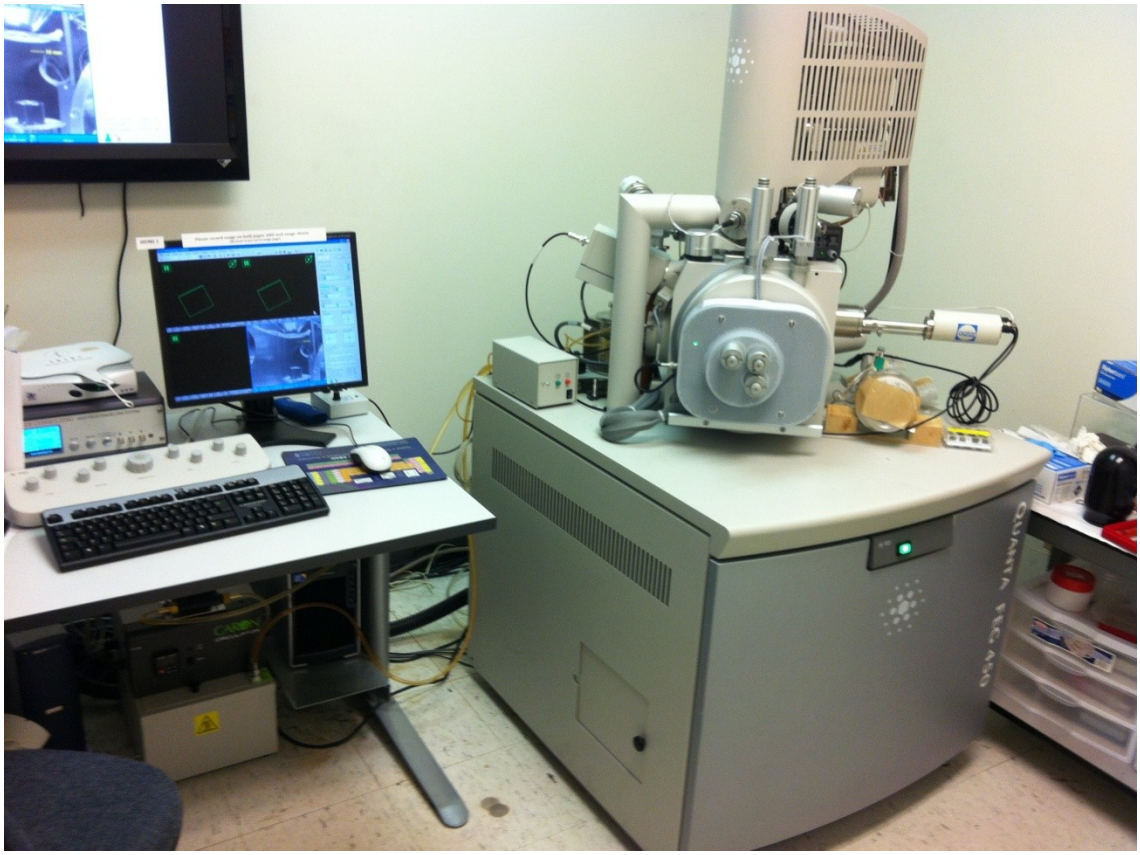

Figure 4.26 Scanning electron microscope at the EMF facility at SDSU

The step-by-step procedure to run the FESEM is as follows:

1. Vent specimen chamber and turn on Nitrogen flow.
2. When chamber is completely vented, turn on CCD camera and pull out the chamber door while monitoring the CCD camera display to make sure that no specimens or objects are in the way of the detector.
3. Use gloves to load specimens into the fixed specimen holder.
4. Close chamber door and again monitor the CCD display to make sure the specimen does not hit the detector on its way in
5. Bring the specimen to a 10mm distance from the detector

6. Open chamber door once again and capture a picture of the specimen at the 10mm distance from the detector using the NAV-CAM
7. Close chamber door and evacuate chamber under high vacuum pressure
8. Once specimen chamber is evacuated, the beam is turned on and the specimens are ready to be examined.

Loose powders are examined using a secondary electron detector for better imaging of the morphology of the powders. Powder compacts and sintered regions were usually tested under a back-scattered detector to facilitate image analysis by minimizing interference from objects in the subsurface that could be visible through larger pores.

### *4.4.2 Image Analysis*

Image analysis for full characterization of pore size and pore content was applied using open source software (UTHSCSA Image Tool version 3.0) developed by Department of Dental Diagnostic Science at The University of Texas Health Science Center, San Antonio, Texas. SEM images in .JPEG or .TIFF formats are first converted to 24 bitmap images and then imported into the software and colors are converted to grayscale. The image threshold (converting to pure black and white) is then controlled manually until all pores in the SEM image are blackened leaving the powders/solid material in white color. This step requires a lot of skill as the black and white images need to be compared to the originals making sure that the pores have similar sizes in both images. However, there is a learning curve in this process and with built up experience proper pores can be selected for comparison to reduce this process to one

step. Figure 4.27shows the corresponding black and white image after adjusting the threshold for an SEM image loaded in Image Tool.

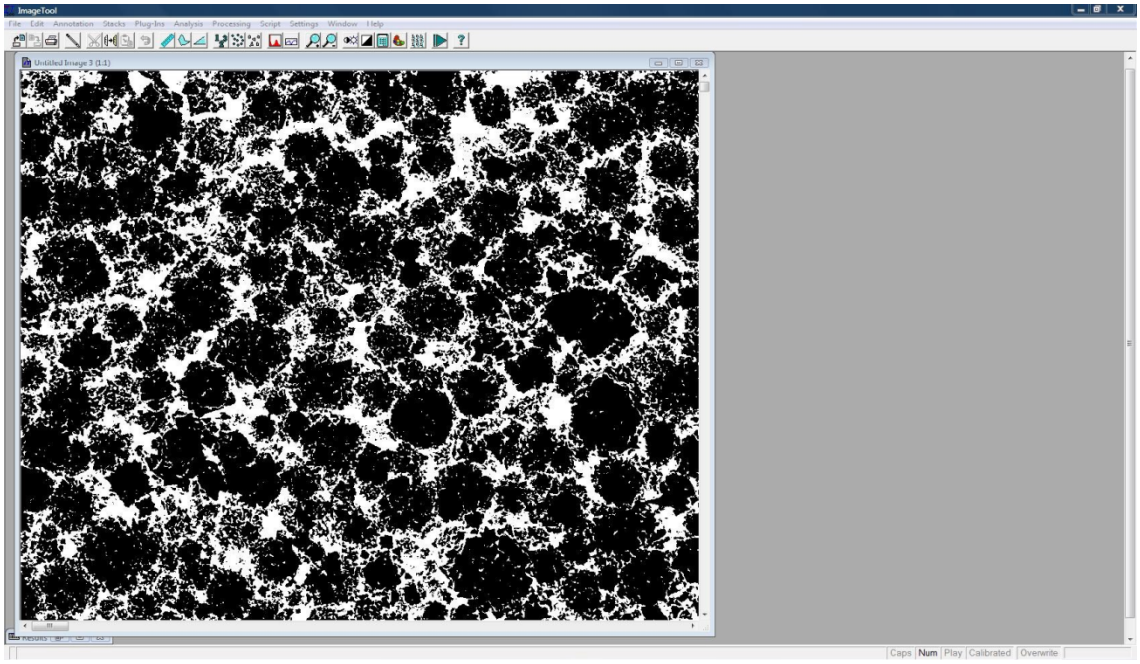

Figure 4.27 Screen capture of an image processed by ImageTool

For pore content analysis, a black and white count plug-in is used to calculate the percentage of the white and black colors. Pore size analysis required the use of an object-count plug-in to identify distinct objects in the black and white image (in this case closed pores), and then an object-analysis plug-in is used to analyze the size of the area of these objects/ pores. Equation 4.2 is then applied to calculate the equivalent spherical diameter of the pore $D_P$:

$$D_P = 2\sqrt{\frac{A}{\pi}} \qquad 4.2$$

Where A is the projected area of the pore.

### *4.4.3 Micro-Hardness Testing*

Micro-hardness measurements were performed on a Wilson Instruments digital micro-hardness tester (Figure 4.28) with the minimum possible applied load (10g) to limit the indentations size. The hardness tester comes with a flatness adjustment table to hold the specimens in a flat position. Once the specimens are secured, the height of the table is adjusted to achieve the best focus under a (40x10) X microscope lens and the specimen is ready for testing. The load is then applied through a diamond indenter and the same microscope lens is once again used to measure the 2 diagonals of the diamond shaped indent on the specimen. The Hardness value in (HV) is then calculated using the built in equation:

$$HV = 1.854\frac{F(Kgf)}{(D_{Avg})^2} \qquad 4.3$$

Where $D_{Avg}$ is the average of the 2 diagonals of the indent.

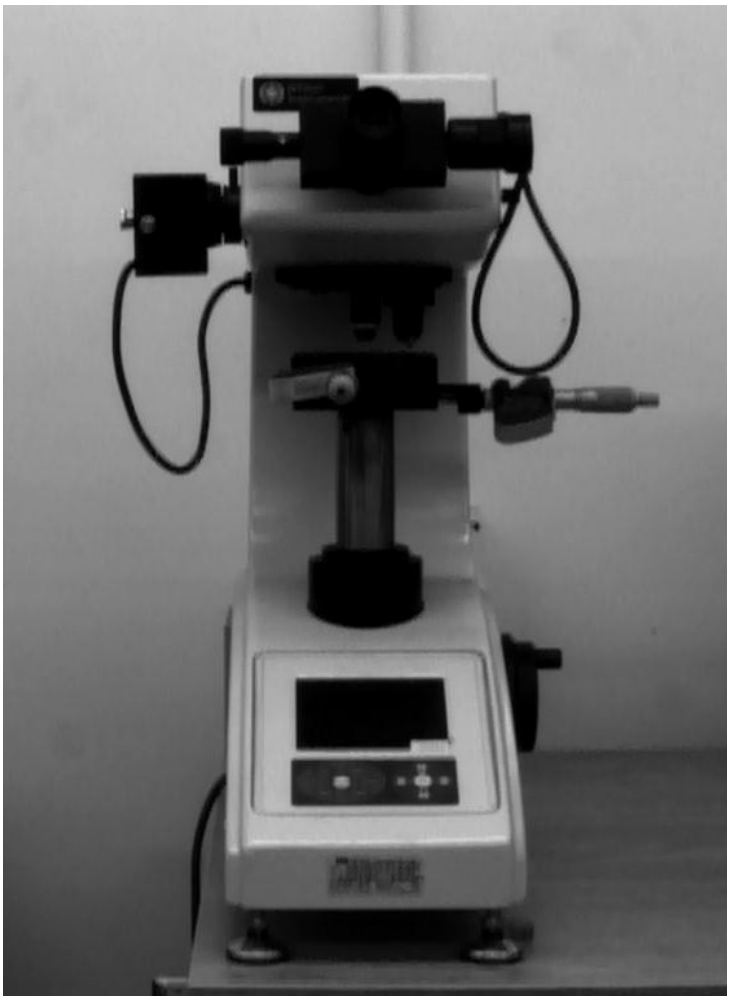

Figure 4.28 Micro-hardness tester at AMPL

# 5 RESULTS AND DISCUSSION

Results from all experiments on stationary and moving CATS and characterization procedures described in Chapter 3 are discussed in this chapter.

## 5.1 Temperature Measurements in Stationary CATS

As discussed earlier, different techniques and various thermocouple types were used to measure the temperature distribution in the CATS setup. One of the early attempts was to use a bare-wire thermocouple with direct contact at the tip-specimen interface. The temperature-time profile generated for nickel powders with different particle sizes under a 12,000 A/cm$^2$ current density is shown in Figure 5.1. It is clear that significantly higher temperatures are generated as the particle size is decreased (all compacts were of the same initial green density). According to Lefebvre *et al* [102] particle interfaces act as resistors to current flow, he also proposed a circuit shown in Figure 5.2 which suggests that powder compacts with smaller particle size will have an overall increased resistivity due to the increase in the number of contact points within the compact, such effect will also be intensified in case of the presence of oxide surface layers on the powders. This increased resistivity can be responsible for the increased temperature observed in smaller particle sizes.

Although our initial results were promising in the sense of monitoring the effect of particle size on the temperature distribution, however the repeatability in temperature measurements could be improved upon. Limitations of this technique include limited

control over the accurate positioning of the thermocouple in relation to the tip and the low strength of the thermocouples, which can result in thermocouple breakage upon application of tension. Consequently, the technique, although promising, was replaced with a more reliable approach, as discussed below.

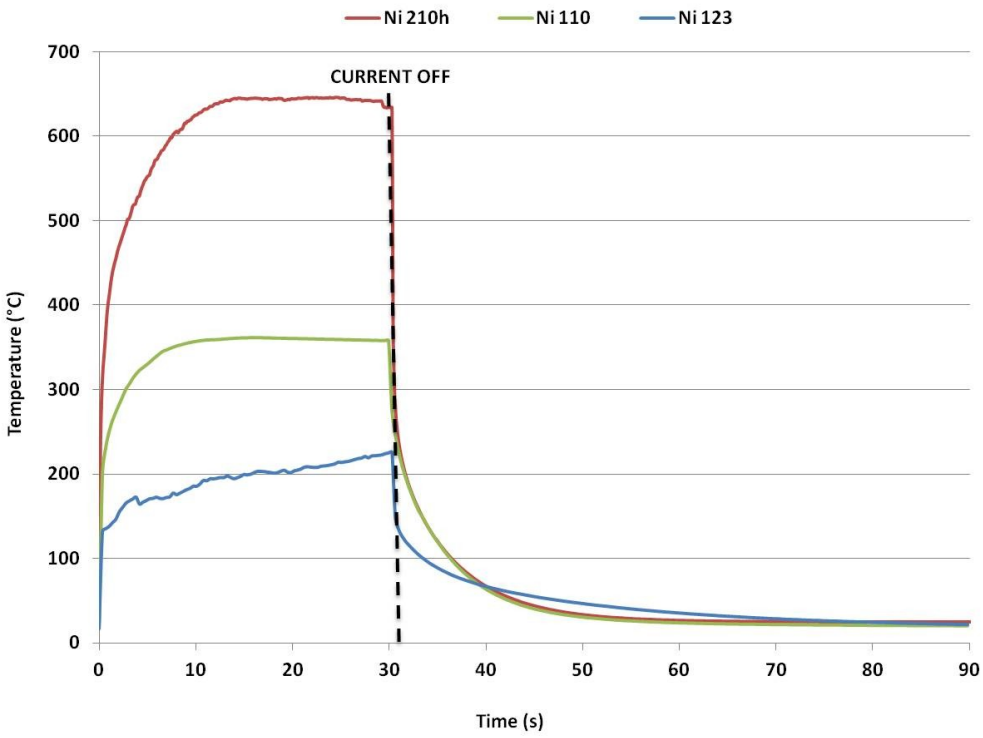


Figure 5.1 Temperature profiles in CATS of nickel powder compacts with different initial particle size

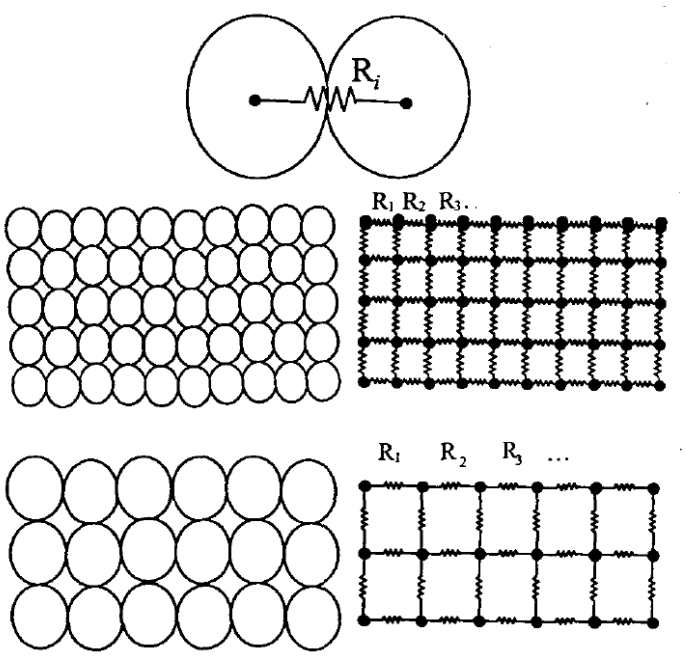


Figure 5.2 Effect of particle size on the electrical resistivity of green compacts [102]

Figure 5.3 shows temperature profiles for Ni 123 powder compacts with average green densities ~55%, 67% and 76% of theoretical at an applied nominal current density ~50,000A/cm$^2$. The temperatures were taken by using the thermocouple configuration shown in Figure 4.14. For all samples the initial heating rate was found to be the same, however, higher temperatures were observed with a decrease in green densities. It appears that steady state temperatures were reached for the 67% and 76% density specimens within the duration of sintering. This was not however the case for the lowest density where a continuously increasing temperature was observed. This could be explained if we consider the development of a highly consolidated progressive region under the tip. This in turn will act as a highly conducting medium, transferring sintering conditions to the significantly unsintered (more resistive) areas beneath it. This will

consequently be repeated as sintering progresses through the thickness of the powder compact.

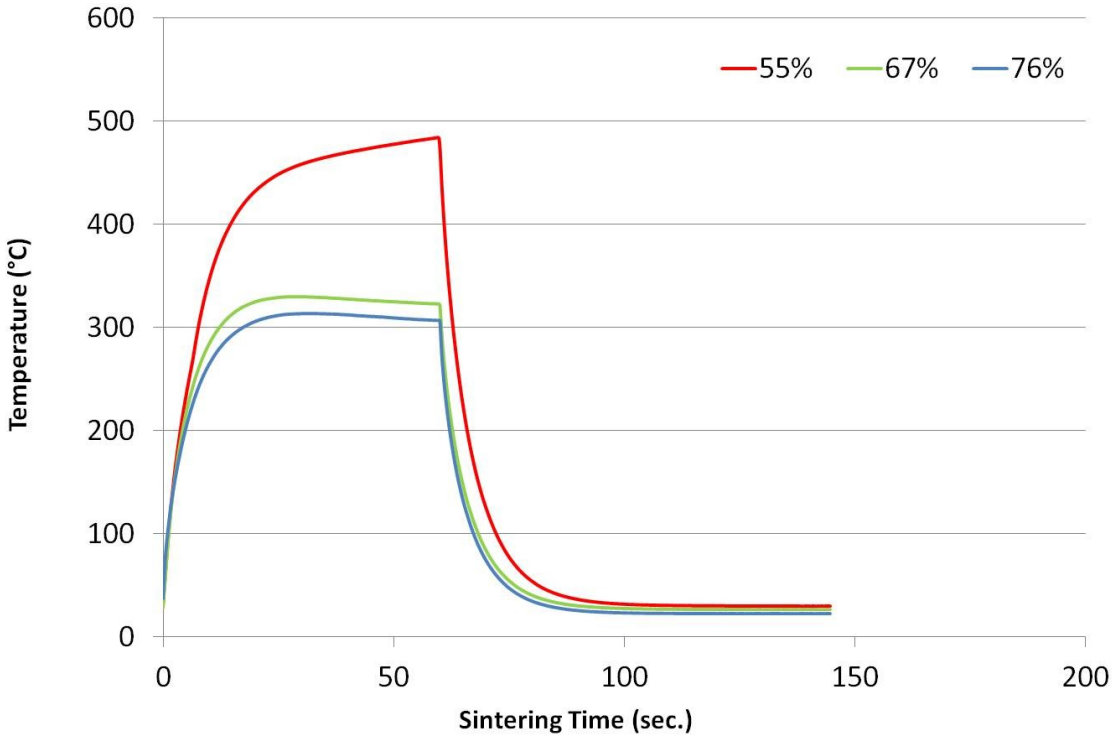


Figure 5.3 Temperature measurements taken from a thermocouple cemented on the CATS tip (~2.5 mm away from tip-powder compact interface)

For the same set of initial green densities, temperature measurements were also taken on the powder compact surface at different radial distances from the tip interface. For all investigated green densities, the temperature was found to decline radially away from the tip location. Figure 5.4-a shows temperature profiles taken from the closest thermocouple to the tip (~2.5 mm away from the tip circumference). It shows that the maximum temperature was experienced by the lowest density specimens as more heat generation is expected in the vicinity of the tip, while the 76% density specimen achieved a steady-state temperature higher than that of the 67% density, which was also

the case for the temperature profiles taken from the thermocouple that is farthest from the tip (Figure 5.4-b). However, at this location the 55% density specimen achieved the minimum temperature. This is due to the expected higher thermal conductivity of the 76% density compact compared to lower density specimens. The results also show that the maximum temperature achieved was ~140 °C at a distance ~ 2.5 mm from the tip circumference. At such temperatures nickel is not expected to sinter which therefore favors a localized sintering effect only closer to the tip.

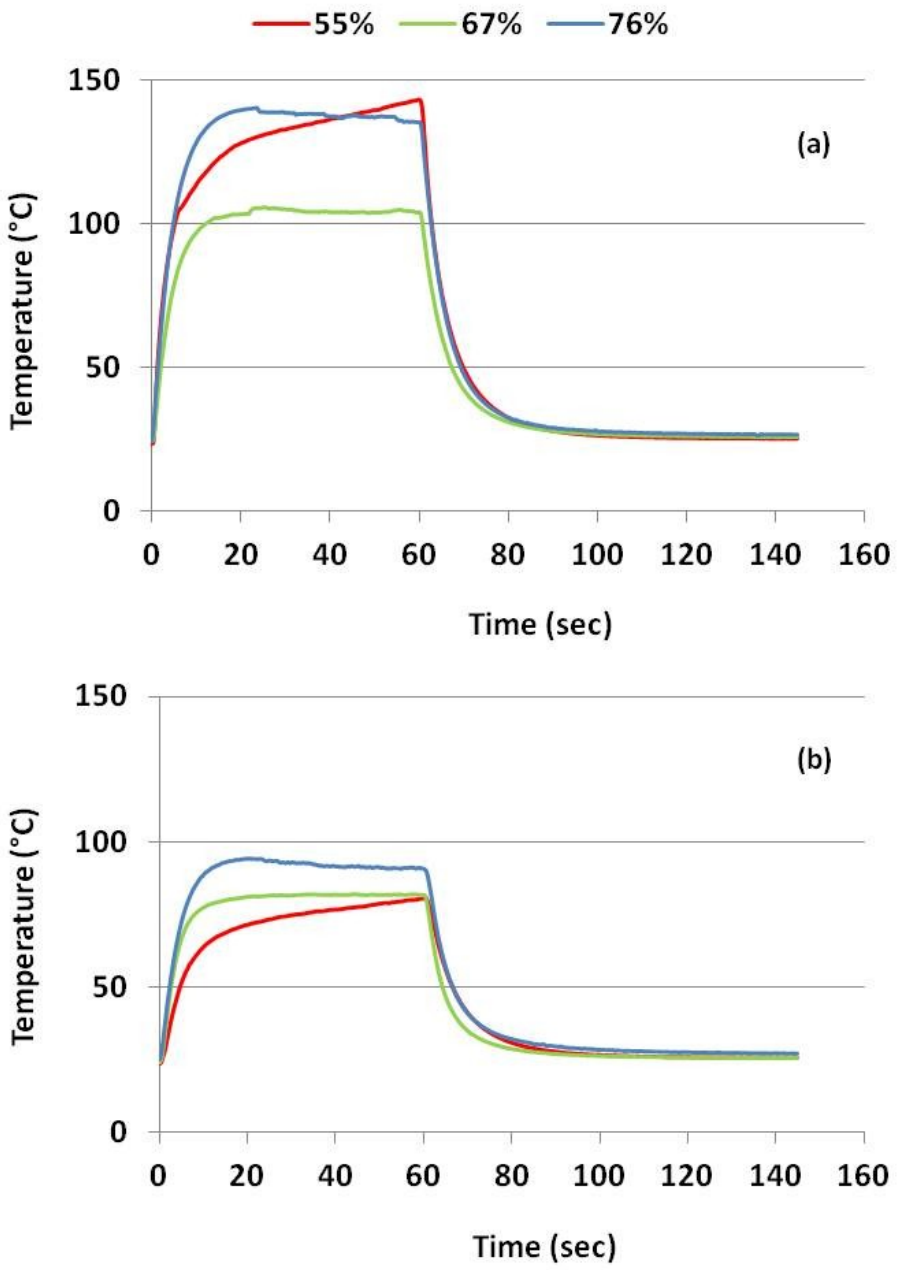


Figure 5.4 Surface temperature profiles for nickel powder compacts with various initial green densities sintered with CATS (a) at a distance ~2.5 mm from the tip circumference and (b) close to the edge of the green compact

Figure 5.5 shows scanning electron micrographs of the local sintered region under and in the vicinity of the tip for the 55% initial green density specimens. Some surface circumferential cracks were observed around the sintered regions due to

shrinkage and thermally induced stresses. However, it was observed that the radius as well as the thickness of these cracks decreased for the 67% density specimen as less shrinkage was experienced while for the 76% density specimens (with an expected higher green strength), minimum shrinkage was observed and no circumferential cracks were found. Further microscopic analysis shows that consolidation was mainly confined to the region immediately beneath the tip, and no consolidation took place at the areas in between this region and the circumferential crack, and the observed structure was similar to that of the unsintered green compact which is evidence of localized sintering.

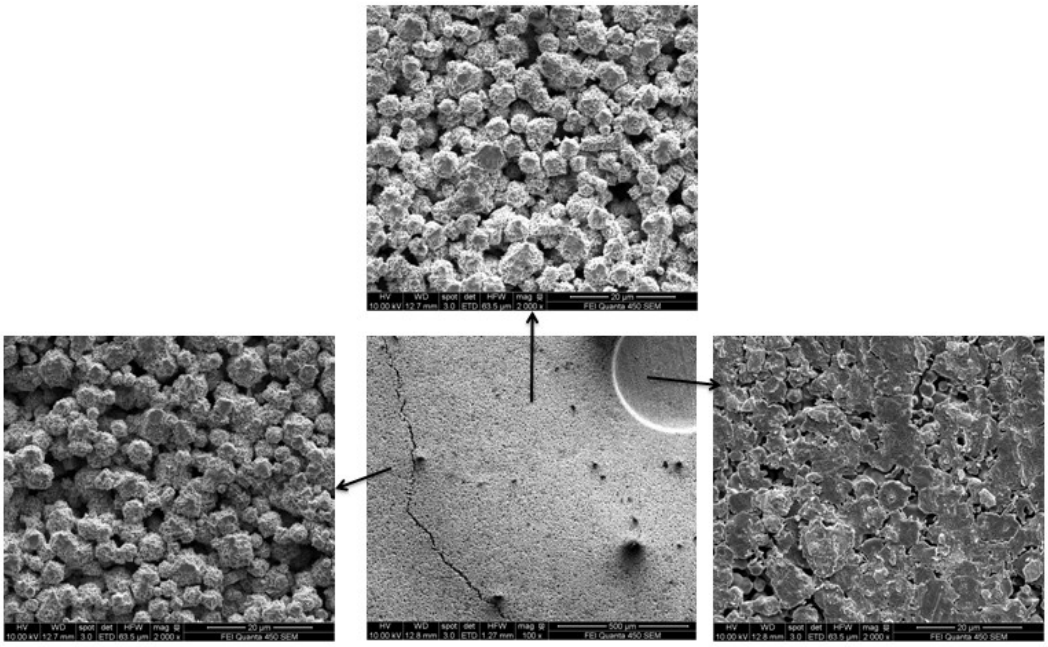

Figure 5.5 Scanning electron micrograph of a 55% initial green density specimen showing evident densification only at the area underneath the tip.

Figure 5.6 shows scanning electron micrographs taken at ~150μm beneath the surface of varying initial green density powder compacts (a,b,c) and the corresponding surfaces after exposure to direct electric current for 60 seconds (d,e,f). Despite having

the lowest initial green density, the 55% dense specimens observed the most significant and pronounced shrinkage amongst all the specimens processed. The assumed nominal current density (the applied current / the tip-material contact area) is in fact magnified as the actual contact area in powder compacts is less than the assumed area due to the presence of porosity. In pressure-assisted powder densification, an effective pressure [103] is defined to take into account the true contact area between the punch and the material. For example, a fully consolidated material should result in an effective pressure equal to the applied pressure; however, a porous compact should result in a considerably higher effective pressure, due to a decline in the effective contacting area exposed to the same load. Although not previously reported to the best of the author's knowledge, it becomes also logical in the case of electric current activated sintering, to introduce an "effective current density" term $J_E$ , analogous to the effective pressure, which should increase with a decrease in the initial green density. As such the following equation, can be introduced maybe assumed to represent effective current density $J_E$.

$$\frac{J_E}{J_N} = \left(\frac{1}{1-\theta^{\frac{2}{3}}}\right) \tag{5.1}$$

Where, $J_N$ is the nominal current density and $\theta$ is the fractional porosity.

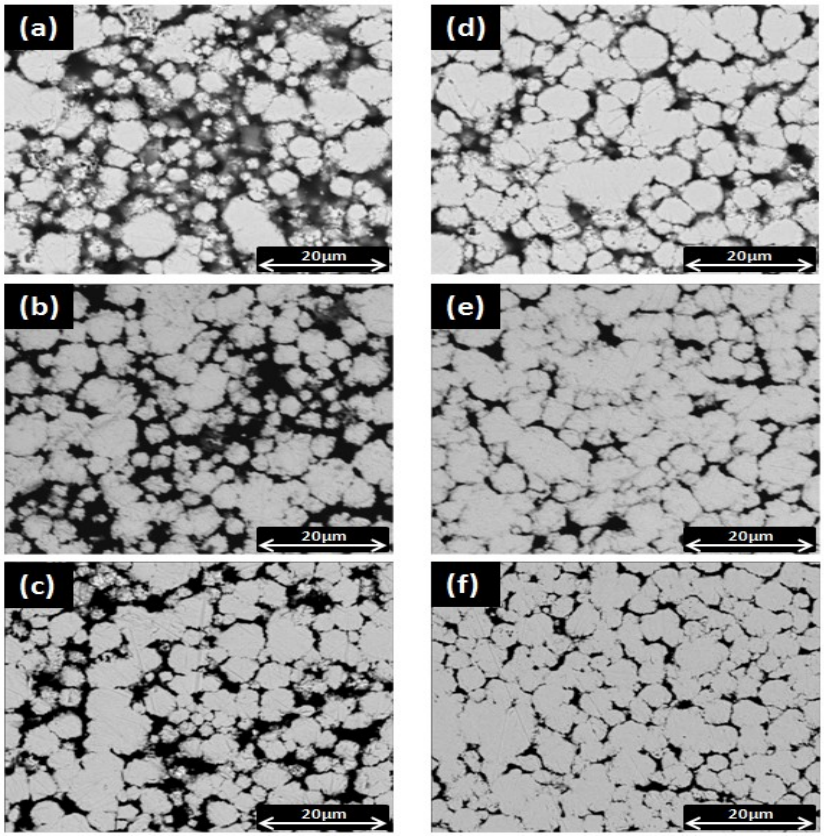


Figure 5.6 Scanning electron micrographs of unsintered top surface compacts of varying initial green densities 76%, 67%, 55% (a,b,c) respectively and corresponding surfaces exposed to 60 seconds of current activated sintering at a nominal current density of 50,000 A/cm$^2$ (d,e,f)

Furthermore, it is well known that the thermal conductivity of powder compacts decreases with the decrease in green density due to the minimal particle-particle contact and interfacial areas. This allows most of the heat generated to remain in the process zone underneath the tip rather than dissipate to the remainder of the compact, giving rise to increased local temperature. Although all green density specimens were exposed to the same nominal current density, the initial effective current density is expected to be higher for the lower density specimens (Figure 5.7). All the above factors have contributed to the enhanced sintering behavior of the lowest density specimens

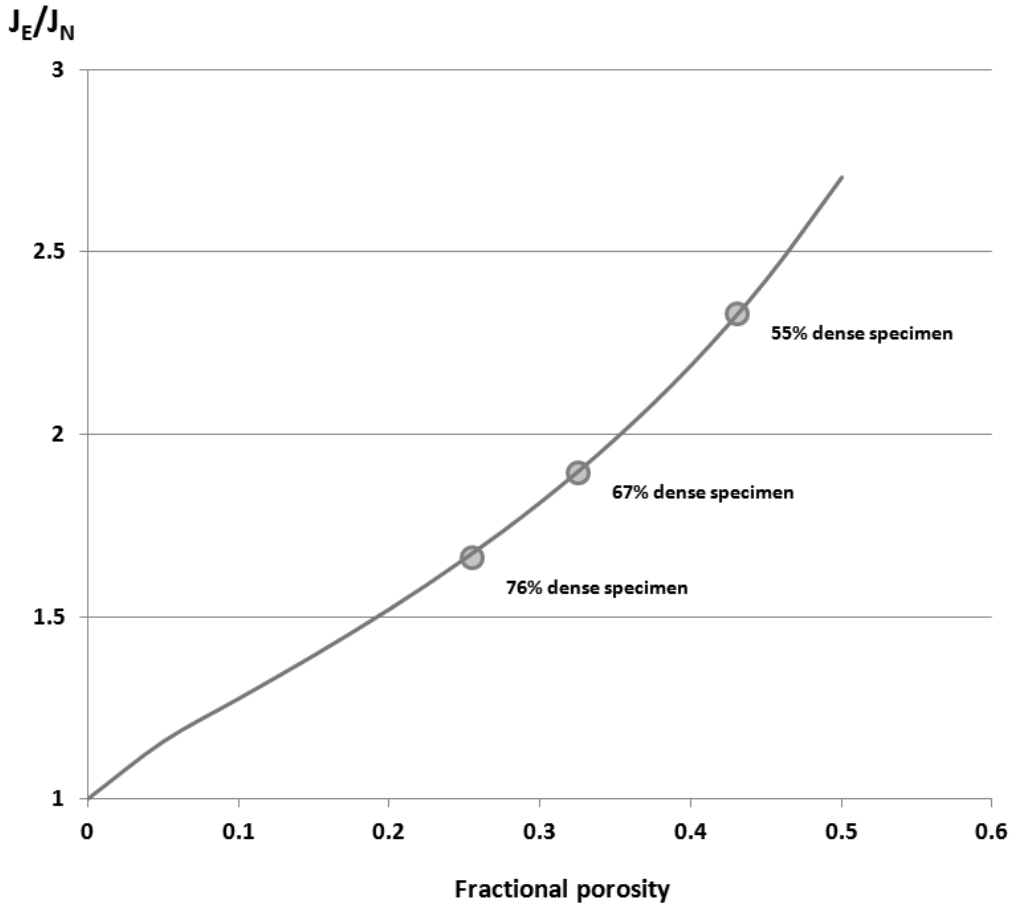


Figure 5.7 Effective current density at various fractional porosities

Figure 5.8 shows the image analysis of the pore content at 150 μm beneath the surface for all sintered specimens and it shows that all three initial green densities reached a final density of ~ 0.85 of theoretical. However when the densification parameter (Ψ) is considered it is clear that it is inversely proportional with the initial green density, which is expected due to all the factors mentioned above that contributed to the enhanced sintering behavior for lower green densities.

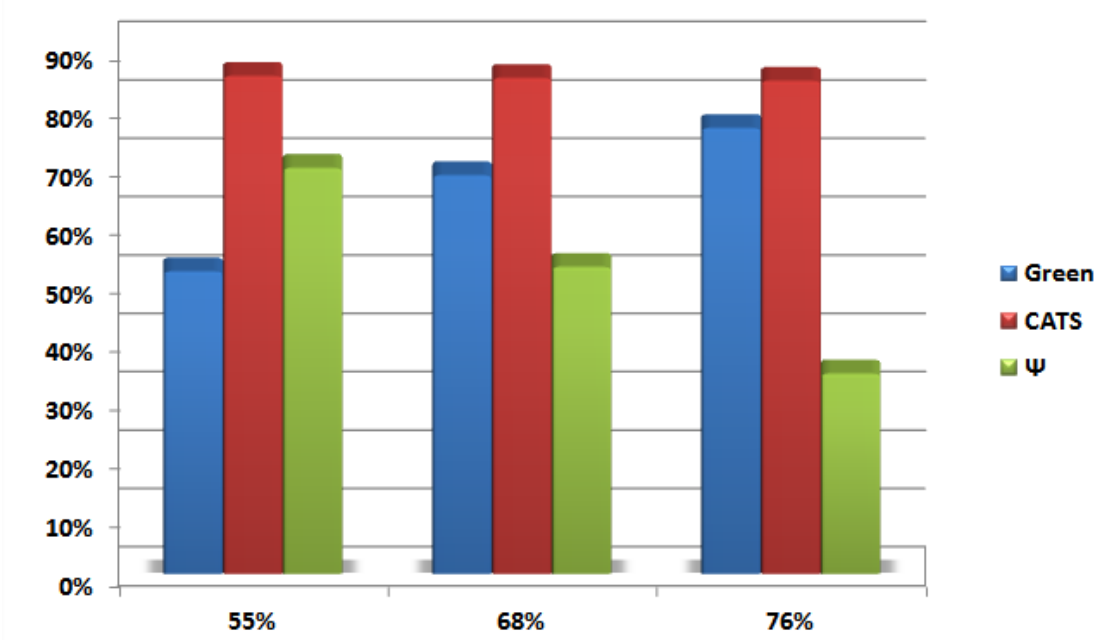


Figure 5.8 Pore content and densification parameter Ψ for all investigated green densities

## 5.2 Finite Element Modeling

COMSOL Multiphysics v3.5a was used in all finite element modeling efforts. Initially the SPS model developed by Anselmi-Tamburini *et al* [63] was reconstructed to test the possibility of thermo-electric coupling in a popular SPS problem by using COMSOL Multiphysics. The original model obtained temperature and current distributions by solving equation 2.3.

Figure 5.9 shows the model that was built in COMSOL with the similar geometries of punches, die and specimen to those used in the original model. The original model used temperature dependent variables for electrical and thermal conductivities of all the used materials. However, for simplicity, fixed values were used in our models (Table 5.1).

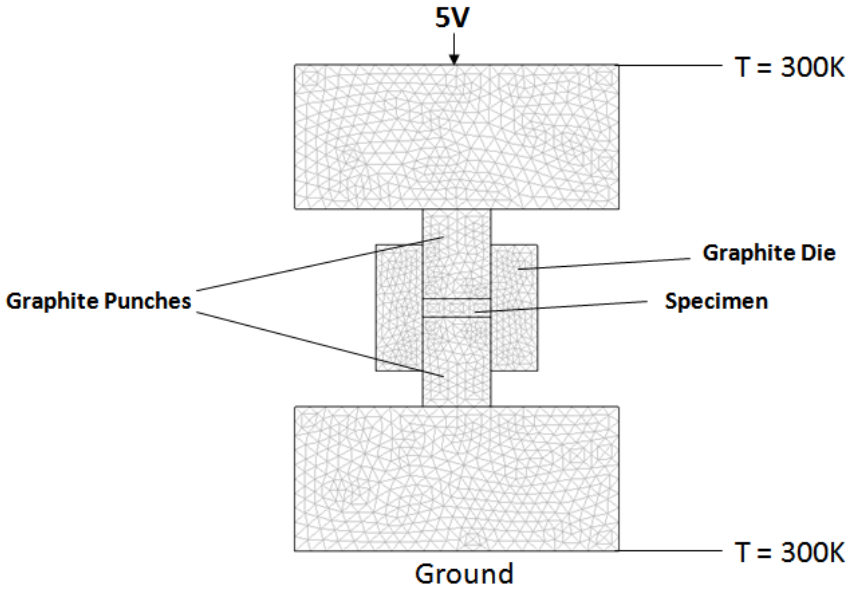


Figure 5.9 A simplified SPS apparatus geometry built in COMSOL with similar dimensions to the model built by Anselmi-Tamburini *et al* [63]

Figure 5.10 andFigure 5.11 show the current density distributions in Cu and alumina samples respectively for both models. Similar current distributions can be seen throughout the SPS system in both models. Even though the current density is highest in the graphite punches regardless of the material of the specimen used, it can be seen that for the highly conductive copper specimen, a significant portion of the current flows through the material which was not the case for the insulating alumina specimen.

Table 5.1 Material properties used in modelling

| | Graphite | Copper | Alumina |
|---|---|---|---|
| Thermal Conductivity K (W/m.K) | 470 | 401 | 27 |
| Electrical Conductivity σ (S/m) | 1.3 E5 | 58 E6 | 4 E-7 |

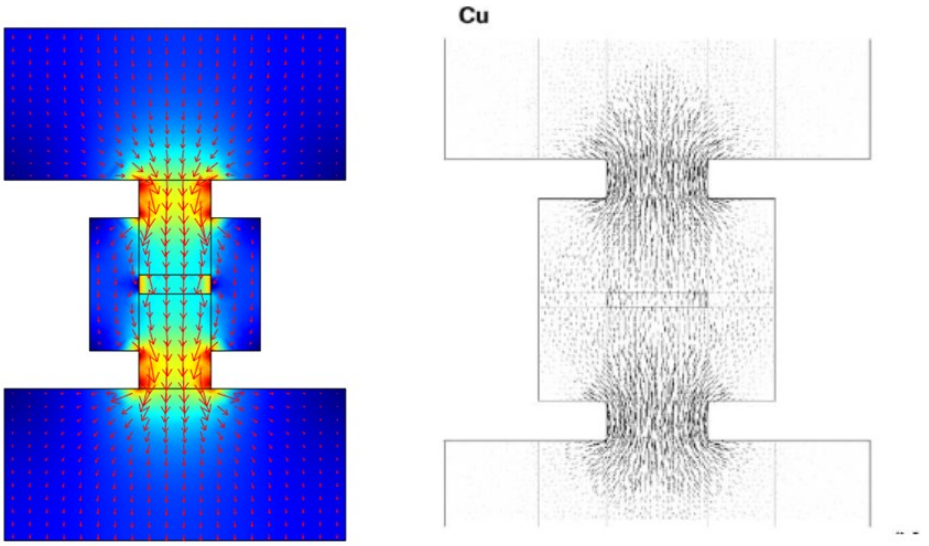


Figure 5.10 Current distribution in the COMSOL model (Left) and the model built by Anselmi-Tamburini *et al* [63] (right) for SPS of copper specimens

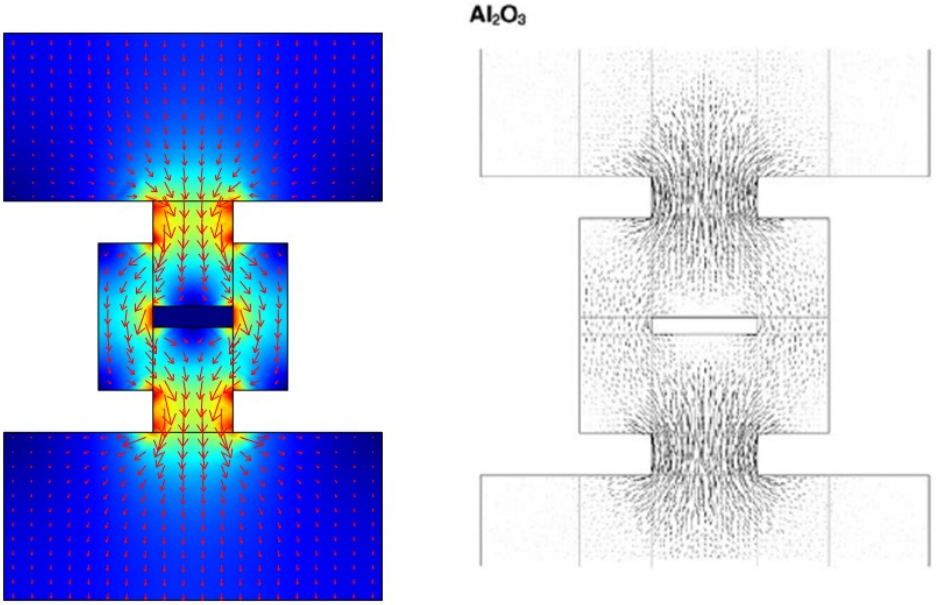


Figure 5.11 Current distribution in the COMSOL model (Left) and the model built by Anselmi-Tamburini *et al* [63] (right) for SPS of alumina specimens

Figure 5.12 shows the temperature distribution in the SPS system of an alumina specimen after 9 seconds of current exposure. The maximum temperature obtained by the COMSOL model was 570 °C which is acceptably comparable to the 640 °C temperature obtained from the original model. These results prove that COMSOL is suitable for the electro-thermal problem of modeling the current and temperature distributions in SPS.

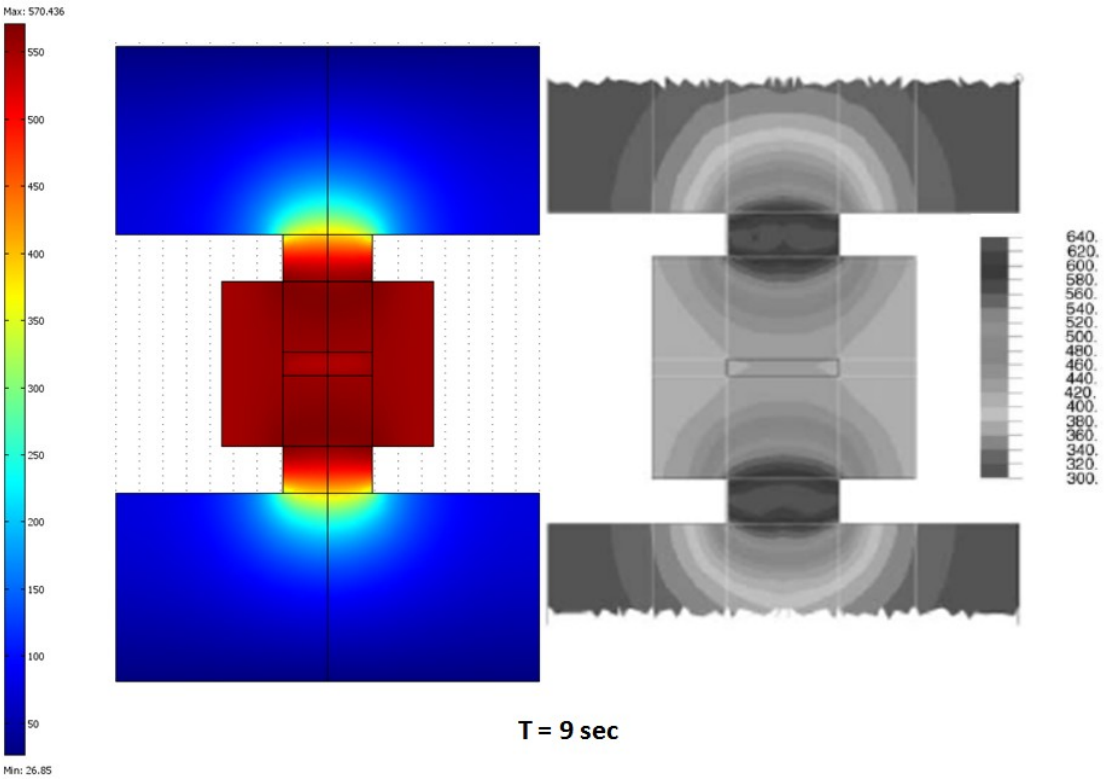


Figure 5.12 temperature distribution after 9 sec of DC current exposure in SPS of an alumina specimen. COMSOL (Left) and Anselmi-Tamburini *et al* [63] (right)

A COMSOL model was then developed to model the current and temperature distribution in CATS using similar boundary conditions and approximations as in the SPS problem. A constant voltage of 5V was applied through the entire CATS assembly

(Figure 5.13) and a heat transfer coefficient ($h$ = 10 W/ m$^2$.K) was assumed throughout the entire CATS setup. Unlike SPS the only source of Joule heating is the current passing through the specimen which complicates the problem as the use of material properties of fully dense materials becomes infeasible (not enough resistive heating). Therefore an electrical conductivity of (2750 S/m) had to be considered which is significantly lower than the theoretical conductivity of nickel.

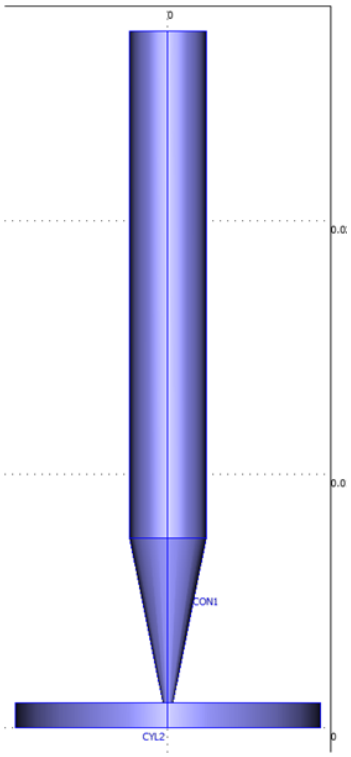


Figure 5.13 Schematic of the CATS setup used in the finite element model

Figure 5.14 shows that a maximum steady state temperature of 982 °C was generated right underneath the tip taking a hemispherical shape. A temperature decline is also observed with increased distance away from this zone. It can be seen that the

temperature in the tip drops to about 450 °C at a distance of ~ 2.5 mm (location of the cemented thermocouple in temperature measurement experiments) which is also in agreement with experimental results.

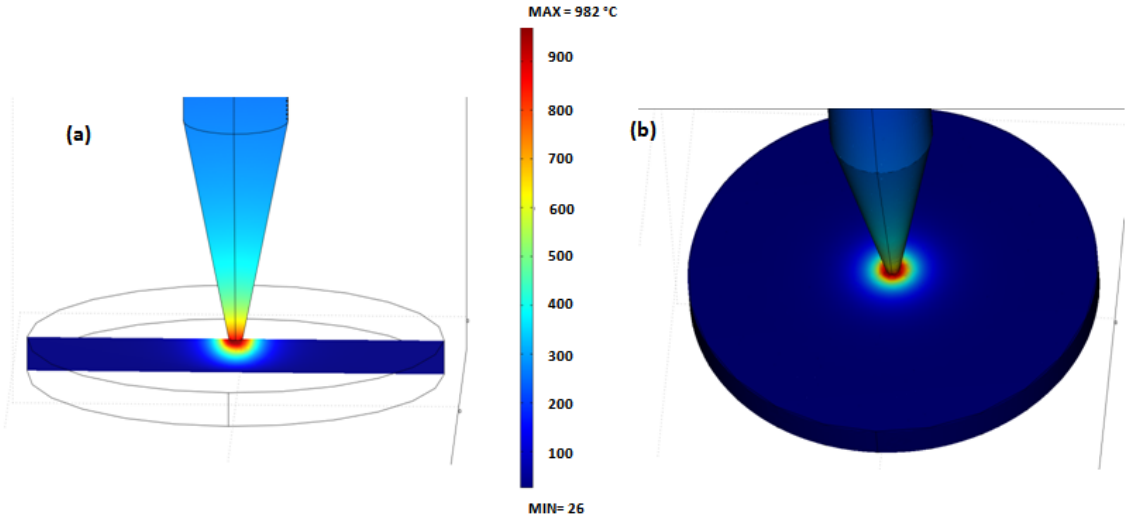


Figure 5.14 Calculated temperature distribution in CATS. (a) cross-sectional view and (b) 3D view

## 5.3 Fabrication of Micro-Functionally Graded Nickel using CATS

The unique tip-specimen configuration in CATS allows for the generation of locally controlled micro-scale temperature and current distributions that can result in significantly large micro-structural gradients. This ability to selectively apply spatial temperature and current distributions on such a small scale can potentially result in the production of porous "micro-scale" functionally graded materials (μ-FGM) under short electric current exposure times and without the need for sequential powder deposition approaches as mentioned earlier in section 4.2.1.3 (which could be more complicated as the size scale is reduced). The CATS approach could open the door for the production

of μ-FGM porous components, or larger 2D and more complex lightweight structures if a moving tip-approach is used, where complicated shapes can be sintered. However before such goals can be realized, it is important to confirm that such unique conditions can indeed result in micro-scale variations in pore content and size, and determine if they can be controlled for example by simply changing the initial green density or particle size. In this section the influence of green density and particle size on the micro-scale porosity profile and pore size distribution for porous μ-FGM produced using CATS is investigated.

Figure 5.15 shows the compaction curve for the 3-7 μm carbonyl nickel used in the present study showing the effect of pressure on fractional green density. The curve is well fitted to the compaction model by Jones [104,105] shown in 5.2 which takes into account particle rearrangement with $R^2$ value of 0.98 giving values for the powder constant θ (427.4) and the particle rearrangement term B (-829.3).

$$f_G = 1 - (1 - f_D)exp\ (B - \theta P) \quad 5.2$$

Where $f_G$ is the fractional green density, $f_D$ is the fractional apparent density, P is the compaction pressure. The equation allowed the selection of the appropriate compaction pressures that would result in the targeted fractional green densities for our present study.

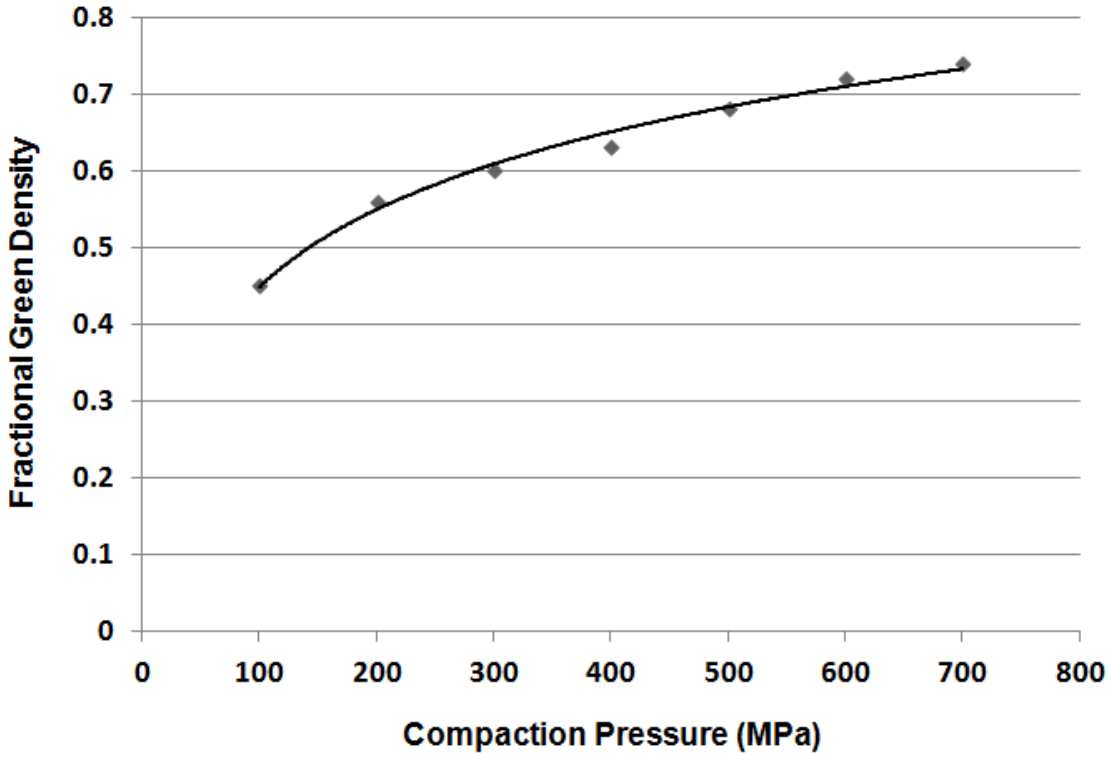


Figure 5.15 Carbonyl nickel (INCO. 123) compaction curve

All sintered specimens under the investigated processing parameters exhibited a highly densified ($\geq$ 99.8%) locally sintered region beneath the tip, which will be referred to hereafter as the process zone. The process zone is a comparatively highly electrically and thermally conductive region that is constantly growing during CATS. Its growth and evolution occurs at the more porous and hence more resistive (heat generating) interface with the remaining green compact. The growth is manifested in first the emergence of small densified regions at the outer boundaries of the process zone (which could be a result of the local microstructural variations) which would extend or grow into the green compact. Similar process zone evolution has been described for NiTi intermetallics [82]. Figure 5.16 shows an example of the micro-

structural modification of the green compact due to localized sintering beneath the tip. Of particular interest to this present study is the region below the process zone, which represents the porous μ-FGM region. Due to the locally imposed micro-scale temperature and current distributions, the microstructure is in turn modified, and generates significant micro-scale gradients in porosity underneath the tip. Porosity measurements were taken starting at ~150 μm beneath the process zone, which avoids any of the mentioned small sintered outgrowths.

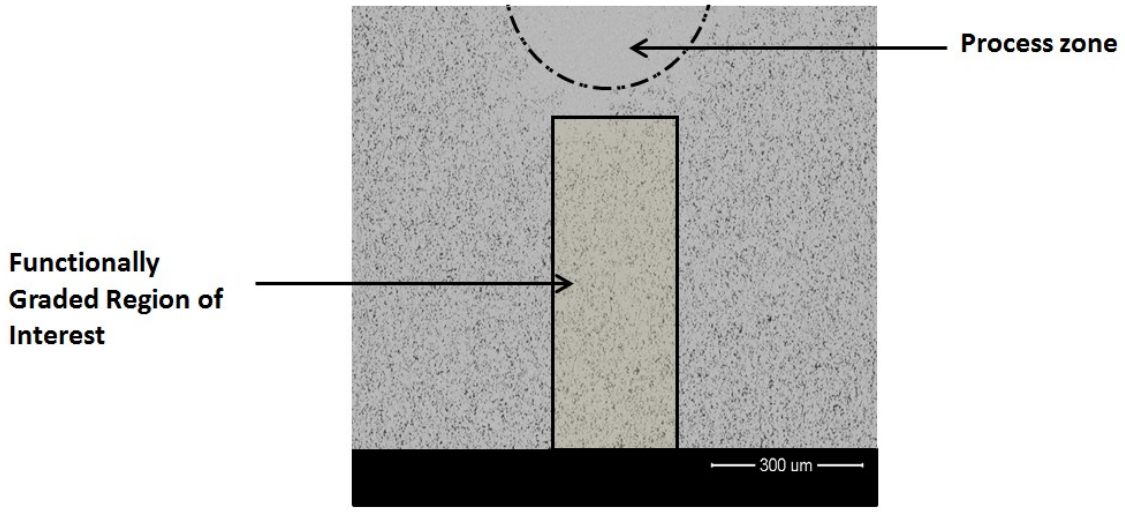


Figure 5.16 Scanning electron micrograph of the cross-section of the powder compact underneath the tip

Indeed, Figure 5.17 shows scanning electron micrographs of configurations A, B and C showing a spatial increase in porosity away from the process zone. It should be mentioned that this is facilitated by the application of a continuous electric current, which allows more heat conduction to the specimen, in contrast to the pulsed current application used in previous studies, which favored more localized sintering [78, 82].

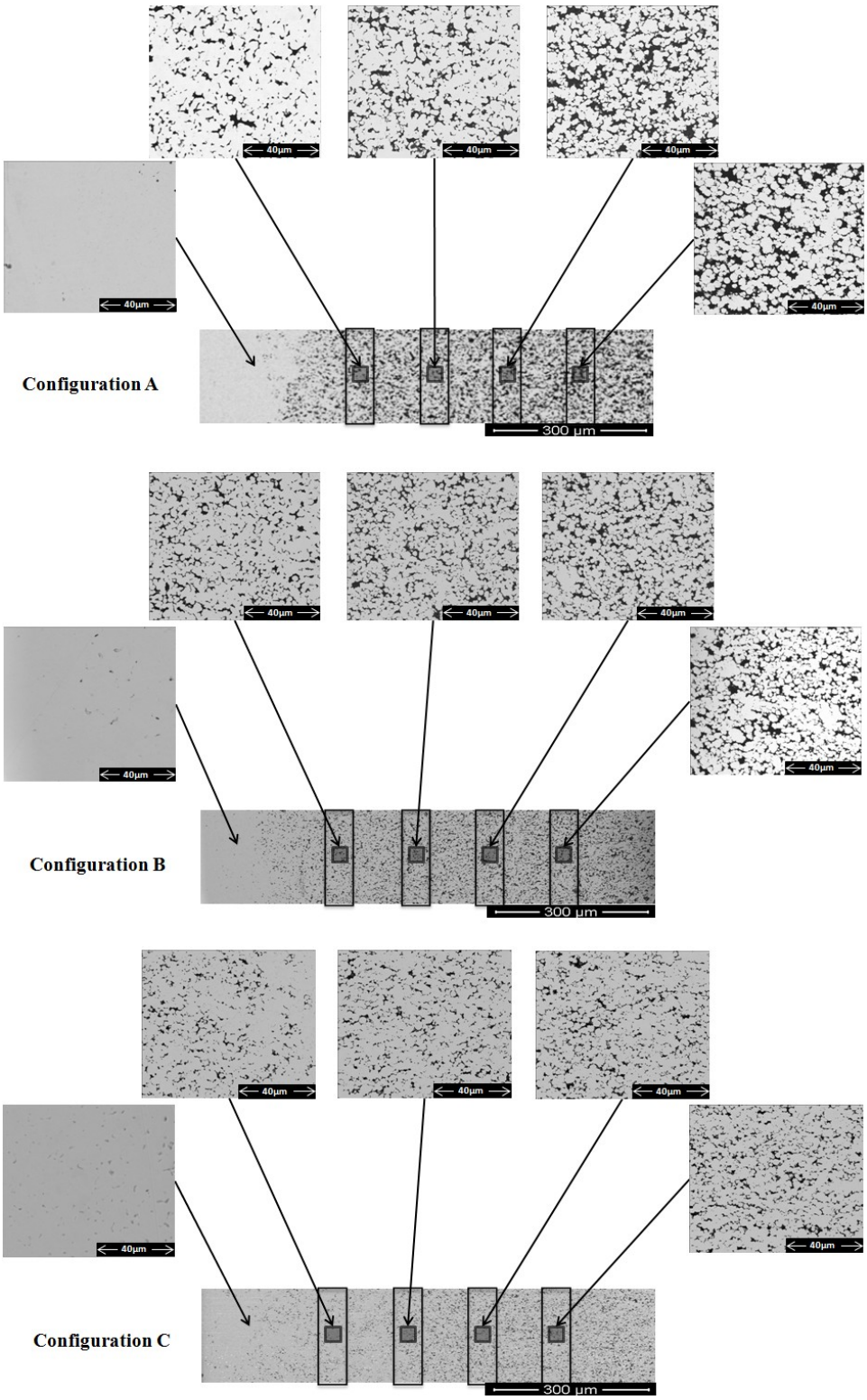


Figure 5.17 Scanning electron micrographs for configurations A, B and C

Image analysis measurements of the pore content (Figure 5.18) shows that for all fractional green densities investigated, as the distance (on the micro-scale) away from the process zone increases, the fractional porosity increases, giving rise to a spatial change in porosity which can form the basis for the production of porous μ-FGMs. The porosity profile exhibits an initial steep increase over a distance of ~150 μm followed by a gradual one for all fractional green densities investigated. The effect of fractional green density is manifested in a number of ways. First, 150μm away from the process zone, the increased porosity level is inversely proportional to the initial green density, where the lowest green density shows the highest porosity increase, this could be a direct result of a decreased thermal conductivity away from the process zone with decreased green density. Second, at any given distance along the micro-functionally graded region the porosity content increases with increase in initial fractional green density.

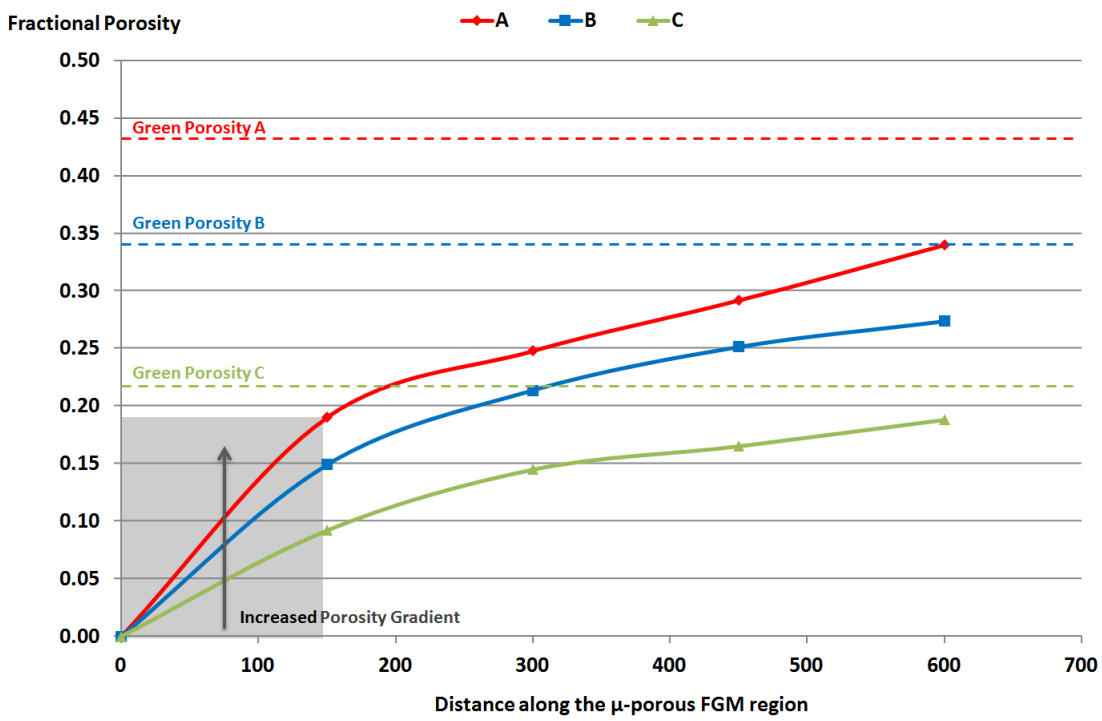


Figure 5.18 Spatial variation in porosity along the μ-FGM for configurations A, B and C (also indicating the initial porosity level of the green compact for each configuration)

Once again if the densification parameter Ψ is considered with respect to distance beneath the process zone for configurations A-C an interesting finding is revealed (Figure 5.19). For all specimens the densification parameter decreases with distance away from the process zone which is expected. However, although the data for configurations B and C seem to overlap, configuration A shows a departure from the other two where a comparatively higher densification parameter is realized at distances greater than a 150μm into the FGM region. The unique tip/specimen setup in CATS provides for a complex interplay between three influential factors (thermal conductivity of the powder compact, initial fractional green density and temperature profile across the thickness of the specimen). The fractional green density can affect the thermal

conductivity, and electrical resistivity (the latter increasing with a decrease in green density, giving rise to greater Joule heating). Despite being subjected to the same current, it is expected that the configuration with the lowest green density would generate the highest temperatures beneath the tip, due to its increased resistivity, giving rise to a modified temperature profile. Despite the low thermal conductivity and initial green density of configuration A, the increased temperature generated may have had a dominant effect on the observed increase in the densification parameter, compared with other factors.

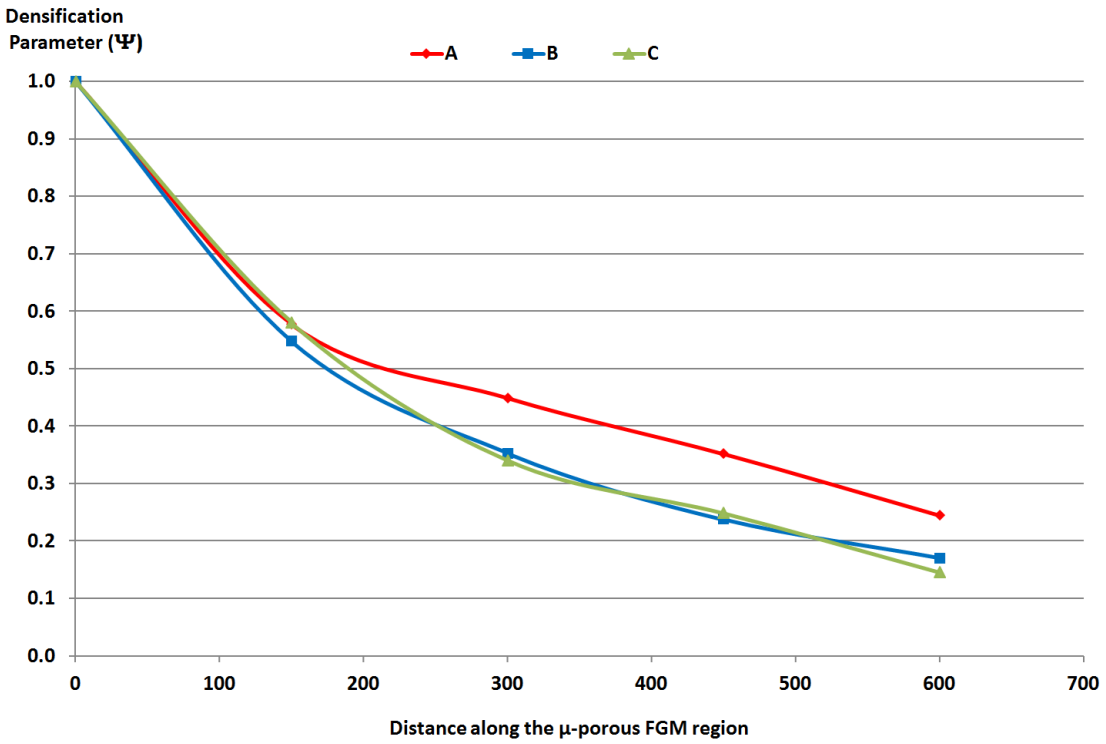


Figure 5.19 Densification parameter Ψ calculated centrally along the specimen thickness for each configuration

In porosity analysis it is often useful to consider a projected area equivalent spherical diameter to depict the size of irregular pores [106,107] as such Figure 5.20

shows how the pore size distribution changes along the length of the μ-FGM for configurations A-C. Due to resolution limits on micrographs the data was considered for pore sizes in excess of 2.5 μm projected area equivalent spherical diameter. Although this does not cover the full spectrum of the pore size distribution it can provide important insight as to the relative shift in pore size with distance along the μ-FGM as well as different initial green densities. It can be seen that for all green densities, as the distance away from the process zone increases, there is an increase in the percentage of larger pores. It can also be seen that the percentage of larger pores increase with the decrease in initial green density at any given distance from the process zone. In fact, at higher green densities (configuration C) no pores larger than 5 μm diameter were observed at any distance less than 400 μm, while the lowest green density (configuration A) had an open pore structure beyond such distance.

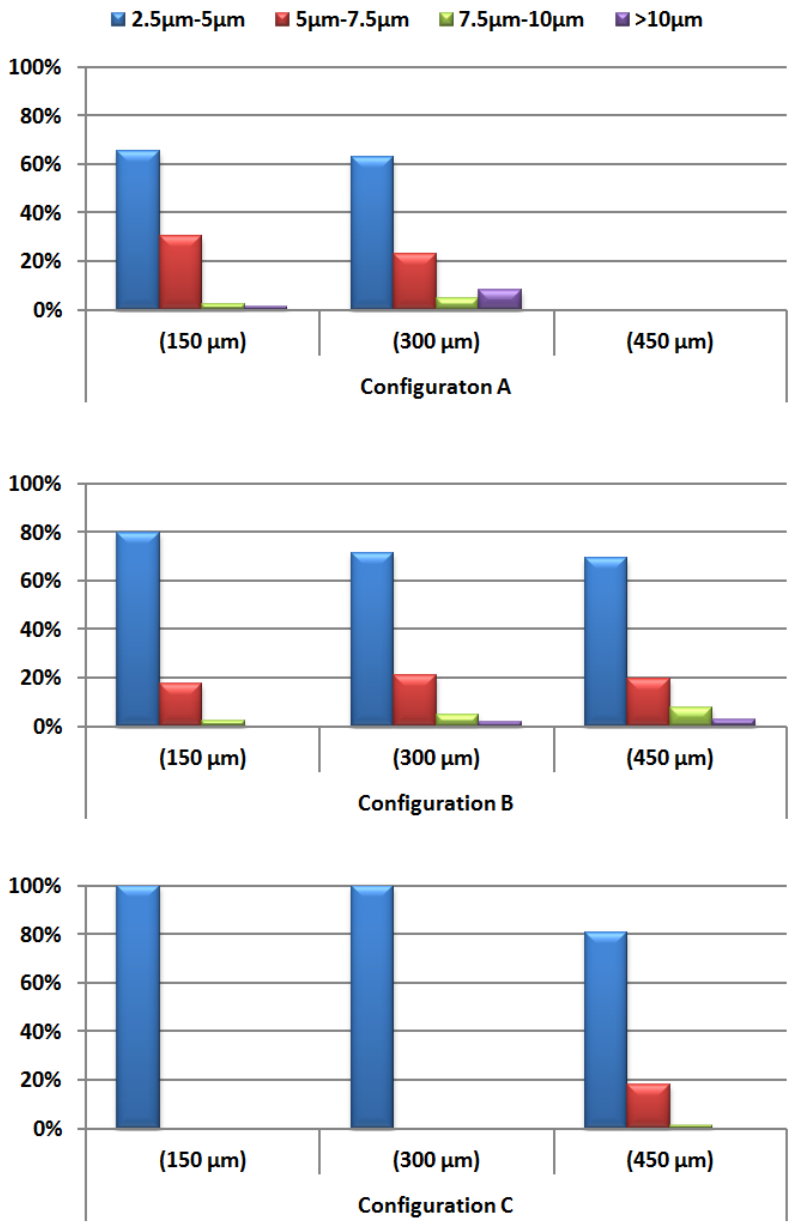


Figure 5.20 Pore size distribution for configurations A, B and C along the µ-porous FGM region

Results from Vicker's micro-hardness testing showed that at 150 µm and 450 µm levels beneath the process zone, the microhardness is proportional to the initial green density which is expected as less porosities are present and at any given level the number of larger size porosity decreases with the increase in initial green density.

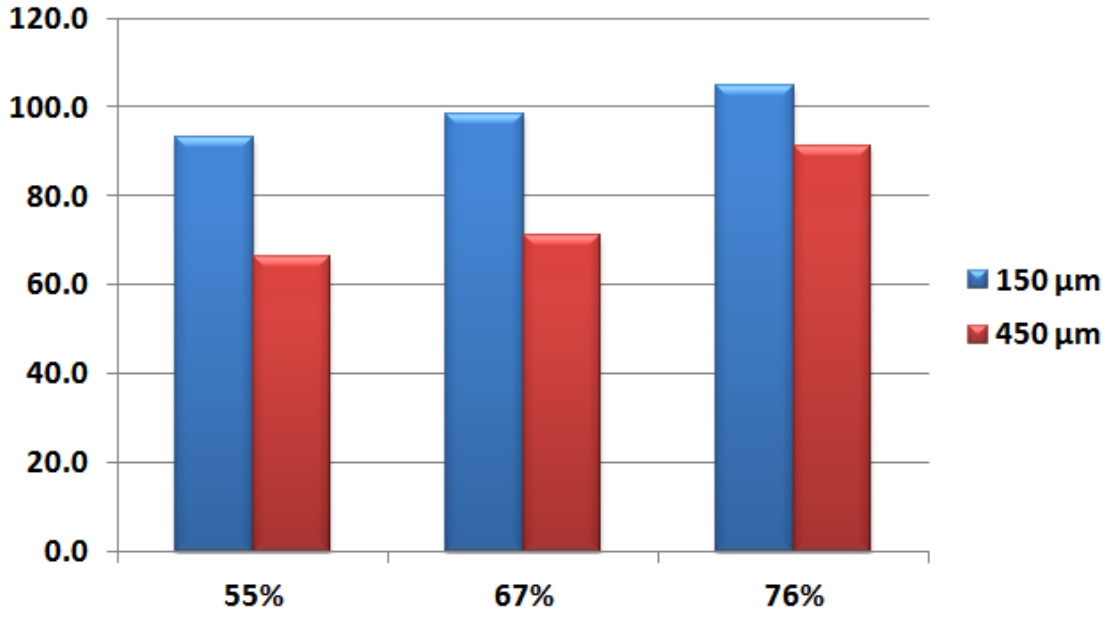


Figure 5.21 Vicker's microhardness measurements taken at 150 µm and 450 µm below the process zone for all investigated green densities

In contrast, a decrease in particle size from 3-7 µm to 0.5-1µm (configuration D) resulted in greatly enhanced densification beneath the tip and no clear observed µ-FGM. It is believed that the increased resistivity and consequently increased temperature generated due to Joule heating in addition to the enhanced sinterability at lower particle sizes resulted in high levels of densification beneath the tip under the present investigated conditions. Figure 5.22 shows that even at a distance ~550 µm from the process zone, highly densified microstructures are generated. This high level of densification even extends down to the bottom of the specimen. The maximum level of porosity (which was very small in size in comparison to the other configurations investigated) seen within these regions was ~3.8%, which were all closed, hence a µ-FGM as in the case of configurations A-C was not established under these conditions. Presumably a lower applied current and shorted current exposure times may provide for

the production of μ-FGMs at a much smaller pore size scale, which is the subject of future investigations.

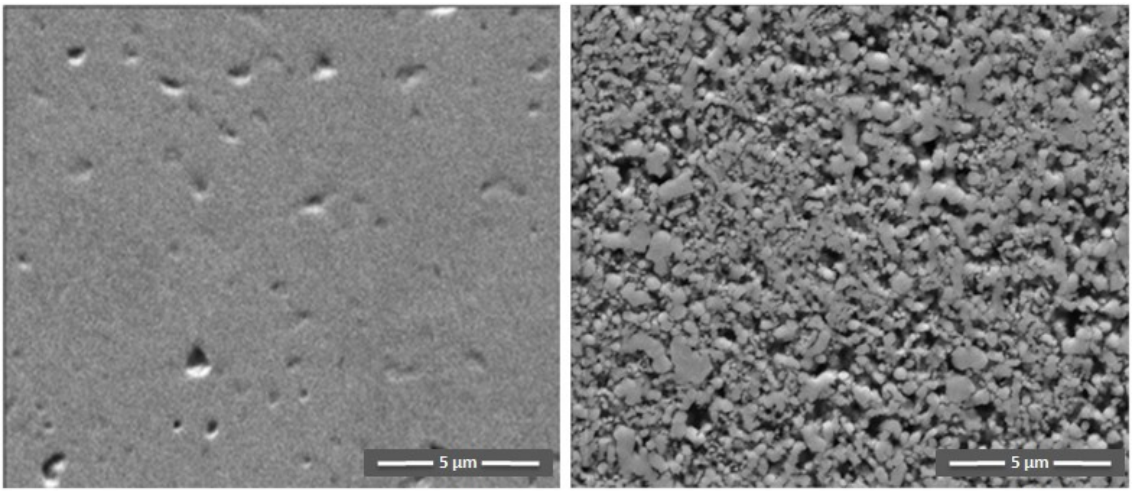


Figure 5.22 Scanning electron micrograph of configuration D taken at high magnification at a distance ~550 μm below the process zone

## 5.4 Moving μ-CATS Configuration

The stationary tip results provide important insight as to the effects of green density and particle size on the sintering process in CATS. The results however were focused on the sintering of regions typically several hundred micrometers in size. However, in order to take CATS to a new level where extended micro-scale features with consolidated thickness as low as a few microns, tip size and motion need to be considered. Such an extraordinarily high precision in localized sintering would have a number of benefits. For example, the approach could potentially open the door to new low-cost thin film manufacturing technology. In addition, selective individual particle-particle bonding could for the first time become possible under current activation. To enable such an approach, it is imperative to use a high precision machine that would

accommodate the use of previously un-explored ultra small conducting tips, and allow both precision movement and speed control. Such a machine has been indeed been manufactured at SDSU in Professor Kee Moon's Nano-mechatronics Lab (please see the experimental procedures section). It is important to point out that once the tip size becomes that small (10-50 μm as investigated in this dissertation) it suddenly becomes comparable to the powder size, unlike any other CATS previous investigation.

Both copper and nickel powder were used in the investigations with sizes ranging from 500nm all the way to sizes greater than 45 μm. The variation in particle size was to serve two purposes: 1. Investigate the effect of current and tip speed on the production of ultra thin consolidated layers over a controlled length by using ultrafine powder. 2. To investigate the ability of CATS to generate particle-particle bonds. Such investigations also necessitates consideration of green density, since lower green densities give rise to greater inter-particle spacing, with the tip size scales under investigation, this also becomes an important issue that needs to be considered. As such, green densities between 57-78% were also investigated.

Both nickel and copper particles with sizes between 500nm and 1μm were used in these investigations. Different moving μ-CATS processing parameters were investigated to examine their effect on the surface as well as level of subsurface consolidation on the micro-scale.

### *5.4.1 Effect of applied DC current*

Figure 5.23 shows the trace of the 7G-10 micro-tip on a 500nm copper powder compact under different current inputs with a constant speed of 2.4 mm/s. It can be seen that the highest current setting (9A) resulted in smoother consolidated line (Figure 5.23-c) due to higher generated temperatures. The line thickness also appears to increase with increase in current due to the taper shape of the tip, which will sink into the material as it gets consolidated due to high temperatures generated. A micro-crack also appears parallel to the consolidated line under 9A. The origin of these cracks appear to be from the initial contact and sustained current input prior to tip movement, due to thermally induced stresses and surface shrinkage. We cannot also discount the fact that thermal stresses and consolidation effects during tip movement could also promote such cracks.

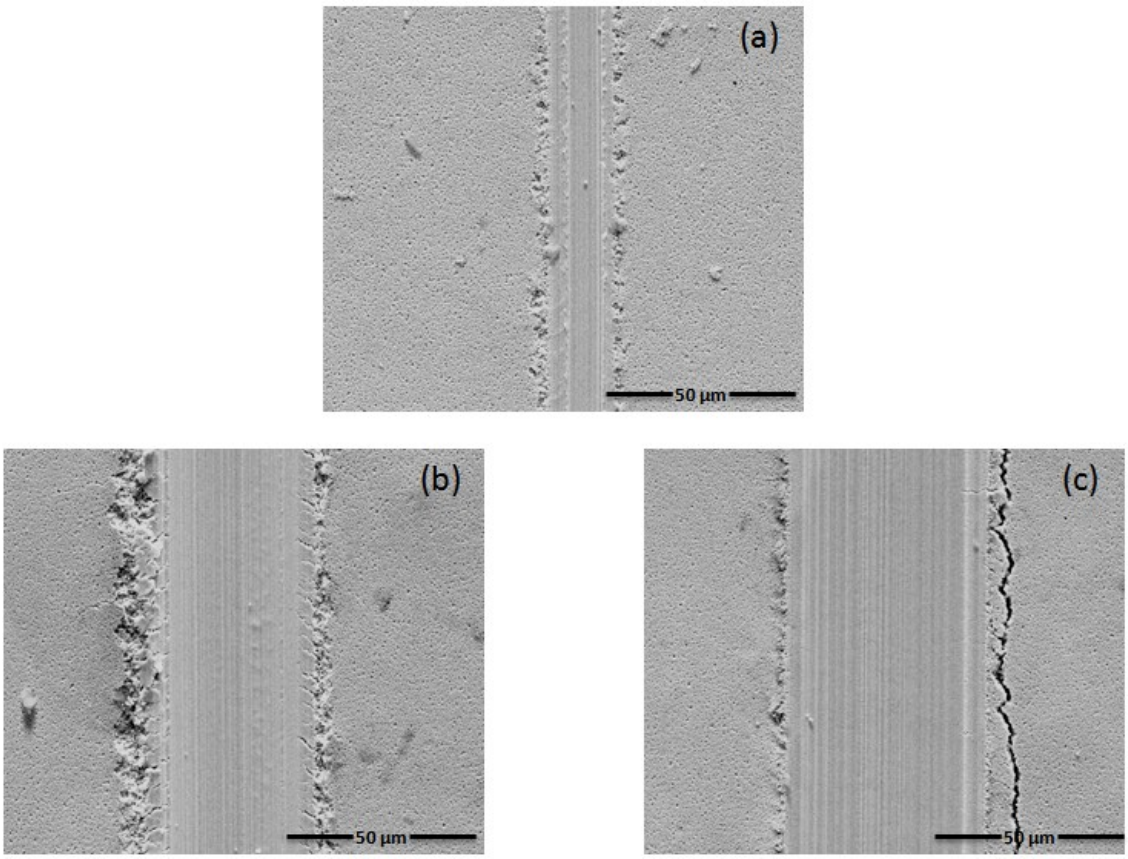


Figure 5.23 Trace of a micro-tip under a direct current of (a) 0 A, (b) 3 A and (c) 9 A

To characterize the sub-surface degree of consolidation, sintered lines were fractured across their path in order to observe the fractured surfaces. An example of this is seen in Figure 5.24, showing micro-scale full consolidation of 500nm copper particles to depths of ~2 µm using the 7G-50 tip and a current input of 12.9A. A similar level of micro-scale consolidation was also observed when using the 7D-10 tips with currents of 6A inputs. Similar investigations for a specimen subjected to the same tip movement but without the application of current showed closely packed individual distinct particles under the tip with no evidence of sintering (Figure 5.25).

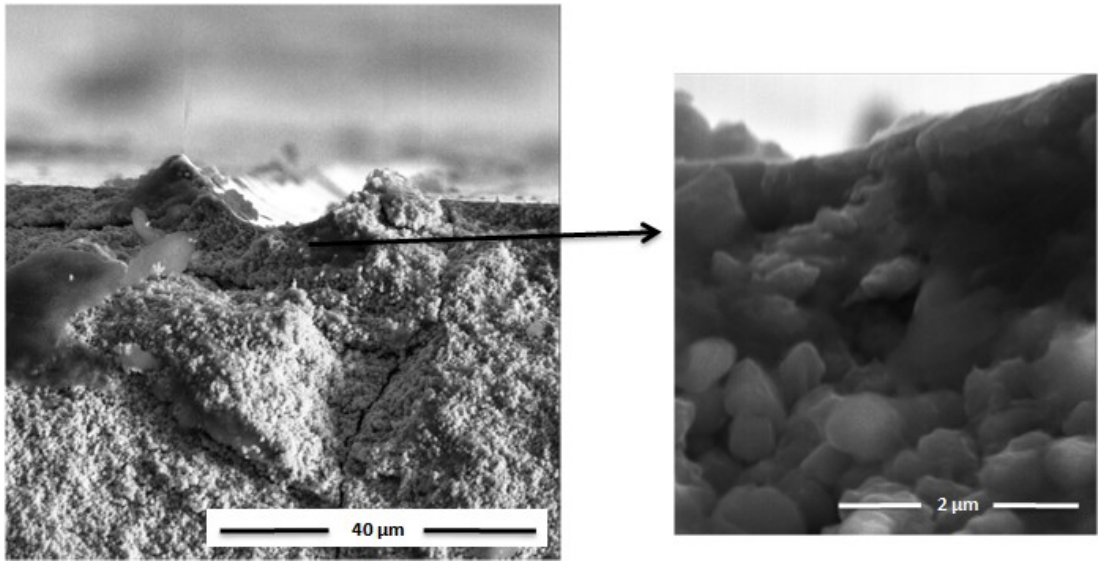


Figure 5.24 Fractured surface of a copper powder compact showing the subsurface beneath a consolidated line (12.9A, 0.2mm/sec)

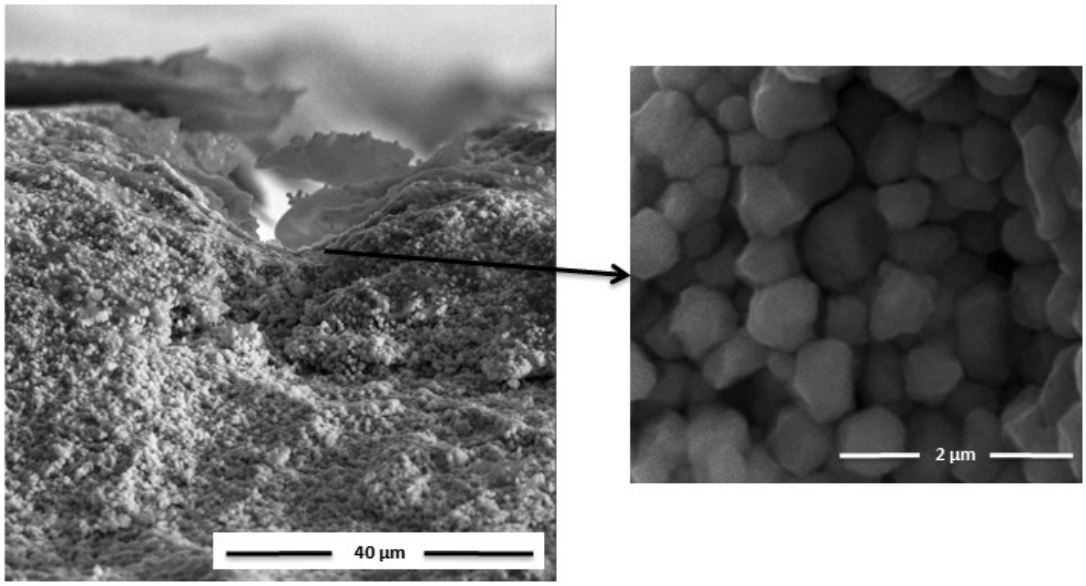


Figure 5.25 Fractured surface of a copper powder compact showing the subsurface beneath a moving tip without the application of current

Nickel powder with a similar particle size (0.5 - 1µm) was also investigated using the 7G-10 tips. Figure 5.26 shows that a layer of about 6-7 µm underneath the surface is consolidated to near full density, which is approximately thrice the size of that produced

under similar conditions for the copper particles as mentioned above. This is believed to be due to the marked difference between the thermal conductivities (K) and electrical conductivities (σ) between copper ($K_{Cu}$ =398 W/m-K and $\sigma_{Cu}$ =5.88 E7 S/m) and nickel ($K_{Ni}$ =60.7 W/m-K and $\sigma_{Ni}$ =1.56 E7 S/m) [108].

It is important to point out that the densification mechanism imposed by micro-scale moving tip under the investigated processing parameters is inherently different from that observed for the stationary tip configuration under prolonged current exposure time. Here the tip motion and tip-material contact promotes combined effects of shear deformation, current-activation and local heating to generate the observed micro-scale consolidated regions. Such microstructures resemble those observed for high shear deformation processes such as equal channel angular pressing (ECAP). This mechanism helps to ensure the locality of the densification to be within the micrometer range.

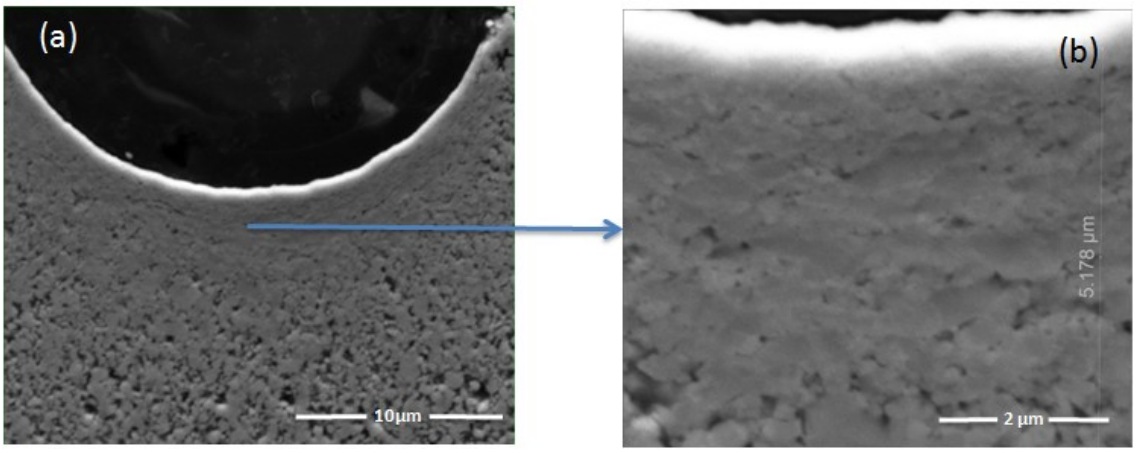


Figure 5.26 cross-section of a nickel powder compact at the site of a consolidated line (a) and a higher magnification image of the subsurface (b)

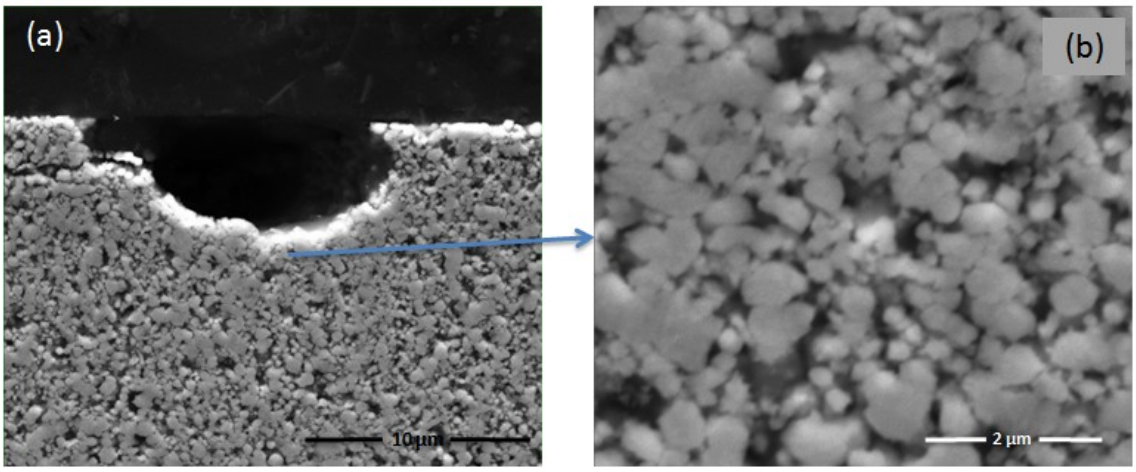


Figure 5.27 cross-section of a nickel powder compact at the site of a moving tip with zero current (a) and a higher magnification image of the subsurface (b)

### *5.4.2 Effect of tip speed*

The speed of the moving tip (under applied electric current) is expected to have a major effect on the quality of the consolidated line as slower speeds result in a higher exposure time to electric current. Figure 5.28 shows a smoother line produced under a lower tip speed configuration for a copper powder compact. Another advantage of slower speeds and prolonged current exposure times is crack healing. Figure 5.29 shows a sintered line on a nickel powder compact at a speed of 1.6 mm/s. lateral cracks at almost equal intervals took place along the line due to possible thermally induced tip local stresses. This was not the case when a lower speed was applied (0.2 mm/s) as seen in Figure 5.30. The higher magnification image shows traces of cracks that would have formed and healed under the slow moving tip which gives enough current exposure time to promote local heating.

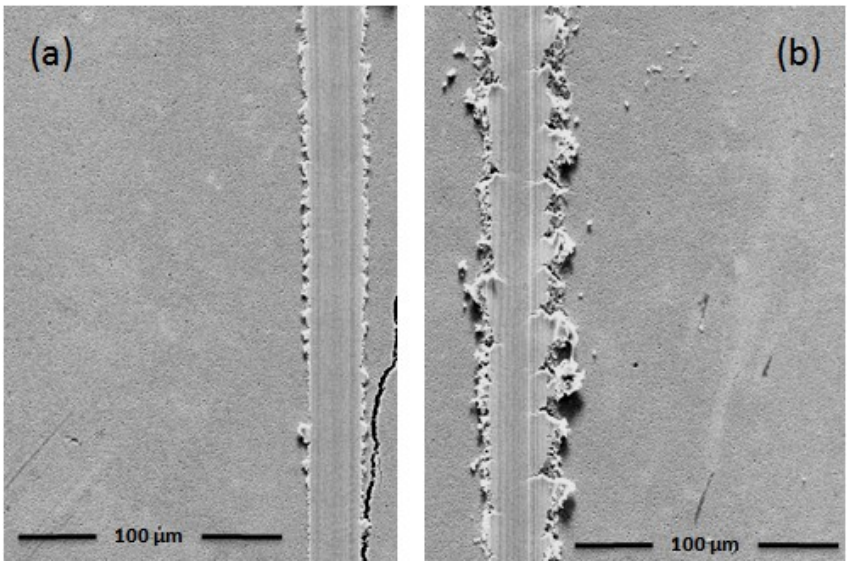


Figure 5.28 Lines consolidated under 6 A of current at 0.2 mm/s (a) and 0.8 mm/s (b)

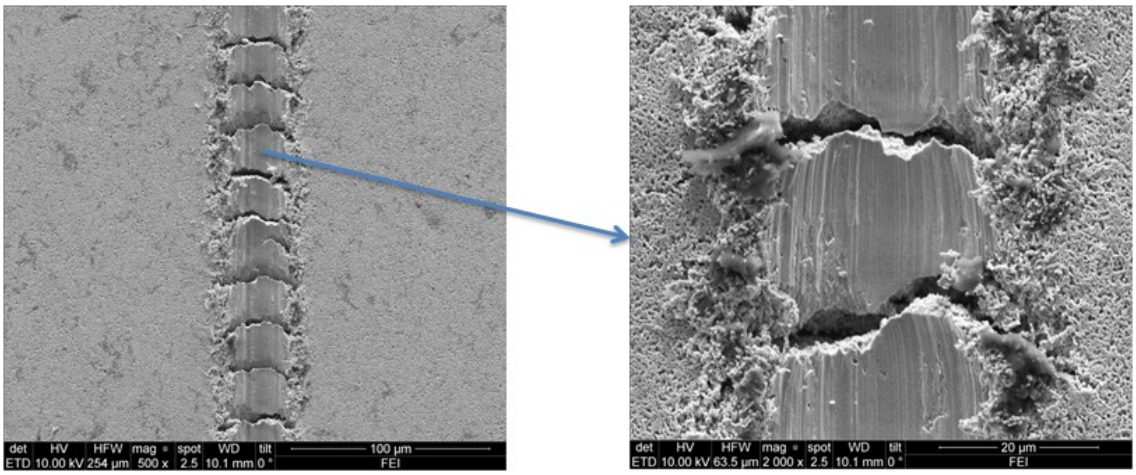


Figure 5.29 Trace of a fast moving (1.6 mm/sec) 7G-10 tip (6 A) on a nickel powder compact (left) and a higher magnification image (right)

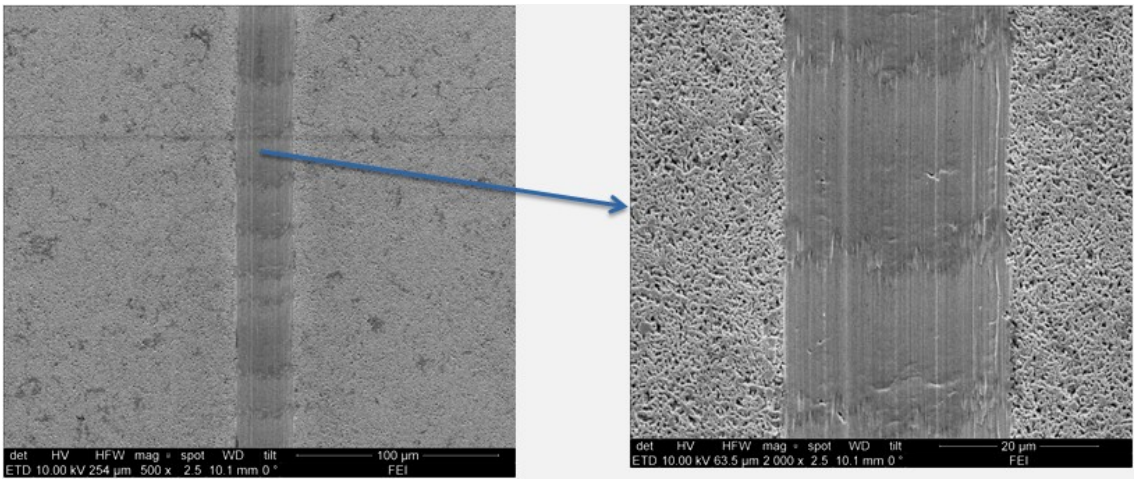


Figure 5.30 Trace of a slow moving (0.2 mm/sec) 7G-10 tip (6 A) on a nickel powder compact (left) and a higher magnification image (right)

### *5.4.3 Particle-particle bonding using µ-CATS*

#### 5.4.3.1 Effect of particle size

As mentioned earlier, once the particle size approaches the size of the tip, it becomes an interesting problem as the gaps between particles will also compare significantly to the size of the tip. Figure 5.31-a shows a scanning electron micrograph of a trace of a 7G-50 tip on a powder compact with >45 µm particle size without the application of current. Some clear major discontinuities are observed as the tip is expected to go over significantly large size gaps. When the same conditions were applied to a powder compact with <45 µm particle size the discontinuities in the trace left behind the tip seemed to be smaller due to smaller size gaps (Figure 5.31-b). As electric current is introduced to the tip (for both powder compacts) a consolidated line appears in the wake of the tip due to the generation of higher local temperatures (Figure 5.32). However, it can be seen that the line on the larger particle size compact appears to have some deviations from a straight line path as the large particles/pores setting will

create obstacles to the movement of the tip. Also higher temperatures are expected to be generated in the smaller particle size powder which contributes to the observed higher quality of the consolidated line.

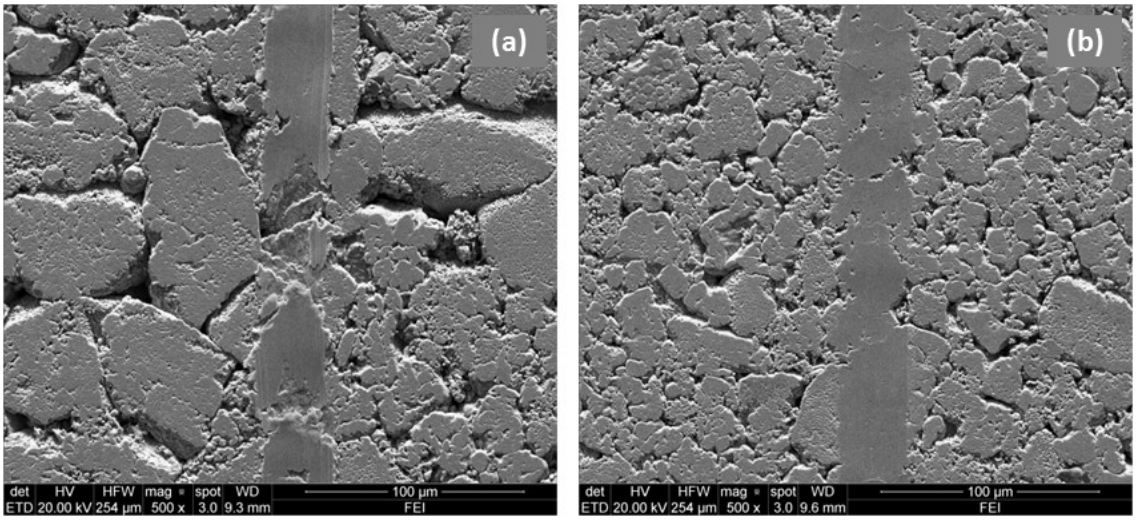


Figure 5.31 trace of a 7G-50 tip (0A) on nickel powder compacts with a $45^{+}$ µm particle size (a) and a $45^{-}$ µm particle size

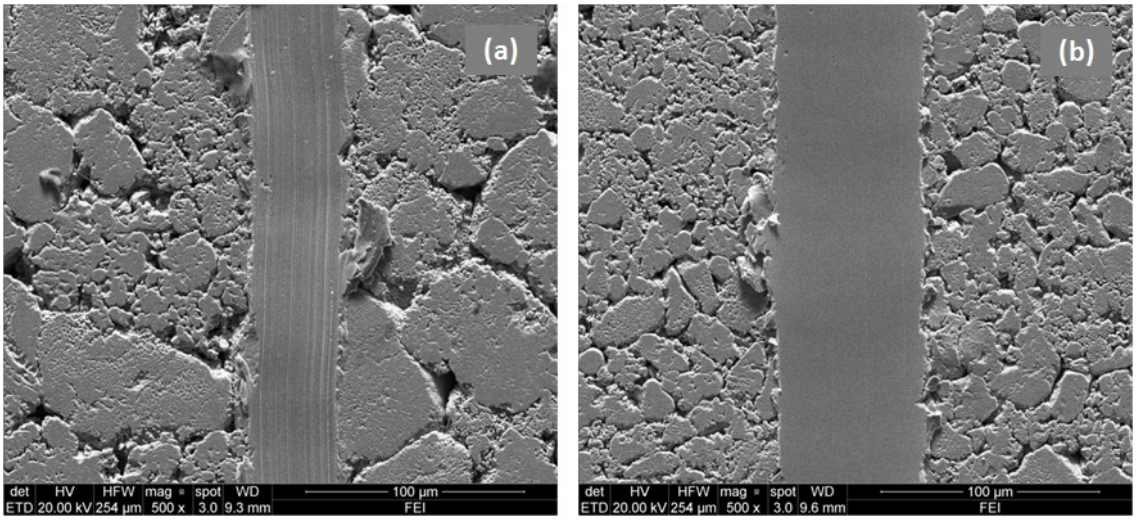


Figure 5.32 trace of a 7G-50 tip (12.9 A) on nickel powder compacts with a $45^{+}$ µm particle size (a) and a $45^{-}$ µm particle size

5.4.3.2 Effect of green density

Similar to the effect of particle size on the quality of the consolidated line, the green density will have a major effect as much larger size pores/gaps are expected in lower green density powder compacts. Figure 5.33 shows a consolidated line using a 7G-50 tip. The difference in line quality is very obvious as the tip could not overcome the large gaps between particles in the lower green density specimen resulting in large lateral cracks.

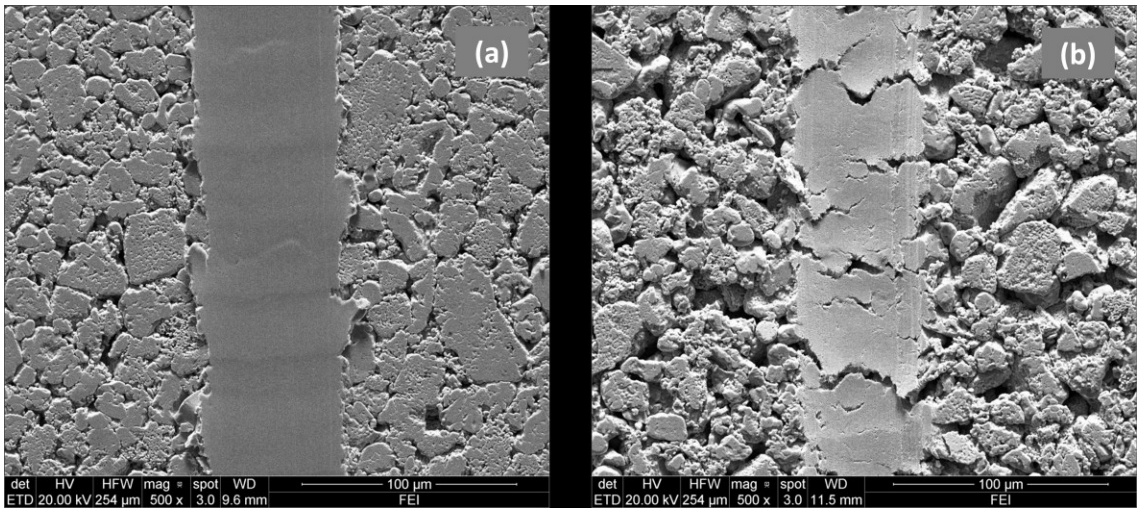


Figure 5.33 Consolidated line under 12.9 A applied current for 45$^{-}$ µm powder compacts with green densities (a) 77% and (b) 57% of theoretical

# 6 CONCLUSIONS

Due to the local nature of the Joule heating source in CATS, significant spatial and temporal temperature distributions are generated during processing. For a given particle size the lowest green density specimens with the lowest number of particle-particle contact/contact area generated the highest temperatures. Also at a given green density as the particle size is decreased (also resulting in an increase in particle-particle contact points), the temperature in the immediate vicinity of the tip is also increased. The concept of "effective current density" was also introduced for the first time to help explain the findings, together with thermal and electrical conductivity of powder-based materials. Spatial temperature measurements show that lower green densities give rise to an enhanced localization effect, where heat conduction away from the tip is reduced due to the lower thermal conductivity compared with higher green densities. A finite element model was developed revealing surface and subsurface temperature profiles in CATS, which were supported by experimental findings.

Under the stationary tip configuration and using a continuous applied current, the unique local temperature and current distributions were used to successfully process localized micro-scale functionally graded (μ-FGM) porous regions of controlled porosity profiles and pore size distributions after only 30 seconds of electric current exposure. Initial green density was found to have a direct influence on the size of the μ-FGM region, where a decline in initial green density results in a narrower profile at any given porosity limit. For all investigated initial green densities, the percentage of pores

with large equivalent spherical diameters increased with an increase in distance away from the highly densified process zone. Along the μ-FGM, the lowest green density configuration showed the highest densification parameter. At 78% initial green density, pores larger than 5 μm were only observed at distances greater than 400 μm. Moreover, under the present investigated conditions, an increase in particle size from 0.5-1.0 to 3-7 μm allowed for the production of micro-scale functionally graded porosity and the avoidance of large scale powder consolidation under the tip.

Through the use of a novel precision controlled micro-CATS machine that utilizes micro-tips, and control of current and tip speed we have successfully limited the densification to only a few micrometers beneath the surface of the compact. This gives rise to the processing of highly consolidated micro-features of "thin film" scale. Lower tip speeds and higher currents in μ-CATS produce higher quality consolidated lines due to longer current exposure times which also promote a microstructural healing effect. The thermal and electrical conductivity of the powder was also found to affect the scale of consolidation, as such copper powders with significantly higher electrical and thermal conductivity compared with nickel gave rise to reduced Joule heating and enhanced heat spreading resulting in thinner consolidated features.

The effect of the tip size to particle size ratio revealed an important dependence on the inter-particle spacing. As such, smaller particles with smaller inter-particle spacing relative to the tip size were found to result in better consolidation and bridging between particles following the passage of the current. Lower green densities are not

preferred in the moving tip configuration as large gaps (inter-particle spacing) result in discontinuities in the consolidated line with and without current application.

# 7 FUTURE RECOMMENDATIONS

A number of recommendations can be made for future research regarding tip sintering.

1. Investigation of the effect of applying current through multiple tips on the current and temperature distribution within specimen as well as the shape and size of the sintered regions.
2. In moving-CATS, electric current can be applied through a moving blade instead of a moving tip to generate micro-scale two dimensional features
3. In-situ observation of microstructural evolution during CATS using a miniature device that can be placed under a light microscope
4. The use of macro-scale tips and sequential powder deposition to enable rapid 3D large scale artifact production which is currently a challenge in the SPS industry

## REFERENCES

1 W. Chen, U. Anselmi-Tamburini, J.E. Garay, J.R. Groza, Z.A. Munir (2005) Fundamental investigations on the spark plasma sintering/synthesis process I. Effect of dc pulsing on reactivity. *Materials Science and Engineering* A 394:132-138

2 N. Chennoufi, G. Majkic, Y. C. Chen, K. Salama (2009) Temperature, current and heat loss distribution in reduced electrothermal loss spark plasma sintering. *Metallurgical and Materials Transactions* 40(A): 2401-9

3 X. Song, X. Liu, J. Zhang (2005) Mechanism of conductive powder microstructure evolution in the process of SPS. *Science in China Series E, Engineering & Materials Science* 48(3):258-269

4 X. Song, X. Liu, J. Zhang (2006) Neck formation and self-adjusting mechanism of neck growth of conducting powders in spark plasma sintering. *Journal of the American Ceramic society*89(2):494-500

5 J.M. Frei, U. Anselmi-Tamburini, Z.A. Munir (2007) Current effects on neck growth in the sintering of copper spheres to copper plates by the pulsed electric current method. *Journal of Applies Physics* 101(11) :1149141-8

6 J.E. Garay, U. Anselmi-Tamburini, Z.A. Munir (2003) Enhanced growth of intermetallic phases in the Ni-Ti system by current effects. *Acta Materialia* 51: 4487-4495

7 C.E. Wen, M. Mabuchi, Y. Yamada *et al* (2003) Processing and characterization of porous aluminum. *Materials Science Forum* 426-432:417-422

8 S. Kawamura, T. Abe, H. Kuwano (2008) Tensile strength of superfine grained iron produce by MM-SPS method. *Journal of the Japan Society for powder Metallurgy* 55(7):509-514

9 B. Srinivasaro, K. Oh-ishi, T. Okhubo, K. Hono (2009) Bimodally grained high-strength Fe fanricated by mechanical alloying and spark plasma sintering. *Acta Materialia* 57: 3277-86

10 J. Gubicza, H. –Q. Bui, F. Fellah, N. Szász, G. Dirras (2008) Bulk ultrafine-grained nickel consolidated from nanopowders. *Materials Science Forum* 589:93-98

11 H. L. Zhang, J.-F. Li, K.F. Yao, L.D. Chen (2005) Spark plasma sintering and thermal conductivity of carbon nanotube bulk materials. *Journal of Applied Physics* 97(11):1143101-5

12 S.H. Risbud, C.H. Shan, A.K. Mukherjee, M.J. Kim, J.S. Bow, R.A. Holl (1995) Retention of nanostructure in aluminum oxide by very rapid sintering at 1150°C. *Journal of Materials Research* 10(2): 237-239

13 M. Omori (200) Sintering, consolidation, reaction and crystal growth by the spark plasma system (SPS). *Materials Science and Engineering* A287:183-188

14 R. Chaim, Z. Shen, M. Nygren (2004) Transparent nanocrystalline MgO by rapid and low-temperature spark plasma sintering. *Journal of Materials Research* 19:2527-31

15 C. Balazsi,Z. Shen, Z. Konya, Z. Kasztovsky, F. weber et al. (2005) Processing of carbon nanotube reinforced silicon nitride composites by spark plasma sintering. *Composite Science and Technology* 65:727-733

16 V.V. Patel, **A. El Desouky**, J.E. Garay, K. Morsi (2009) Pressure-less and current-activated pressure-assisted sintering of titanium dual matrix composites: Effect of reinforcement particle size. *Materials Science and Engineering* A507: 161-166

17 U. Anselmi-Tamburini, J.E. Garay, Z.A. Munir, et al. (2004) Spark plasma sintering and characterization of bulk nanostructured fully stabilized zirconia: Part I. Densification studies. *Journal of Materials Research* 19:3255-3262

18 Y. Gu, K.A. Khor, P. Cheang (2004) Bone-like apatite layer formation on hydroxyapatite prepared by spark plasma sintering. *Biomaterials* 25(18):4127-34

19 V. Gauthier, F. Bernard, E. Gaffet, Z.A. Munir, J.P. Larpin (2001) Synthesis of nanocrystalline NbAl3 by mechanical and field activation. *Intermetallics* 9(7):571-580

20 T.-Y. Um, T. Abe, S. Sumi (1999) Fabrication of intermetallic compounds by spark plasma sintering . *Journal of Materials Synthesis and Processes*7(5): 303-309

21 M. Mal'tsev (2003) Electric rolling of powder materials with a dielectric phase. *Powder Metallurgy and Metal Ceramics* 42(5-6):225-229

22 M. Mal'tsev (2005) Electric rolling of metal powders in roller electrodes. *Powder Metallurgy and Metal Ceramics* 44(5-6):222-227

23 K. Morsi, **A. El Desouky** (2009) Preliminary evaluation of spark plasma extrusion. *Proceedings of TMS Annual Meeting and Exhibition 2009*: 685-692

24 K. Morsi, **A. El Desouky**, B. Johnson, A. Mar, S. Lanka (2009) Spark plasma extrusion (SPE): prospects and potential. *Scripta Materialia* 61(4):395-398

25 K. Morsi, A.M.K. Essawi, P. Borah et al. (2010) Properties of single and dual matrix aluminum–carbon nanotube composites processed via spark plasma extrusion (SPE). *Materials Science and Engineering* A 527(21-22):5686-90

26 K. Morsi, A.M.K. Essawi, S.Lanka, A. Sayed, M. Taher (2010) Spark plasma extrusion (SPE) of ball-milled aluminum and carbon nanotube reinforced aluminum composite powders. *Composites Part A: Applied Science and Manufacturing* 41(2): 322-326

27 J. E. Garay (2010) Current-activated, pressure-assisted densification of materials. *Annual Review of Materials Research* 40:445-68

28 K. Morsi, K. Moon (2009) Current activated tip-based sintering. *USPatent* US2011/0262655 A1

29 German, R.M. (2005) Powder metallurgy and particulate materials processing. *MPIF*

30 German, R.M. (1996) Sintering theory and practice. *Wiley interscience publication*

31 A. Zavalingos, J. Zhang, M. Krammer, J.R. Groza (2004) Temperature evolution during field activated sintering. *Materials Science and Engineering* A379:218-228

32 G. Xie, O. Ohashi, N. Yamaguchi, A. Wang (2003) Effect of Surface oxide films on the properties of pulse electric-current sintered metal powders. *Metallurgical and Materials Transactions* 34A(11): 2655-61

33 K. Morsi, V.V. Patel, K.S. Moon, J.E. Garay (2008) Current-activated pressure-assisted sintering (CAPAS) and nanoindentation mapping of dual matrix composites. *Journal of Materials Science* 43(12):4050-56

34 J.E. Alaniz, J.R. Morales, J.E. Garay (2010) The current activated pressure assisted densification technique for producing nanocrystalline materials. *JOM* 62(2):58-62

35 M. Tokita (2010) Mechanism of Spark Plasma Sintering, *Ceramics* 044903: 605-608

36 J. Lux (1906) GB Patent 9020

37 R. Orru, R. Licheri, A. M. Locci, A. Cincotti, G. Cao (2009) Consolidation/ synthesis of materials by electric current activated/ assisted sintering. *Materials Science and Engineering* R 63:127-287

38 A.L. Duval d'Adrian (1922) U.S. Patent 1,430,724

39 S.L. Hoyt (1932) U.S. Patent 1,843,768

40 E.G. Gilson (1930) US Patent No. 1,756,857

41 G.F. Taylor (1933) U.S. Patent No. 1,896,854

42 K. Inoue (1966) U.S. Patent No. 3,250,892

43 K. Inoue (1967) U.S. Patent No. 3,317,705

44 K. Inoue (1967) U.S. Patent No. 3,340,052

45 S. Grasso, Y. Sakka, G. Maizza (2009) Electric current activated/assisted sintering (ECAS): a review of patents 1906-2008. *Science and Technology of Advanced Materials* 10:053001-24

46 V. Mamedov (2002) Spark plasma sintering as advanced PM sintering method. *Powder Metallurgy* 45(4):322-328

47 Z.A. Munir, U. Anselmi-Tamburini, M. ohyanagi (2006) The effect of electric field and pressure on the synthesis and consolidation of materials: A review on the spark plasma sintering method. *Journal of Materials Science* 41:763-777

48 1 Z.A. Munir, D.V. Quach, M. Ohyanagi (2011) Electric current activation of sintering: A review of the pulsed electric current sintering process. *Journal of American Ceramic Society* 94(1):1-19

49 T. Hungria, J. Galy, A. Castro (2009) Spark plasma sintering as a useful technique to the nanostructuration of piezo-ferroelectric materials. *Key Engineering materials* 11(8):615-631

50 M. Mulukutla, A. Singh, S.P. Harimkar (2010) Spark plasma sintering for multi-scale surface engineering of materials. *JOM* 62(6):65-71

51 D.M. Hilbert, A. Andres, D.V. Dudina *et al* (2008) The absence od plasma in "spark plasma sintering". *Journal of Applied Physics* 104:033301-5

52 H. Conrad (2000) Effects of electric current on solid state phase transformations in metals. *Materials Science and Engineering* A287:227-237

53 Z.H. Lai, H. Conrad, G.Q. Teng, Y.S. Chao (2000) Nanocrystallization of amorphous Fe-Si-B alloys using high current density electropulsing. *Materials Science and Engineering* A287:238-247

54 H. Conrad (2000) Electroplasticity in metals and ceramics. *Materials Science and Engineering* A287:276-287

55 D. Yang, H. Conrad (2001) Exploratory study into the effects of an electric field and of high current density electropulsing on the plastic deformation of TiAl. *Intermetallics* 9:943-947

56 H. Conrad (2002) Thermally activated plastic flow of metals and ceramics with an electric field or current. *Materials Science and Engineering* A322: 100-107

57 S.D. Antolovich, H. Conrad (2002) The effects of electric currents and fields on deformation in metals, ceramics, and ionic materials: an interpretive survey. *Materials and manufacturing Processes* 19(4):587-610

58 H.B. Huntington, in "Diffusion in solids", edited by A.S. Nowick and J.J. Burton (Academic Press New York, 1975):306

59 N. Bertolino, J. Garay, U. Anselmi-Tamburini, Z.A. Munir (2001) Electromigration effects in Al-Au multilayers. Scripta Materialia 44:732-742

60 M. Nanko, T. Oyaidu, T. Maruyama (2002) Densification of Ni-20Cr alloy coarse-powder by pulse current pressure sintering. *Journal of the Japan Institute of Metals* 66(2):87-93

70 G.Xie, O. Ohashi, K. Chiba, N. Yamaguchi, M. Song, K. Furuya, T. Noda (2003) Frequency effect on pulse electric current sintering process of pure aluminum powder. *Materials Science and Engineering* A359:384-390

71 K. Vanmeensel, A. Laptev,J. Hennicke, J. Vleugels, O. Van der Biest (2005) Modelling of the temperature distribution during field assisted sintering. *Acta Materialia* 53:4379-88

72 U. Anselmi-Tamburini, S. Gennari, J.E. Garay, Z.A. Munir (2005) Fundamental investigations on the spark plasma sintering/ synthesis process: II Modelling of current and temperature distributions. *Materials Science and Engineering* A394:139-148

73 Cincotti, A., Locci, A. M., Orrù, R. and Cao, G. (2007), Modeling of SPS apparatus: Temperature, current and strain distribution with no powders. *American Institute of Chemical Engineers Journal* 53:703–719

74 X. Wang, S.R. Casolco, G. Xu, J.E. Garay (2007) Finite element modeling of electric current activated sintering: the effect of coupled electrical potential, temperature and stress. *Acta Materialia* 55:3611-22

75 D. Tiwari, B. Basu, K. Biswas (2009) Simulation of thermal and electric field evolution during spark plasma sintering. *Ceramics International* 35:699-708

76 F. Mechighel, B. Pateyron, M. El Ganaoui, M. Kadja (2008) Study of thermo-electrical and mechanical coupling during densification of a polycrystalline material using COMSOL. *Proceedings of the COMSOL Conference 2008 Hannover*

77 E.A. Olevsky, L. Froyen (2009) Impact of thermal diffusion on densification during SPS. *Journal of American CeramicsSociety* 92(S1):122-132

78 E.A. Olevsky, L. Froyen (2006) Constitutive modeling of spark plasma sintering of conductive materials. *Scripta Materialia* 55:1175-78

79 E.A. Olevsky, S. Kandukuri, L. Froyen (2007) Consolidation enhancement in spark plasma sintering: Impact of high heating rates. *Journal of Applied Physics* 102:114913

80 Klaus Lichtinghagen, US patent no. 4420294 (1983)

81 Y. H. Ko, S. H. Chung, I. H. Oh, J. I. Cho, C. S. Kang (2007) Joining of aluminum foam/ aluminum metal by spark plasma sintering process. *Advanced Materials Research* 26-28:1349-52

82 L.Limeng, Y. Feng, Z. Yu, Z. Zhiguo, H. Qinglong (2010) Fast bonding α-SiAlON ceramics by spark plasma sintering. *Journal of the European Ceramic Society* 30:2683-89

83 J. F. Xu, X. B. Zhang, Y. J. Fei, H. F. Wu, Y. F. Ye,W. Li (2007) Joining of MoSis to 316L stainless steel using spark plasma sintering technique. *Material Science and Technology* 23(7:)875-879

84 S.S. Kim, S. Yamamoto, T. Aizawa, A. Yamamoto(2005) Experimental and theoretical evaluation on thermoelasticity for SPS-joined p-n module in Bi-Te system. *Materials Transactions* 46(7):1506-1513

85 W.Liu M. Naka. (2003) In Situ joining of dissimilar nanocrystalline materials by spark plasma sintering. *Scripta Materialia* 48:1225-1230

86 J. Fan, L. Chen, S. Bai, X. Shi (2004) Joining of Mo to $CoSb_3$ by spark plasma sintering by inserting a Ti interlayer. *Materials Letters* 58:3876-78

87 K.Morsi, K.S. Moon, S. Kassegne, R. Ugle, E. Villar (2009) Novel current-activated tip-based sintering (CATS): Localization of spark plasma sintering. *Scripta Materialia* 60:745-748

88 R.A. Ugle (2009) Effect of current density and tip speed in current activated tip-based sintering. Thesis, San Diego State University

89 E. P. Villar (2010) The effect of pressure on macro-scale current activated tip-based sintering of nickel. Thesis, San Diego State University

90 D.B. Elting (2010) Novel forming techniques using current activated tip-based sintering (CATS). Thesis, San Diego State University

91 M. Patel, K.S. Moon, S.K. Kassegne, K. Morsi (2011) Effect of current intensity and cumulative exposure time on the localized current-activated sintering of titanium nickelides. *Journal of Materials Science* 46: 6690-99

92 A. Numula, K. Morsi, K.S. Kassegne, K. Moon (2011) Exploratory investigations in reactive current activated tip-based sintering (CATS). *Proceedings of TMS Annual Meeting and Exhibition, San Diego 2011*

93 A. Numula, S. Kassegne, K.S. Moon, K. Morsi (2012) Current activated tip-based sintering of Ni-Al intermetallics. *Journal of materials Science* (submitted feb. 2012)

94 **A. El-Desouky**, K.S. Moon, S.K. Kassegne, K. Morsi (2011) Preliminary investigations on the effect of particle size and tip size in the current activated tip-based sintering (CATS) of nickel powder compacts. *Proceedings of the TMS Annual Meeting and Exhibition, San Diego 2011*

95 J. Zhua, Z. Lai, Z. Yin, J. Jeon, S. Lee (2001) Fabrication of ZrO2–NiCr functionally graded material by powder metallurgy. Materials Chemistry and Physics 68:130–135

96 S. Lo´pez-Esteban, J.F. Bartolome´, C. Pecharroma´ n, J.S. Moya (2002) Zirconia/stainless-steel continuous functionally graded material. Journal of the European Ceramic Society 22: 2799‑2804

97 L. Yongming , P. Wei, L. Shuqin, W. Ruigang, L. Jianqiang (2003) A novel functionally graded material in the Ti_/Si_/C system. Materials Science and Engineering A345: 99/105

98 T. Traini, C. Mangano, R.L. Sammons, F. Mangano, A. Macchi, A. Piattelli (2008) Direct laser metal sintering as a new approach to fabrication of an isoelastic functionally graded material for manufacturen of porous titanium dental implants. *Dental materials* 24: 1525–1533

99 K.Morsi, H. Keshavan, S. Bal (2004) Processing of grain-size functionally gradient bioceramics for implant applications. Journal of Materials Science: Materials in Medicine 15(2): 191-197

100 K.Morsi, H. Keshavan, S. Bal (2004) Hot pressing of graded ultrafine-grained alumina bioceramics. *Materials Science and Engineering A* 386: 384-389

101 D. Jankovic´ Ilic´, J. Fiscina, C. Gonzàlez Oliver, N. Ilic´, F. Mücklich (2007) Self formed Cu-W functionally graded material produced via powder segregation. *Advanced Engineering Materials* 9(7): 542-546

102 Y. Watanabe, Y. Iwasa, H. Sato, A. Teramoto, K. Abe, E. Miura-Fujiwara (2011) Microstructures and mechanical properties of titanium/biodegradable-polymer FGM for bone tissue fabricated by spark plasma sintering method. Journal of materials processing Technology 211(12): 1919-1926

103 D. M. Hulbert, D. Jiang, U. Anselmi-Tamburini, C. Unuvar, A. K. Mukherjee (2008) Continuous functionally graded boron carbide-aluminum nanocomposites by spark plasma sintering. *Materials Science and Engineering A* 493:251–255

104 T. Holland, D. Hulbert, U. Anselmi-Tamburini, A. Mukherjee (2010) Functionally graded boron carbide and aluminum composites with tubular geometries using pulsed electric current sintering. Materials Science and Engineering A 527: 4543-4545

105 M. Daio, K. Hasezaki, M. Hosogi, I. Yoshioka (2010) Sintering and mechanical properties of Fly-ash/NiCr compacts prepared by spark plasma sintering. Funtai Oyobi Fummatsu Yakin/ Journal of the Japan Society of Powder Metallurgy 57(10): 654-659

106 M. Omori, T. Kakita, A. Okubo, T. Hirai (1998) Pure WC/Mo functionally graded materials. Materials Science Forum 308(311): 53-58

107 G. Jin, M. Takeuchi, S. Honda, T. Nishiwaka, H. Awaji (2005) Properties of multilayered mullite/Mo functionally graded materials fabricated by powder metallurgy processing

108 H. Feng, Q. Meng, Y. Zhou, D. Jia (2005) Spark plasma sintering of functionally graded material in the Ti-$TiB_2$-B system. *Materials Science and Engineering* A 397:92-97

109 I.F. Machado,L. Giradini, I. Lonardelli, A. Molinari (2009) The study of ternary carbides formation during SPS consolidation process in the WC-Co-steel system. *International Journal of Refractory Metals & Hard materials* 27:883-891

110 M. Radwan, M. Nygren, K. Flodström (2011) Fabrication of crack-free SUS316L/$Al_2O_3$ functionally graded materials by spark plasma sintering. *Journal of Materials Science* 46:5807-5814

111 L.P. Lefebvre, G. Pleizier, Y. Deslandes (2001) Electrical resistivity of green powder compacts. *Powder Metallurgy* 44(3): 259-266

112 J.M. Montes, F.G. Cuevas, J. Cintas (2006) A new expression for the effective pressure on powders under compression. *Computaional Materials Science* 36:329-337

113 German R M, Park S J (2008) Handbook of Mathematical Relations in Particulate Materials Processing. Wiley

114 Jones W D (1960) Fundamental principles of powder metallurgy. Edward Arnold, London

115 V. Shatokha, I. Korobeynikov, E. Maire, L Gre´millard, J. Adrien (2010) Iron ore sinter porosity characterisation with application of 3D X-ray tomography. *Ironmaking and Steelmaking* 37(5): 313-319

116 W.H. Shih, F. C. Chou, W. H. Hsieh (2007) Experimental investigation of the heat transfer characteristics of aluminum-foam heat sinks with restricted flow outlet. *Journal of Heat Transfer* 129: 1554-1563

117 Shakelford, J. F. (2010) Introduction to materials science for engineers (7th edition) Pearson Prentice Hall